Establishing Quantitative Relationships Between Composition, Morphology, and Performance in Polymer Electronics

Wesley K. Tatum

A dissertation

submitted in partial fulfillment of the

requirements for the degree of

Doctor of Philosophy

University of Washington

2020

Reading Committee:

Christine Luscombe, Chair

Guozhong Cao

Dwayne Arola

David Beck

Program Authorized to Offer Degree: Materials Science and Engineering

University of Washington

ABSTRACT
Establishing Quantitative Relationships Between Composition, Morphology, and Performance in Polymer Electronics

Wesley K. Tatum

Chair of the Supervisory Committee:
Prof. Christine Luscombe
Materials Science and Engineering

π-Conjugated polymers (CPs) have been the subject of a rapidly growing body of research ever since their discovery in the 1970s. A great deal of work has been conducted to improve device performance and better understand the relationships between monomer design and optoelectronic properties. However, the same effort has not been put into understanding the driving factors for morphological development or the impact of morphology on the final device performance, partially due to the complex and highly dependent nature of the morphology in these materials. This work seeks to 1) understand the role of structural defects on the crystal lattice and morphology of CPs, 2) to develop quantitative methods for studying morphological development to predict device performance. First, self-assembled nanowires of poly(3-hexylthiophene), a well-studied CP, are used to probe the effect of regio-defects and chain end-groups on the crystal. The defects were found to readily incorporate into and disrupt the crystal lattice, and they were used to influence nanowire morphology. Next, an unsupervised machine learning toolkit is developed, which automatically processes and labels the phases and domains in scanning probe microscopy images. Finally, the labels generated by this toolkit are used to examine the benefits of quantitative morphological information using a variety of regression and neural network techniques. This data, and subsequently the models, describe changes in morphology and device performance for two types of CP-based devices during thermal annealing. Current efforts and future work are discussed.

TABLE OF CONTENTS

List of Figures viii

List of Tables xxiii

Chapter 1. Introduction 1

1.1 Deformable Electronics 1

1.2 π-Conjugated Polymers: Optoelectronic Properties 2

1.3 π-Conjugated Polymers: Mechanical Properties 12

1.4 Thin Film Morphology of π-Conjugated Polymers 14

Chapter 2. Defect Tolerance of π-conjugated polymer crystal lattices 18

2.1 Background: Crystallization in Traditional, Non-Conjugated Polymers 18

2.2 Chemical Defects in π-Conjugated Polymers 25

2.3 Materials and Methods 31

2.3.1 Materials 31

2.3.2 Nanowire Production and Isolation 31

2.3.3 Size Exclusion Chromatography 32

2.3.4 ^{1}H Nuclear Magnetic Resonance 32

2.3.5 Matrix Assisted Laser Desorption/Ionization – Time of Flight (MALDI-TOF) 33

2.3.6 X-Ray Diffraction (XRD) 33

2.3.7 Differential Scanning Calorimetry (DSC) 33

2.3.8 PeakForce Quantitative Nanomechanical Mapping Atomic Force Microscopy (QNM) 33

2.3.9 Amplitude-Modulation, Frequency-Modulation Force Microscopy (AMFM) 34
2.4 Results and Discussion 34
2.5 Conclusions 50
2.6 Supporting Information 51
Chapter 3. A Generalizable Framework for Algorithmic Interpretation of Thin Film Morphologies in Scanning Probe Images 68
3.1 Introduction 68
3.2 Materials and Methods 71
3.2.1 m2py Development 71
3.2.2 Substrate Preparation 71
3.2.3 Thin Film Sample Preparation 72
3.2.4 Nanowire Film Preparation 73
3.2.5 Force-Distance Mapping Atomic Force Microscopy (FDM) 73
3.2.6 AMFM 73
3.2.7 Conductive Atomic Force Microscopy (C-AFM) 73
3.3 Results and Discussion 74
3.3.1 Data Intake and Pre-Processing 75
3.3.2 Feature Selection and Semantic Segmentation 76
3.3.3 Instance Segmentation 83
3.3.4 Final Output and Transferability 87
3.4 Conclusions 91
3.5 Supporting Information 91
3.5.1 Data Intake and Pre-Processing (Continued) 91

3.5.2 Feature Selection (Continued) 93
3.5.3 Semantic Segmentation 94
3.5.4 Instance Segmentation (Continued) 96
Chapter 4. Using Quantitative morphology to Explain and Predict device performance 100
4.1 Introduction 100
4.2 Methods and Materials 101
4.2.1 Regression and Code Development 101
4.2.2 Substrate Preparation 101
4.2.3 Thin Film Deposition 102
4.2.4 OPV Devices and Testing 102
4.2.5 OFET Devices and Testing 103
4.2.6 Force-Distance Mapping (FDM) 104
4.3 Results and Discussion 104
4.3.1 Data and Sampling 104
4.3.2 Regression on Tabular Data Only 107
4.3.3 Regression on Multidimensional Morphological Data 112
4.4 Conclusions 116
4.5 Supporting Information 117
4.5.1 OPV Dataset Feature Surfaces 117
4.5.2 Regressor Performance 121
4.5.3 Hyperparameters 126
Chapter 5. Future Work and Considerations 130

5.1 Improvements to Models Predicting OFET and OPV Performance 130
5.1.1 Finishing the Comparison 130
5.1.2 Data and Sampling 130
5.1.3 Model Optimization 131
5.1.4 Image Encoding 131
5.2 Rectifying Kinetic Monte Carlo Simulations to Experimental Results 133
5.3 High Performance π-Conjugated Polymer Morphologies and Performance 134
Chapter 6. References 136

LIST OF FIGURES

Figure 1.1. Some sample strategies for creating compliant interconnects for stretchable inorganic devices.……..…….2

Figure 1.2. By depositing the OPV layers onto a pre-strained substrate, compliant devices can be created, which survive high bending radii..…….…….....4

Figure 1.3. A diagram representing the emergence of band-like behavior in CPs as more monomer units participate in the conjugation..…….…...5

Figure 1.4. An illustration of the positional dependence of H- and J-aggregation, per the Spano model. When θ < ~57º, J-aggregation is dominant.…….,……6

Figure 1.5. An illustration of the dependence of absorption and charge conduction on molecular weight. Lower M_n crystallites prefer intermolecular, H-aggregation, with high M_n crystallites preferring intramolecular J-aggregation..……..…….…..7

Figure 1.6. A top-down view of thin film morphology in traditional polymers, with lamellar crystalline domains and amorphous domains.……..……8

Figure 1.7. A schematic representation of the transition from chain-extended crystals to entangled crystalline lamellae, with increased M_n……...8

Figure 1.8. Regio-defects in P3HT, HH and TT coupling, compared to the preferred HT coupling……..……10

Figure 1.9. AFM images of two P3HT OFET active layers, where the left picture has been annealed at 100 ºC for 15 minutes and the right picture 150 ºC for 30 minutes……11

Figure 1.10. a. A plot of semicrystalline CP showing the correlation between modulus and charge transport. b. A plot from a study of D-A polymers for intrinsically stretchable CP…….13

Figure 1.11. Representations of the three known thin film morphology classes in CPs: a. semicrystalline, b. disordered aggregates, c. completely amorphous.……..……..15

Figure 1.12. A representation of charge mobility in relation to crystallinity and charge transport methods……..16

Figure 2.1. Schematic representations of (top) partial inclusion of defects and the resulting lattice distortions and (bottom) complete exclusion of defects…….20

Figure 2.2. (left) Simulation results of PE lamellar growth. (middle) Thermal fluctuations create crystallizable stems of a minimum length needed to stably grow the lamella. (left) As stems grow in the crystal, slack from other stems propagates to account for the growth……..……....22

Figure 2.3. By inserting aromatic defects into the middle of PEO chains, the angle at which the polymers crystallize can be tuned via the substitution of the aromatic group……24

Figure 2.4. Regio-defects in P3HT: (left-to-right) HH and TT coupling, compared to the preferred HT coupling……...25

Figure 2.5 A representative diagram of a CP crystallite. Bulky end-groups can be similar in size to the intermolecular distance, which is disruptive to crystal growth…….…….27

Figure 2.6. A top-down view of thin film morphology for traditional polymers following Flory's model of complete exclusion, with lamellar crystalline domains separated by amorphous domains and the defects only residing in the amorphous domains. As shown in this figure, the amorphous regions (A) contain all of the chemical defects, including short backfolds (SB), long backfolds (LB), chain ends (E), voids (V), migrating folds (MF), and Statton model (ST) defects, as well as the beginnings of new crystallites (CG). Depending on processing, crystalline domains can be single fibrils (SF), clustered fibrils (CF), paracrystalline layerlattice (P), or single crystals (SC). Shown also are shearing region defects (SH) to the crystal lattice…….30

Figure 2.7. Proposed nanowire structures for the cases where there is either (A) complete exclusion of defects or (B) partial inclusion of defects into the crystal lattice. Darker grey indicates higher crystallinity.……...…35

Figure 2.8. A representative PeakForce AFM image of P3HT nanowires that are aged (left-to-right) 24, 48, and 72 hours. Scale bars are all 500 nm. As seen in these height scans, and described in Table S1, there are no differences in the dimensions of the nanowires in these three different samples……...…37

Figure 2.9. A plot demonstrating that, despite differences in the crystallinity that result from varied defect concentrations, there is little difference in the nanowire widths and l_c for the different samples. Linear fits provide visual guides for the data. Error in the data is associated with instrumental precision. These results are more completely shown in Table S.2.1……..38

Figure 2.10. An overlay of the normalized UV-vis absorption spectra for the 24, 48, and 72-hour aged Rieke P3HT nanowires. The absorption peaks corresponding to the 0-0 and 0-1 transitions are marked reference. As seen in above plots, as age increases, so does the $A_{0\text{-}0}/A_{0\text{-}1}$ ratio, signifying more backbone planarity and increased short-range order…….……..…….39

Figure 2.11. A plot generated from data in Table S2.2. The hole mobility, nanowire width, and $\xi_{(010)}$ are plotted as a function of regioregularity. Linear fits provide visual guides for the data. Error in the data is associated with instrumental precision. Changes in regioregularity have drastic

effects on the short-range order of the nanowires, as measured by both XRD and OFET mobility……..41

Figure 2.12. Predicted structures of the nanowires that are described in Table S3, with (top, left to right) DP = 50, 100, 150 and (bottom, left to right) DP = 75, 125. l_c remains relatively consistent for all samples above DP = 50…….42

Figure 2.13. A plot showing the enthalpy of fusion and coherence *versus* DP for a series of P3HT nanowires, described in Table S2.3. Error in the data is associated with instrumental precision. This plot illustrates the effects of harmonic vs. non-harmonic DP on the crystallinity and short-range order of nanowires. Sinusoidal curves are fitted to emphasize the role of DP on the incorporation of end-groups……...43

Figure 2.14. (A-C) 2 × 2 μm topographical scans of nanowires formed from Tol-200-100-narrow, Br-275-98-narrow, and Br-150-91-wide (right-to-left). (D-F) Young's modulus scans of the same nanowires. All images are from AMFM scans, all scale-bars are 500 nm. Larger segments are seen in nanowires made from P3HT with lower defect concentrations and π-interacting end-groups. As indicated, defect concentration increases from right-to-left, and short-range order increases from left-to-right. The length of segments, or crystal grains, in the nanowires are denoted in E and F with green rectangles. Grain size increases as defect concentration is reduced…….46

Figure 2.15. An overlay of the UV-vis absorption profiles for the nanowires shown in Figure 11. The absorption peaks corresponding to the 0-0 and 0-1 electronic transitions are marked for

reference. An increase in the $A_{0\text{-}0}/A_{0\text{-}1}$ ratio signifies increased short-range order and electronic coherence along the backbone. As discussed, Br-150-91-wide had the most defects, least order and, correspondingly the lowest $A_{0\text{-}0}/A_{0\text{-}1}$ ratio. Conversely, Tol-200-100-narrow had the fewest overall defects and therefore has the highest $A_{0\text{-}0}/A_{0\text{-}1}$ ratio……49

Figure S2.1. ^{1}H NMR of 24 h nanowire incorporated polymer……...54

Figure S2.2. ^{1}H NMR of 24 h nanowire decanted polymer ……...…….54

Figure S2.3. ^{1}H NMR of 48 h nanowire incorporated polymer…….……55

Figure S2.4. ^{1}H NMR of 48 h nanowire decanted polymer……55

Figure S2.5. . ^{1}H NMR of 72 h nanowire incorporated polymer……56

Figure S2.6. ^{1}H NMR of 72 h nanowire decanted polymer…….……56

Figure S2.7. ^{1}H NMR of as-purchased commercial polymer……..57

Figure S2.8. MALDI- TOF of 24 h nanowire incorporated polymer……..57

Figure S2.9. MALDI- TOF of 24 h nanowire decanted polymer……58

Figure S2.10. MALDI- TOF of 48 h nanowire incorporated polymer……58

Figure S2.11. MALDI- TOF of 48 h nanowire decanted polymer……..59

Figure S2.12. MALDI- TOF of 72 h nanowire incorporated polymer……59

Figure S2.13. MALDI- TOF of 72 h nanowire decanted polymer……..60

Figure S2.14. MALDI- TOF of as-purchased commercial polymer……..60

Figure S2.15. DSC overlay of commercial polymer nanowire aging series polymer…….61

Figure S2.16. XRD spectra of the as purchased commercial P3HT……61

Figure S2.17. XRD spectra of 24 h aged commercial P3HT nanowires…….……62

Figure S2.18. XRD spectra of 48 h aged commercial P3HT nanowires……..62

Figure S2.19. XRD spectra of 72 h aged commercial P3HT nanowires……..63

Figure S2.20. DSC overlay of synthesized polymer nanowires……..63

Figure S2.21. XRD of DP = 50 P3HT nanowires……..64

Figure S2.22. XRD of DP = 75 P3HT nanowires……64

Figure S2.23. XRD of DP = 100 P3HT nanowires……..65

Figure S2.24. XRD of DP = 125 P3HT nanowires……65

Figure S2.25. XRD of DP = 150 P3HT nanowires…….66

Figure S2.26. AMFM line-scans of Tol-200-100-narrow nanowire properties, along the [010] direction……..……66

Figure S2.27. AMFM line-scans of Br-275-98-narrow nanowire properties, along the [010] direction…….67

Figure S2.28. AMFM line-scans of Br-150-91-wide nanowire properties, along the [010] direction…….67

Figure 3.1 A generalized m2py workflow. Raw or pre-cleaned data is fed in by the user. Next, outlier removal and fast Fourier transforms are applied to increase the sensitivity of m2py's segmentation modules. Feature selection finds the most descriptive features from the data while reducing data dimensionality to distill the material-property signals. This is followed by semantic

segmentation (pixel classification) and then instance segmentation (pixel clustering). Statistical information can be extracted at any point in the workflow…….74

Figure 3.2. Signal distributions and cross-correlations are easily extracted throughout the workflow. a. Four input material-property distributions from an annealed P3HT:$PC_{61}BM$ thin film. Input channel units are relative. b. Cross-correlations from the same sample after GMM segmentation, with red and blue representing the two GMM labeled phases. c. (*left*) An example principal component from PCA of the same sample. Principle component units are arbitrary. (*right*) The property distributions for each of the two GMM phase for the principal component. d. Cross-correlation between principal component 1 and 3, color-coded by their GMM phase labeling. Scale bar is 200 nm, images are 256 × 256 pixels……77

Figure 3.3. Input data and the GMM label maps from FDM measurements of a P3HT OFET active layer. a. The input data channels after outlier and noise removal. Colorbar units are relative. b. GMM labeling when the height channel is included. **c.** GMM labeling when the height channel is excluded. All scale bars are 500 nm, imaged at 512 × 512 pixels……...79

Figure 3.4. Input data and GMM label maps from FDM measurements of a PTB7:$PC_{71}BM$ thin film OPV active layer. a. The input data channels after outlier and noise removal. Colorbar units are relative. b. GMM labels when the height channel is included. c. GMM labels when the height channel is excluded. d. Graphical explanation of how large features can artificially alter measured material response signals by varying the amount of surface-area contact between the probe-tip and sample surface. The scale bars are 200 nm, images are 256 × 256 pixels……..….80

Figure 3.5. Results of GMM segmentation on two different samples. a. Two component classification of a P3HT:$PC_{61}BM$ thin film, where red and blue corresponds to the different components. The input channels are shown in the top two rows alongside their material-property signal distributions that are color coded by GMM component. Scale bars are 200 nm, images are 256 × 256 pixels. b. Results of two component classification of P3HT nanowires (blue) spin-coated onto a passivated SiO_2 substrate (red). The input channels are shown in the bottom two rows, alongside their corresponding material-property signal distributions color coded by GMM phase components. Scale bars are 500 nm, images are 512 × 512 pixels……..82

Figure 3.6. A representative channel from a FDM image of PTB7:$PC_{71}BM$ is shown, followed by the results throughout m2py analysis of the image. First undergoing semantic segmentation, the resulting GMM phase labels show the spherical aggregates to be a distinct phase from the matrix. Phase 1 is shown in yellow, phases 2 and 3 are combined in purple. Next, the height channel is used in instance segmentation by the PWS method, producing individually indexed morphological domains. The color of each individual domain is selected according to its size. Finally, PWS labels that correspond to GMM phase 1 are plotted in green and the mislabeled phase 1 pixels plotted in yellow for contrast. Scale bars are 1 μm, images are 512 × 512 pixels……85

Figure 3.7. Throughout the m2py workflow, labels can be used to calculate and analyze relative ratios, property distributions, and domain descriptors. Simple examples are presented for a P3HT:$PC_{61}BM$ thin film. a. The height channel from FDM analysis of a P3HT:$PC_{61}BM$ thin films is shown. Colorbar units are relative. b. Domain labels are determined by connected components labeling and then sorted by their GMM label. The color of each individual domain is selected

according to its size. (*left*) Phase 1 domains, with black domains being phase 2. The co-continuous matrix domain is remapped to the lightest color for visibility. (*right*) Phase 2 domains, with black domains being phase 1. c. The major-axis length, in pixels, of connected components labeled domains, sorted by GMM label. d. The major-axis length, in pixels, of connected components labeled domains. e. The log of connected components labeled domain areas in pixels. The scale bars are 1 μm and the images are 500 × 500 nm and are 256 × 256 pixels……88

Figure 3.8. Input data channels and m2py labeling results for P3HT nanowires spin-coated onto passivated ITO glass. a. Property channels of AMFM measurements of P3HT nanowires on ITO glass. Colorbar units are relative. b. GMM labels with coloring corresponding to GMM phase labels. c. Connected components labels. The color of each individual domain is selected according to its. d. Property channels for C-AFM measurements of P3HT nanowires on ITO glass. Colorbar units are relative. e. GMM labels with coloring corresponding to GMM phase labels. f. Connected components labels. Scale bars are 200 nm, images are 256 × 256 pixels……90

Figure S3.1. In order to detect outlier pixels in an image, the z-score of all pixels is computed. Z-score values surpassing an adjustable threshold are identified as outliers. Outliers are re-assigned the median value of the channel to improve visualization of the sample. P3HT:$PC_{61}BM$ FDM, 500 × 500 nm and imaged with 256 × 256 pixels……..92

Figure S3.2. In order to enhance the clarity of images and remove background noise, each channel undergoes a fast Fourier transform. While in Fourier-space, an adjustable band-pass filter is applied to remove noisy frequencies. Shown above is an example channel from a P3HT:$PC_{61}BM$

FDM image before and after the 5% lowest-magnitude frequencies are removed (*i.e.* 95% of the signals remain). The scale bar is 200 nm, image is 256 × 256 pixels……..93

Figure S3.3. Results of m2py semantic (GMM) and instance segmentation (persistence watershed and connected components) for four different samples, one per row. The height channel of each sample is shown in the far-left column, GMM results are shown in the second column. PWS labels, sorted by their size are shown in the third column, and connected components labeling in the fourth. Scale bars are (top to bottom) 200 nm, 200 nm, 500 nm, and 200 nm, and images are 512 × 512, 512 × 512, 512 × 512, and 256 × 256 pixels, respectively. False color bars on the clustering images correspond to the domain indexing labels, which are integers……97

Figure 4.1. MSE for each model predicting 4 OPV device metrics (*PCE*, V_{oc}, J_{sc}, and *FF)*. Each model was trained on either the AOD or on the CTD……109

Figure 4.2. NN prediction of J_{sc} had the worst R^2 value when it only saw time and temperature data, but improved to the best R^2 after including tabular data summarizing the morphology of the device active layers……..……109

Figure 4.3. MAPE for each model predicting the 4 OPV device metrics, *PCE*, V_{oc}, J_{sc}, and *FF*. Each model was trained on either the AOD or on the CTD.……..…111

Figure 4.4. R^2 for each model predicting the 4 OPV device metrics, *PCE*, V_{oc}, J_{sc}, and *FF*. Each model was trained on either the AOD or on the CTD…...……111

Figure 4.5. a. Network architecture for NN1 and NN2. Only tabular data is taken in and used to make device predictions. b. Network architecture for NN3 and NN4. Only image-like data is taken in, encoded, and used to make predictions. These models take in either m2py labels or SPM data and compress the 2-dimensional channels into 1-dimensional tensors before branching. c. Network architecture for NN5, NN6, and NN7 is shown. These models take in both tabular and image-like data. The encoded representations of these data are aggregated before the network branches to make its device predictions……..113

Figure S4.1. Device performance metrics for samples in the OPV dataset that includes morphological information (CTD). 3D surface represents the average value for a given (Time, Temperature) point on the graph. Individual devices are shown as black dots to show variation between samples……...117

Figure S4.2. Device performance metrics for samples in the OPV dataset that only includes annealing conditions (AOD). 3D surface represents the average value for a given (Time, Temperature) point on the graph. Individual devices are shown as black circles to show variation between samples……..118

Figure S4.3. Representative morphology descriptors in the OPV dataset that includes morphological information. The active layers were all labeled with 3 phases (fullerene-rich, polymer-rich, and mixed phase, respectively). The 3D surface represents the average area value

(in pixels) for a given (Time, Temperature) point on the graph. Individual devices are shown as black circles to show variation between samples……..119

Figure S4.4. Representative morphology descriptors in the OPV dataset that includes morphological information. The active layers were all labeled with 3 phases (fullerene-rich, polymer-rich, and mixed phase, respectively). 3D surface represents the average eccentricity value (unitless) for a given (Time, Temperature) point on the graph. Individual devices are shown as black circles to show variation between samples……..120

Figure S4.5. Representative morphology descriptors in the OPV dataset that includes morphological information. The active layers were all labeled with 3 phases (fullerene-rich, polymer-rich, and mixed phase, respectively). 3D surface represents the average perimeter length value (in pixels) for a given (Time, Temperature) point on the graph. Individual devices are shown as black circles to show variation between samples……..121

Figure S4.6. R^2 results for LASSO predictions after training on CTD (top 4) and AOD (bottom 4)……..122

Figure S4.7. R^2 results for RF predictions after training on CTD (top 4) and AOD (bottom 4)…123

Figure S4.8. R^2 results for SVM predictions after training on CTD (top 4) and AOD (bottom 4)……..124

Figure S4.9. R^2 results for NN predictions after training on CTD (top 4, NN2) and AOD (bottom 4, NN1)……..125

Figure S4.10. Representative results of learning rate optimization of NN3. For each learning rate, the MSE, MAPE, and R^2 are plotted for 30 epochs of training. For each graph, the blue dot corresponds to the epoch with the best value for that metric (*e.g.* lowest loss)…….129

LIST OF TABLES

Table S2.1. The results of analyzing nanowires made from commercial P3HT, aged for different times. Numbers in parenthesis indicate results from analyzing the unincorporated P3HT for that sample. Corresponding data is shown in Figures S2.1-S2.19…….51

Table S2.2. The results of analyzing nanowires made from P3HT of varying RR…...……..52

Table S2.3. The results of analyzing nanowires made from P3HT of varying M_n. P3HT with integer multiples of l_c are above the bold line. P3HT with non-integer multiples are below the bold line. Results of XRD and DSC analysis are shown in Figures S20-S25.…….……53

Table 4.1. Thermal annealing conditions that devices in the P3HT:$PC_{61}BM$ OPV dataset were subjected to during device fabrication. Color indicates the relative amount of thermal energy that the active layer was exposed to, ranging from dark blue (low) to dark red (high).…….……105

Table 4.2. Thermal annealing conditions that devices in the P3HT OFET dataset were subjected to during device fabrication. Color indicates the relative amount of thermal energy that the active layer was exposed to, ranging from dark blue (low) to dark red (high).…….……105

Table 4.3. Model name, training set, and progress for the NN predictors outlined in this work…115

Table S4.1 A table summarizing the optimized hyperparameter values for the presented regressors…….126

ACKNOWLEDGEMENTS

There are so many people that need to be acknowledged and thanked, but I simply can't fit them all on this page. Here are a few (the rest of you know who you are):

All of this work is the product of collaborations, teams, and friends. First, I want to thank the Luscombe research group and my PI, Prof. Christine Luscombe. This group and the opportunities you've given me have been an integral part of my growth and learning throughout this graduate school experience. I want to thank the Luscombe group (present and past) for your support, criticism, feedback, and group hang-outs and lunches. I also want to specifically thank Dr. Lauren Kang, Dr. Wesley Beckner, and (soon-to-be Dr.) Jon Onorato for their help, support, and friendship in both lab and life.

Thank you also to the Clean Energy Institute for funding some of this research, for the opportunity to learn data science, and supporting so many of my efforts and projects with student groups and events. On that subject, I want to thank Prof. Lilo Pozzo for inviting me into her work with off-grid solar and research in partnership with communities, which deserves to be in this dissertation; thank you for your support and inspiration.

I also want to thank my parents and brothers who have supported me since the beginning. You helped foster my curiosity and love of nature and are why I got to take this opportunity to learn about the world.

Finally, I want to thank my wife and best friend, Bethany. I simply would not be here without you and your support throughout our almost 9 years together. This one's for you.

DEDICATION

This dissertation is dedicated to my wife, my family, and all the friends who have helped me along the way.

Chapter 1. INTRODUCTION

1.1 DEFORMABLE ELECTRONICS

Developing electronic and optoelectronic devices with the ability to experience structural deformation without also experiencing electronic failure is of keen interest to many fields, such as energy production, personal electronics, and healthcare. These types of devices could help enable the development of new applications and devices that can, for example, be applied to curved or flexible surfaces, adhered to skin, or implanted inside the body.[1–4] Thin and elastomeric semiconductors with relatively compliant properties used in electronic devices would allow these devices to continue performing while stretching over pointed joints, or enduring twisting, pulling, and shear pressure.

Currently, the vast majority of electronic devices are made with inorganic conductors and semiconductors. In order to compensate for the brittle nature of highly crystalline inorganic semiconductors, such as Si, engineering techniques have been developed with the goal of introducing slack to the connections between small devices; these folds can then be straightened out during elongation, preserving the high crystallinity of the bulk device which is ideal for electronic performance. This is typically done through non-linear or non-coplanar bridges and precise nanostructure control, as shown in Figure 1.1.[5–12] While these techniques are able to achieve a degree of extensibility and deformability, they require film growing techniques that are highly sensitive, slow, and expensive. Use of such demanding and time-consuming batch-production techniques limits the scalability such processes. Many of these techniques require a stretchable, elastomeric substrate that is pre-strained during electrode deposition, adding further production complication.

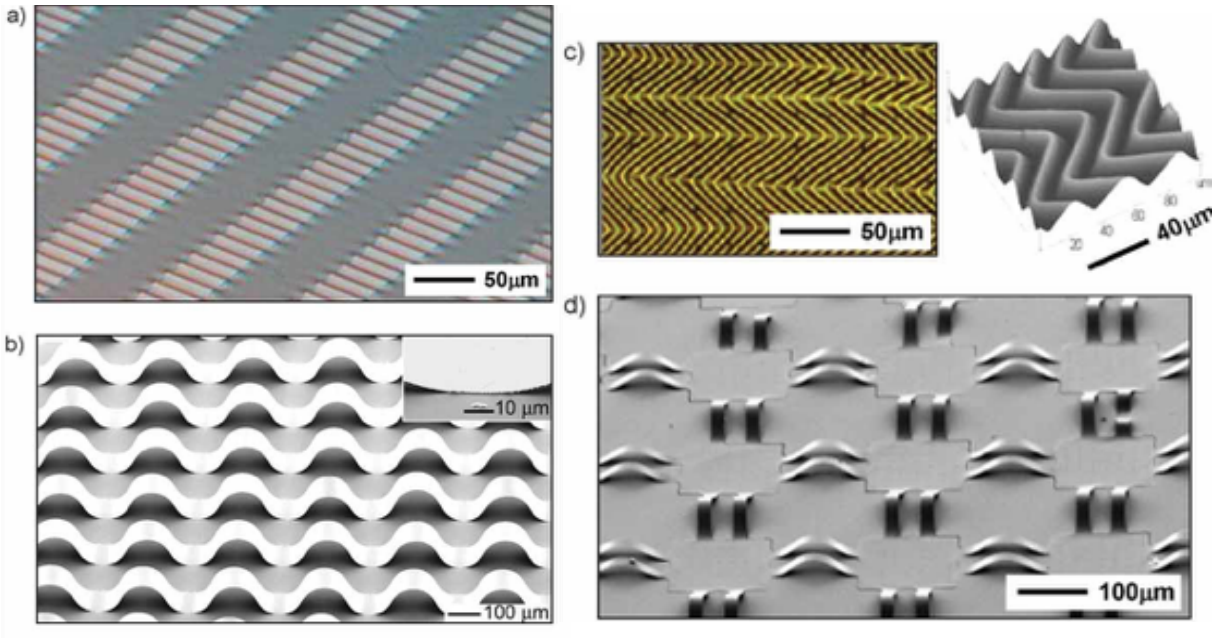

Figure 1.1. Some sample strategies for creating compliant interconnects for stretchable inorganic devices.[5]

So, despite their promising performance, such technically demanding designs are inherently limited in their ability to be mass produced. In order to avoid such time and energy consuming methods, the use of semiconducting materials that possess inherent mechanical compliance while retaining crystallinity would drastically simplify the production of deformable, robust, electronic and optoelectronic devices.

1.2 Π-Conjugated Polymers: Optoelectronic Properties

Among many candidates for next generation semiconducting materials, some of the most promising are π-conjugated polymers, which have been the subject of extensive research since their discovery in the 1970's, by Hideki Shirakawa, Alan G. MacDiarmid, and Alan J. Heeger, for which they were awarded the 2000 Nobel Prize in Chemistry.[13] Since their discovery, there has been tremendous progress into understanding and properly utilizing these π-conjugated polymers

(CPs). As a result of establishing design rules and heuristics, single junction all polymer photovoltaic devices have achieved power conversion efficiencies surpassing 17%,[14] organic field-effect transistors (OFET) have demonstrated intrinsic mobilities above 20 $cm^2/V•s$,[15] and ammonia sensors capable of sensing 8 ppb concentrations with millisecond accuracy,[16] highly efficient photodiodes[17] and low temperature thermoelectrics[18,19] have been demonstrated. CPs can be designed to be soluble in solvents and cast into thin films at conditions close to ambient temperatures and atmospheres, which allows them to be used in fabrication of large area devices with low energy usage and high throughput speeds techniques like slot-die coating,[20] or roll-to-roll coating (R2R).[21] These scalable, continuous production techniques significantly reduce the capital expenditure (CAPEX) required to build new factories and produce industrial-scale quantities of semiconducting devices.[22] What's more, the inherently amorphous aggregation behavior of polymers, which is present in many CPs, allows for intrinsically compliant active layers in semiconducting and conducting devices. This is due to a few distinct characteristics of these CP active layers. First, these layers are typically ultrathin, with OFETs achieving peak performance at ~50-100 nm thickness.[23] Because of their ubiquitously high absorption coefficient, α, highly light-absorbing layers can be produced with active layers of approximately 250 nm.[24] As a result of being so thin, these CP films are inherently flexible with some films surviving a bend radius on the order of 10 μm (shown in figure 1.2).[25] What's more, CPs can be designed and engineered to also be highly stretchable, and to maintain charge conduction throughout elongations beyond 50% for hundreds of cylces.[3,4,26,27] The emerging design rules for these stretchable systems will be explored later in this discussion.

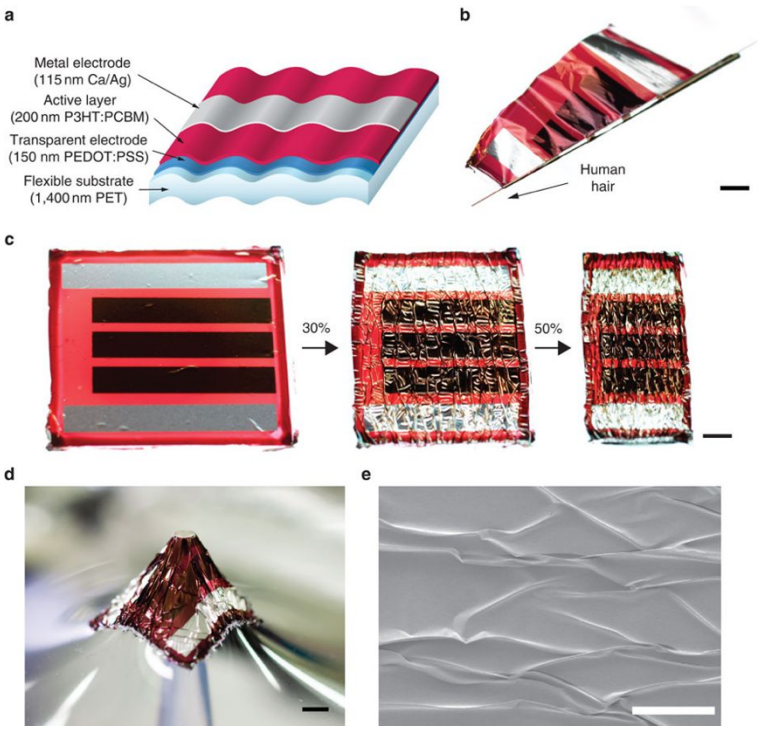

Figure 1.2. By depositing the OPV layers onto a pre-strained substrate, compliant devices can be created, which survive high bending radii.[25]

Conductivity and semiconductivity arise in polymers when there are extended networks of alternating double and single bonds, which is known as a π-conjugated structure and contains sp^2 hybridized atoms along the backbone of the polymers. As a result of the conjugation, electrons that are participating in the π-bonds can be delocalized along the extent of contiguously conjugated monomers. This delocalization is best along the backbone of the polymers, which is supported by the σ-bond, so uninterrupted backbone charge transport (*intra*molecular interactions) has the highest charge mobility. However, when units are in close proximity, such as in a crystallite, the π orbitals from two parallel chain segments can overlap and extend the conjugation between the two co-facial chains (*inter*molecular interactions) and achieve high mobilities as well. The number of monomer units that participate in the conjugation increases the density of states in the macromolecule which blend like a valence and conduction band; further conjugation reduces the

band gap between the highest occupied molecular orbital (HOMO) and the lowest unoccupied molecular orbital (LUMO), as illustrated by figure 1.3.[28–31] The more CP backbones planarize and cofacially close-pack, the more atoms are able to participate in the π-conjugation, and the longer the conjugation length is. The relative amounts crystalline and amorphous domains (rigid, aligned

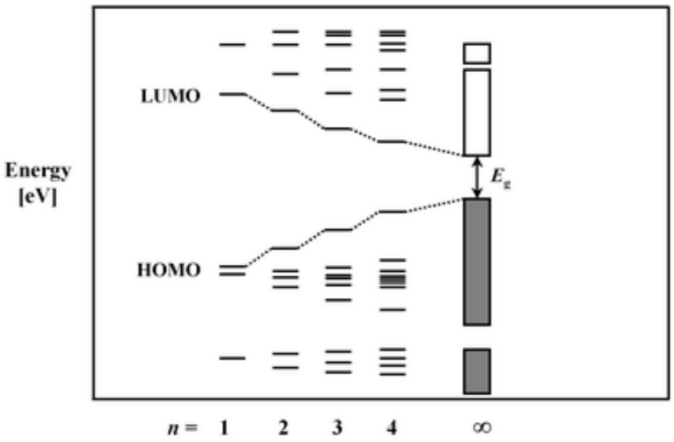

Figure 1.3. A diagram representing the emergence of band-like behavior in CP as more monomer units participate in the conjugation.[31]

chains and chaotic, unaligned chains, respectively) significantly determines the optoelectronic properties of the whole CP sample. The contributions of inter- and intramolecular charge coupling in crystalline and amorphous polymer is neatly described in Spano's HJ-aggregate model and illustrated in figure 1.4.[32–34] In this model, intrachain charge coupling produce Wanier-Mott type excitons and is characteristic of J-aggregation, while interchain coupling produces a Frenkel type exciton and is characteristic of H-aggregation. Due to the in-phase transition dipole moments present between the covalently bound, intrachain coupled monomers, the lowest energy 0-0 electronic transition is possible. Conversely, the out-of-phase transition dipole moments of the co-facial H-aggregates requires a vibronic in order to rectify electron-pair spins within the π* orbital during the transfer of the promoted electron from one monomer to the other in a 0-1 transition.

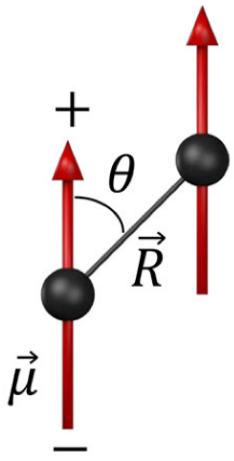

$$J_C^{pd} = \frac{\mu^2(1-3\cos^2\theta)}{4\pi\varepsilon R^3}$$

Figure 1.4. An illustration of the positional dependence of H- and J-aggregation, per the Spano model. When θ < ~57º, J-aggregation is dominant.[34]

The extent to which a system prefers H or J aggregation affects its optoelectronic properties, as a more J-aggregated system will tend to utilize the higher charge mobility intramolecular charge transport and will be able absorb light through the lower wavelength, 0-0 transition, an effect that is clearly visible in the UV-vis absorption profile within even a single polymer. For example, poly(3-hexylthiophene) (P3HT) can display both highly H-like and J-like UV-vis absorption spectra, as shown in figure 1.5.[35] Although figure 1.5 illustrates aggregation behavior that is solely dependent on the molecular weight, there are many different factors that influence electronic properties and can be used to tune them. Among the many variables in determining a CP's properties, some of the most studied are molecular weight (M_n), regioregularity (*RR)*, annealing, and aggregation. Each of these have been shown to affect the ability of the CP chains to pack, and interact with neighboring chains, each in their own ways.

As a CP progresses from a monomer, to an oligomer, to a polymer, the behavior of the whole sample changes drastically. For example, at low M_n, in many semicrystalline polymers, such as

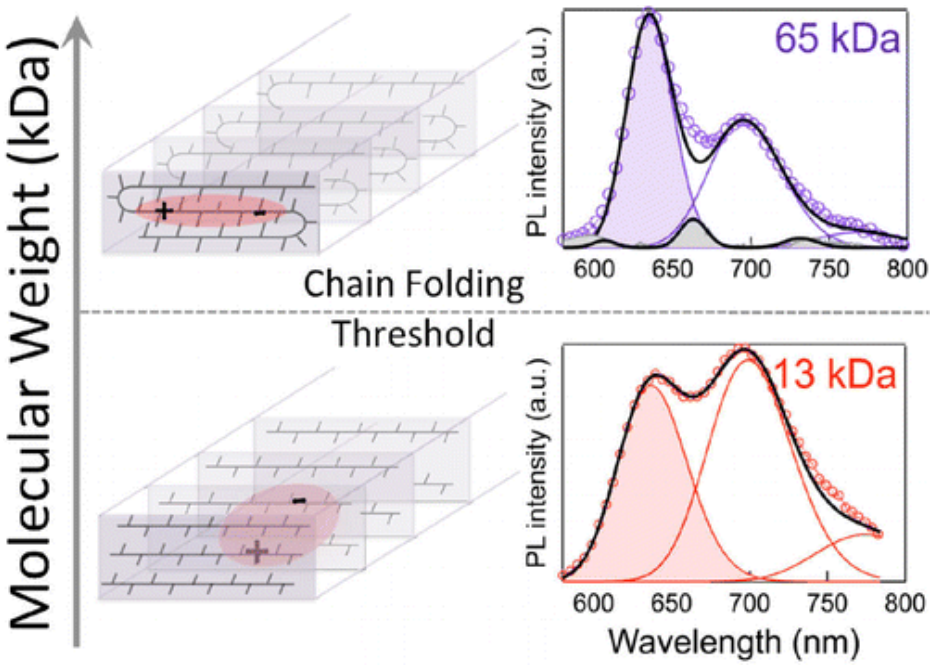

Figure 1.5. An illustration of the dependence of absorption and charge conduction on molecular weight. Lower M_n crystallites prefer intermolecular, H-aggregation, with high M_n crystallites preferring intramolecular J-aggregation.[35]

P3HT, the polymer chain becomes linear to participate in crystallites. The resulting improvements in close-packing planarizes the backbone. In a thin film, as used in semiconducting devices, lamellar domains of crystalline polymer are separated by amorphous polymer. This morphology with higher M_n polymer is pictured in Figure 1.6[36] and will be returned to in detail, later in this discussion. Crystallites of low M_n polymers are relatively isolated in a thin film. So, despite their heightened charge transport properties, excitons and polarons that are generated in one of these regions will have to pass through amorphous domains to reach their electrode, which drastically reduces the speed and likelihood of collection of charge carriers. As the M_n of the polymer chains increases past the characteristic persistence length of the CP, chain-folded crystals can form, as shown in Figure 1.7.[37] In P3HT, the transition from chain-extended, Form II crystals to chain-folded, Form I crystals occurs around 8.9 kg/mol, or ~50 monomer units.[38] In Form II P3HT, there

is a larger π-π stacking distance of the crystal lattice to accommodate the interdigitation of the solubilizing alkyl side-chains.[39]This can help explains why P3HT devices made from polymer with M_n above the ~8.9 kg/mol tend to have much higher charge

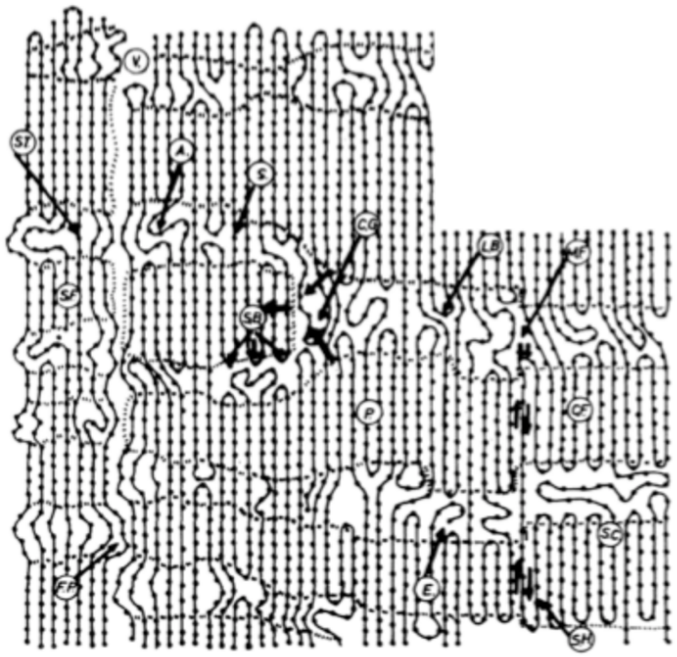

Figure 1.6. A top-down view of thin film morphology in traditional polymers, with lamellar crystalline domains and amorphous domains.[36]

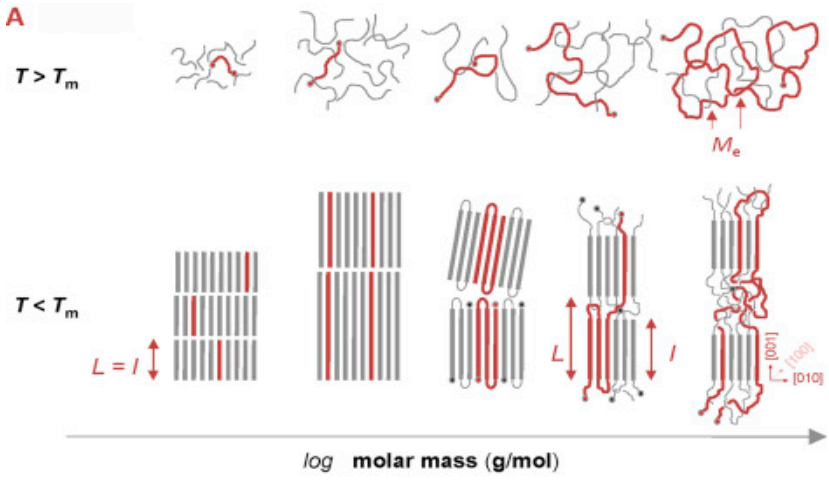

Figure 1.7. A schematic representation of the transition from chain-extended crystals to entangled crystalline lamellae, with increased M_n.[37]

mobilities. Another contributing factor is tie-chains, which will be returned to below. Beyond the characteristic persistence length, there is an additional, critical molecular weight, which serves as the critical M_n needed to support entanglement. This corresponds to ~25-35 kg/mol in P3HT.[37] Entanglement occurs when polymer chains are long enough to be incorporated into more than one crystalline domain, as shown in the high M_n regime of figure 1.5. These bridging chains are known as tie-chains and serve as critical highways for charge transfer between crystallites because they present a direct line of intramolecular charge transfer. So, above the critical M_n needed for entanglement, charge transport is more efficient between crystalline domains and there is another drastic increase in the charge mobility of the thin film, an effect that saturates as M_n increases.

The effect of *RR* on optoelectronic properties has been the subject of extensive research, however, it is contingent on the presence of asymmetric monomer units because symmetrical monomers cannot be incorporated backwards. As depicted in figure 1.8, P3HT monomer units can be incorporated into the main-chain backwards, creating either a head-to-head (HH) or tail-to-tail (TT) coupling instead of the preferred head-to-tail coupling (HT). When these regio-defects occur, the steric bulk of the alkyl side-chains interact with and displace each other, creating a torsion in the CP backbone that causes a more *gauche* alignment. As a result of the torsion, there is a decreased overlap of the π orbitals between the two contorted monomers. This decreased overlap reduces the continuity of conjugation along the backbone and thereby serves as a barrier to charge transport. The correlation between *RR* and charge mobility has been repeatedly demonstrated in P3HT, although the improvements saturate around 98% *RR*. It has also been noted that the *RR* of a CP influences the crystallinity and crystalline coherence in CP films and nanostructures, this is also attributed to the torsion that results from the regio-defect.[40–42] Twists in the backbone of CP reduce the planarity of the regio-defect monomers and their nearest neighbors. When the planarity

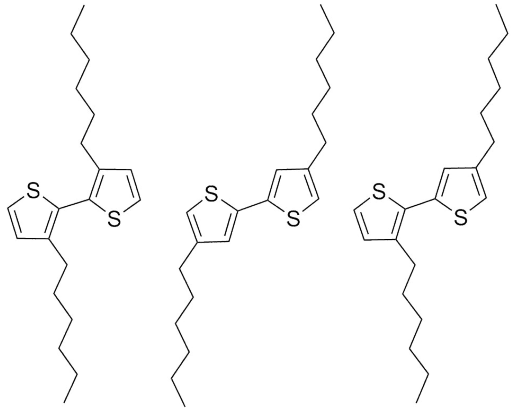

Figure 1.8. Regio-defects in P3HT, HH and TT coupling, compared to the preferred HT coupling.

of the backbone is reduced, the polymer chain loses its ability to close-pack with other chains.[43,44] So, not only do regio-defects disrupt intrachain charge transport by twisting the backbone, but they also decrease the interchain charge transport by perturbing close-packing of CP. In addition to RR, the development of donor-acceptor (D-A) copolymers brings the problem of homocoupling the donor or acceptor monomers, which is beyond the scope of this discussion.

When a thin film of CP is initially cast through a method like spin-coating or drop-casting, the dissolution of the chains in the solvent produces a stochastic distribution of the polymer chains, resulting in a highly amorphous film. Post-processing techniques like annealing can mobilize the solid-state polymer chains and allow them to aggregate and form crystalline domains. This mobilization of solid chains can be achieved through two means: through heating to film above the glass transition temperature (T_g) but below the melting temperature (T_m), in order to preserve film and electrode integrity, or through partial solvation with a solvent vapor, or even a combination of the two. Thermal annealing has been used to increase the charge mobility of P3HT, as measured by OFET, by up to an order of magnitude. P3HT devices are typically annealed at ~150 ºC for 15-30 min, which is a high enough temperature to soften the films and allow chains

to move but still low enough that the polymer will not flow or aggregate to the point of creating large fluctuations in film thickness.[45] As illustrated in figure 1.9, small differences temperature and duration of annealing can have large effects on the number of crystallizing nuclei and the extent to which they grow. The size and distribution of crystalline domains and aggregates in a film of CP significantly contribute to film's long-range order and charge transport properties. Similar to the crystalline nucleation through thermal annealing, solvent annealing (both with and without thermal annealing) is used to maintain chain mobility, either during or after film deposition. Conventional deposition techniques, such as spin-coating, deposit thin films from rapidly evaporating solvents. Because of the speed at which the film is produced, the CP chains are kinetically limited in their ability to crystallize and form highly amorphous films, as mentioned above. Solvent vapor annealing can be used *in situ* to increase the time that polymers have to aggregate for a number of different coating techniques.[46] This is particularly beneficial in coating methods that have a directionality, such as blade coating or dip coating.[47] These lateral casting

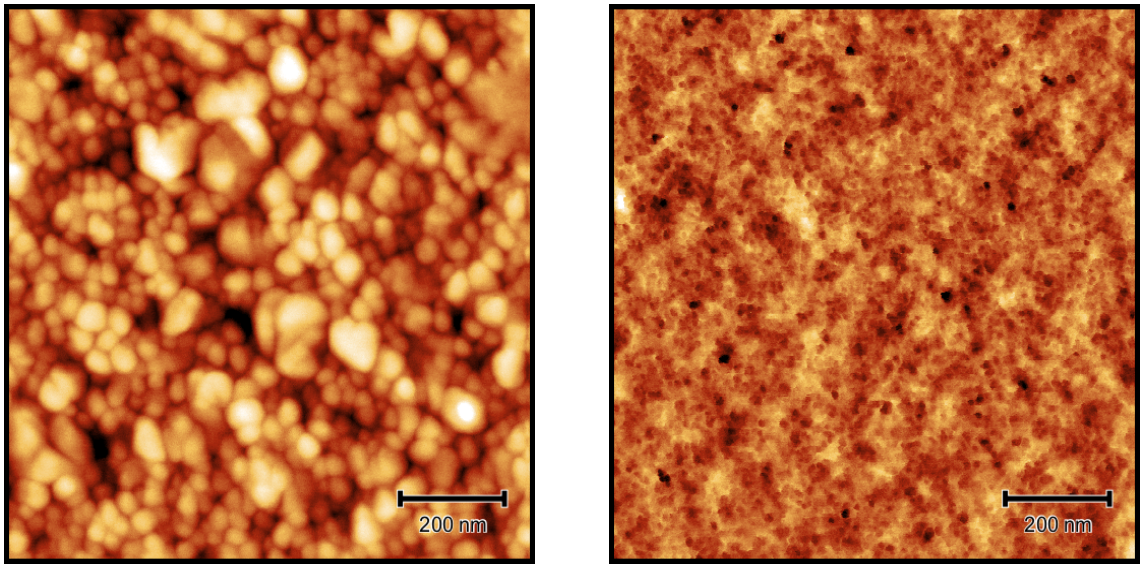

Figure 1.9. AFM images of two P3HT OFET active layers, where the left picture has been annealed at 100 ºC for 15 minutes and the right picture 150 ºC for 30 minutes.

techniques result in a sheer force, on the CP solution as it is drying, either through an evaporation meniscus or the geometry of a printing head, which can orient the polymer chains parallel to the casting direction.[48] By enclosing the casting structure, the solvent vapors are contained and exposed to the thin film, a simple method that can be highly scalable for large scale production.[49]

Finally, aggregation of the CP solution prior to casting can drastically improve the crystallinity and charge mobility of a give thin film.[50–52] This is a result of the self-assembly of highly crystalline nanostructures in the solution, which will be discussed in detail in a later section.

1.3 π-Conjugated Polymers: Mechanical Properties

While the solution-processability and electronic properties of CPs are promising, they are still yet to show the fully tunable mechanical properties that have become expected from commodity non-conjugated polymers, such as polyethylene (PE). Initially, it was assumed that the highly flexible, light-weight nature of CP thin films was sufficient to foster their commercial acceptance. However, other solution-processable, thin film materials, such as CdTe or perovskites have demonstrated higher charge mobilities and power conversion efficiencies, while being able to survive similar bending radii.[53,54] Recently, there has been a push to obtain highly stretchable and deformable CPs that can maintain a high degree of electronic performance throughout repeated deformation. Despite the wide and tunable range of mechanical properties in traditional, non-conjugated polymers, there has yet to be discovered a similar range of mechanical properties in highly conductive CP.[1,43,44,55,56] So far, this is attributed to distinct correlations between mechanical and electronic properties and their structural origins.

As explained in section 1.2, there is a distinct correlation between how close-packed and planar a polymer is and how well it transports charge. This has led the field to produce CP with higher

and higher degrees of crystallinity, resulting in many different thin film polymers as OFET that have demonstrated >3 $cm^2/V•s$ as a thin film. [46] However, as is evident in figure 1.10a, this progress has come at the cost of increased moduli.[55] Most CPs have a modulus of 1-10 GPa, which is 3-4 orders of magnitude above the value of skin: 0.05-20 MPa. Compounding this issue, CPs tend to have very low crack onset strains, as illustrated by figure 1.10b, with *CoS* of only 3-10%, far short of the 20-80% displayed by skin. Figure 1.10b does show that there have been some highly extensible polymers formed, but this ductility has come at the price of crystal disruption and low charge mobility.[1]

There has been some recent work relating the chemical structure and backbone torsion of D-A CPs to optoelectronic and mechanical properties. In these studies, it was found that the donor indacenodithiophene (IDT) can be paired with different acceptor moieties to achieve highly planar or highly contorted backbones in CPs that form disordered aggregates (a concept that will be addressed in section 1.4). These polymers lack the traditional semicrystalline morphology of CPs

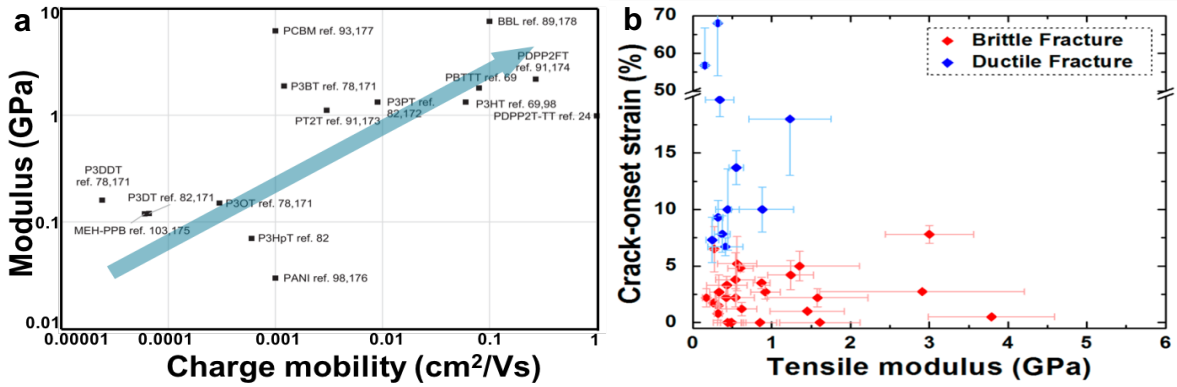

Figure 1.10. a. A plot of semicrystalline CP showing the correlation between modulus and charge transport.[54] **b.** A plot from a study of D-A polymers for intrinsically stretchable CP.[1]

such as P3HT, and can achieve +100% *CoS*, with a modulus of 80-400 MPa, close to being fully within the desired range of mechanical properties to be compatible with skin.[43,44] What's more, by

retaining short-range order in the thin films, even highly twisted backbones can have a hole mobility of 0.06 ± 0.03 $cm^2/V•s$, which surpasses other intrinsically stretchable CP. These results are impressive and lay the foundation for further work to disrupt the correlation between modulus and charge mobility.

1.4 Thin Film Morphology of π-Conjugated Polymers

The morphology of these CP thin films is of the upmost importance in any device application of semiconducting polymers for a number of reasons and it is evident that the thin film morphology of CP strongly influences many different properties, both mechanical and electrical. Thus, it is critical to understand the microstructural development of the thin films in order to develop repeatable and predictable processing conditions for fabricating CP devices. Thin films of semicrystalline CPs exhibit lamellar domains of crystalline CP, which are surrounded by amorphous domains, as illustrated in figure 1.11a. These domains are typically on the order of 10 nm in width and height but can reach as much as microns in length and resemble fringed micelles.[57] The crystalline regions are defined by a high degree of structural order and alignment of polymer backbones with each other.[58] This crystalline structure allows charges to travel much more efficiently through the material. The crystalline domains are large enough to interact with and scatter x-rays, allowing for rough size estimations to be conducted through Scherrer analysis (figure 1.11a). By contrast, the amorphous domains are defined by a distinct lack of structural order. In these domains, polymer chains are bent and overlap with each other. As such, there are traps states and other impedances in the amorphous domain that can limit charge mobility in the material and act as centers for charge recombination.[59] When a charge encounters a trap site, it

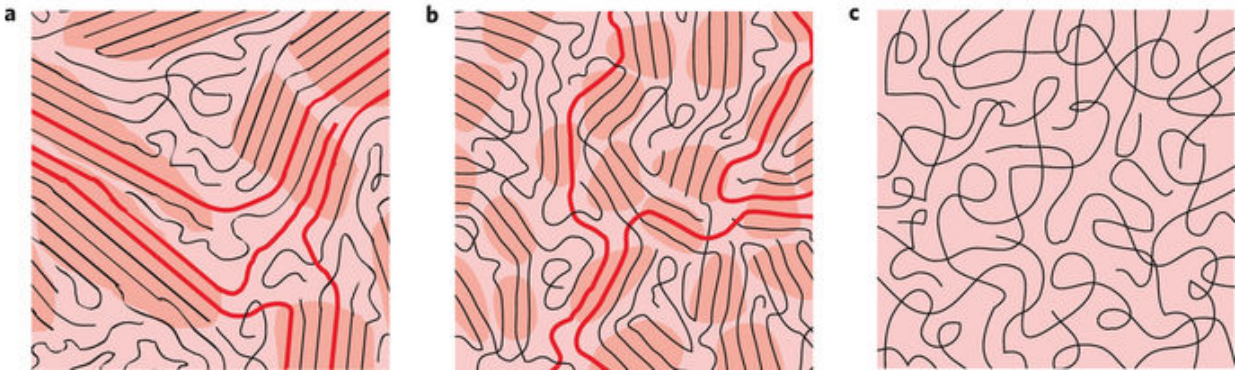

Figure 1.11. Representations of the three known thin film morphology classes in CP: a. semicrystalline, b. disordered aggregates, c. completely amorphous.[57]

can then relax or recombine with an opposite charge carrier, releasing the energy as either a photon or a phonon, rather than being utilized by the device.[60] This principle is one of the primary factors that limits the efficiency of OPV devices. Because of the trap state density in amorphous regimes, and a lower charge mobility, it has been definitively shown that crystalline domains are essentially solely responsible for charge conduction through the thin film and that relatively small amounts of such domains are needed for charges to be able to percolate through the film to the electrode. This is known as a percolation threshold. In blends of pre-aggregated, highly *RR* P3HT and regio-random P3HT, as little as 10% volume fraction of the *RR* P3HT was needed to reduce electroluminescence (EL) in the regio-random P3HT to negligible amounts.[57] So, in semicrystalline CP thin films with long-range order and relatively large crystalline domains, only a small concentration (~10%) of highly crystalline domains is needed to produce a high-performance thin film. The same study also outlined the morphology of disordered aggregates, as mentioned in the above section and illustrated by figure 1.11b. In such a thin film, the π-π interacting aggregates are ordered over a much smaller length scale than in the semicrystalline case. In fact, they are often too small to scatter x-rays, or do so weakly, particularly in the π-π stacking direction. However, despite the size of such aggregates, they serve as intermolecular

charge transfer points, which allow the charge carrier to percolate from chain to chain to the electrode. So, although there is less long-range order, disordered aggregates dispersed throughout the film and can utilize tie chains and high backbone charge mobilities to produce thin films with >1 $cm^2/V•s$ charge transport.[61] Finally, CP thin films can be completely amorphous (figure 1.11c) and rely solely on energetically expensive chain hopping mechanisms to percolate from chain to chain. Chain hopping, which is different from interchain transport, is the slowest charge transport mechanism, and is orders of magnitude below inter- and intramolecular charge mobilities, as shown in figure 1.12.[62]

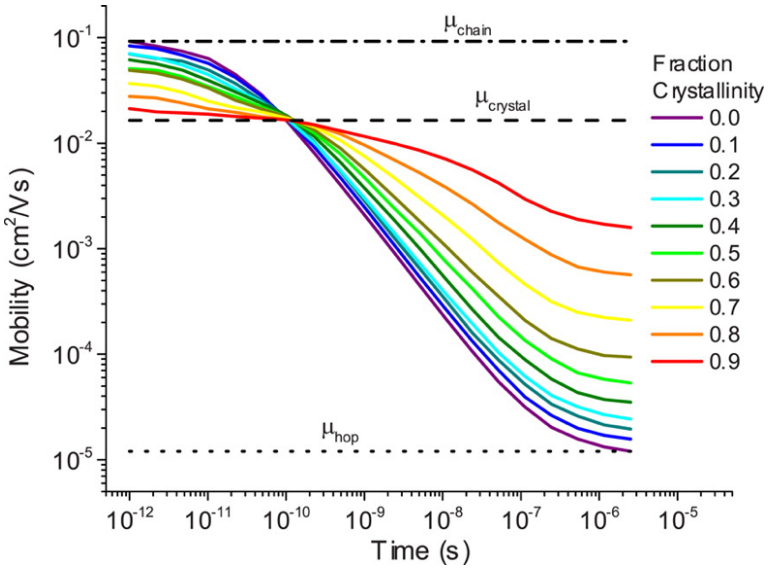

Figure 1.12. A representation of charge mobility in relation to crystallinity and charge transport methods.[62]

Different forms of amorphous CPs have also been recently reported. Through systematic, fast differential scanning calorimetry (DSC) analysis, different melting signatures T_m were found in P3HT, which was first melted and then rapidly quenched to different levels.[63] As expected, those samples that were quenched the quickest formed the least ordered structures. Such highly amorphous domains are characterized as the mobile amorphous fraction (MAF). More ordered

than the MAF, the rigid amorphous fraction (RAF) has been recently demonstrated by the Stingelin group. The RAF is thought to occur at the boundary of crystallites, where chains that are partially incorporated into the aggregate reside. Indeed, by quenching to temperatures of 30-120 ºC from above the melting temperature, there appears to be an additional melting curve that is larger than the <30 ºC quenched polymers that exhibited the MAF. This middle range of 30-120 ºC is attributed to the RAF and most likely appears in thin films of other semicrystalline CP.

These studies have been critical in expanding the understanding of thin film morphology, but there are still many gaps to be filled. Many of these analyses are being conducted on a bulk-averaged basis, meaning that the presence of different phases can be confirmed, but their location and origin are difficult to determine. Simulation models and design heuristics have been developed through a trial-and-error analysis of the highest performing conditions compared to initial conditions, rather than an *in situ* or otherwise systematic analysis of the spatially resolved morphology. The rest of this discussion will focus on elucidating the microstructural evolution of CP, the various processing and structural influences on that microstructure, and developing techniques for spatially resolved microstructural analysis.

Chapter 2. DEFECT TOLERANCE OF Π-CONJUGATED POLYMER CRYSTAL LATTICES

*The work in sections 2.2 – 2.6 has been previously published as an article: *ACS Appl. Polym. Mat.* **2019**, *1*, 1466–1475; DOI: 10.1021/acsapm.9b00223

2.1 BACKGROUND: CRYSTALLIZATION IN TRADITIONAL, NON-CONJUGATED POLYMERS

As has been established, the presence of defects in a thin film disrupts the crystalline structure and consequently its ability to transport charge carriers. However, the microstructural consequences of defects have not been fully explored for CP. One critical component to be determined is whether or not defects can be incorporated into the crystal lattice of CP. There has been a wealth of research onto this specific component for traditional, non-conjugated polymers, but has only received limited research for CP. In order to discern what models can also be used to describe CP crystallization, it is beneficial to first understand the non-conjugated counter parts they were developed for.

In the ideal, thermodynamically limited case, it is predicted that there is complete exclusion of defects from crystalline domains. As first formulated by Flory in 1955,[64] the effects of increasing the defect concentration in polymer samples is described by a reformulation of the Thompson-Gibbs equation, below:

$$\Delta T = \frac{RT_m T_m^{\infty}}{\Delta H_f} x_e \tag{2.1}$$

where ΔT is the difference between the melting onset and crystallization onset temperatures, R is the ideal gas constant, T_m is the observed melting point, T_m^{∞} is the melting point of an infinitely long chain, ΔH_f is the enthalpy of fusion for the crystal, and x_e is the molar fraction of crystallizable

units. So, in this ideal model, as defect concentration is increased, x_e is decreased, reducing the difference between the crystalline melt and the semicrystalline crystallization. Physically, what is happening is that as the defect concentration increases, more and more of the polymer has to be excluded into the amorphous domains, which decreases the crystalline fraction and the thickness of the crystalline lamellae. As discussed, there are much stronger intermolecular interactions in crystalline domains than in amorphous domains, so as the amorphous fraction increases, the total energy required to disrupt the intermolecular interactions and melt the film decreases.

In the years since the seminal foundations of Flory, there have been many reformulations of equation 1. Notably, in 1977, Sanchez and Eby investigated the thermodynamic effects of defect inclusion into the crystalline domains of non-conjugated homopolymers, block copolymers, and random copolymers.[65] They concluded that Flory was only partially correct, increasing defect concentration will increase the amorphous fraction and thereby decrease the lamellar thickness, however, there are further consequences. Although there is a thermodynamic preference for a perfect crystal, they define a case where defects containing polymer segments participate in the crystal (Figure 2.1). In this case, the defects introduce steric bulk into the crystal, which distort the planarity of the neighboring chains. The result of this lattice distortion is a weakening of the intermolecular interactions between the neighboring chains. Because of this decrease in intermolecular interactions for the crystal, it follows that the required energy to melt the crystal decreases as well, and that there is therefore a decrease in ΔH_f for the crystallite. So, in the case where defects can be partially included into the crystallite, ΔT in influenced by both the increase of the amorphous fraction and the decrease in ΔH_f for the crystalline fractions that contain defects.

Since these insights, researchers have been able to develop a much deeper understanding of the crystalline behavior of non-conjugated polymers. In particular, polyethylene (PE) has been the

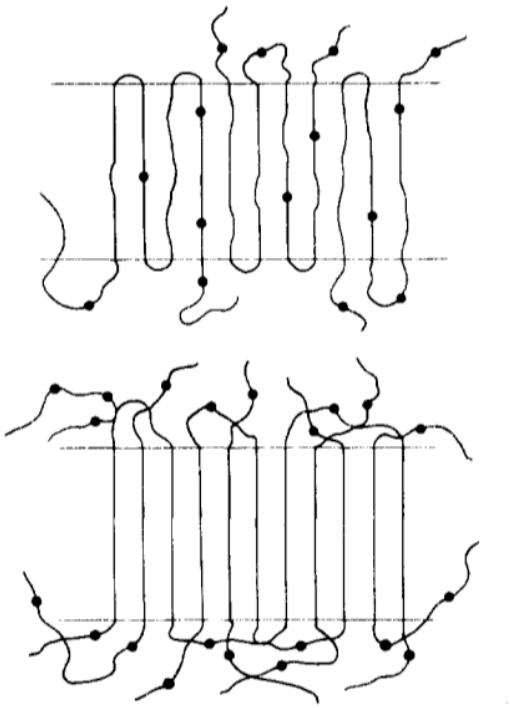

Figure 2.1. Schematic representations of (top) partial inclusion of defects and the resulting lattice distortions and (bottom) complete exclusion of defects.[65]

subject of much research. This is due to a few reasons, namely, PE is one of the simplest possible structures for polymers. This drastically simplifies analytical techniques like XRD or NMR, where increased structural complexity can cause increased complexity of signals produced and also reduces computational complexities for simulations. Additionally, PE is of high interest for industrial purposes and highly precise polymerizations have been developed, which have allowed for the widespread use of high-density PE (HDPE), low-density PE (LDPE), and ultra-high molecular weight PE (UHMWPE), among others. The results of these efforts have produced a bounty of experimental and theoretical knowledge. Phase diagrams of PE at high pressure and varied temperature and M_n have been developed, as well as on-equilibrium phase diagrams of flow-induced crystallization and melting of polyethylene, as just a few examples.[66,67] The crystal structure of PE throughout ranges of operating conditions and polymer profiles (e.g. M_n,

Đ, etc.) have been systematically developed and corroborated. Such an intimate knowledge of PE has been a significant achievement that has improved the implementation and understanding of PE and other non-conjugated polymers.

Recently, advances in simulation methods and techniques have also augmented efforts to understand polymer behaviors. Using all-atom molecular dynamics simulations, Zhang and Larson investigated the effects of the length of defect side-chains on the crystallization of PE oligomers of 50 repeat units. The study showed a severe decrease in crystallinity with the addition of a single methyl group, which continued to decrease as the side chain was increased to a hexyl group.[69] This result was compounded by their additional results from experiments looking at the effect of two methyl groups attached at various points along the chain. This study shows just how sensitive crystal structures and close-packing are to steric disruptions, even at low concentrations. Similarly, Verho *et al*. used large-scale atomistic molecular dynamics simulations to investigate crystalline lamella growth in a system of 3000 chains comprised of ~1000 repeat units.[68] It was found that lamellae tend to grow only from the ends of the parabolic front because of thermodynamic constraints, despite the fact that the smallest stems form at the growth front, are not stable, and tend to have short lifetimes. This is illustrated in Figure 2.2. In this context, 'stems' refers to straight, crystallizable segments of PE. It is only when thermal and conformational fluctuations grow the stems large enough that they begin to become thermodynamically stable and grow, which is ~4 nm for PE. Beyond this point, the stem grows until reaching a critical point, l_c, where it is no longer thermodynamically preferable to grow due to a lack of slack in the unincorporated stems. As a result, l_c corresponds to the lamellar width. The stems often attach in pairs, forming tight folds because the formation of a stem within an amorphous chains segment stretches it locally, causing another straight segment to form to compensate, which tends to become a stem as well.

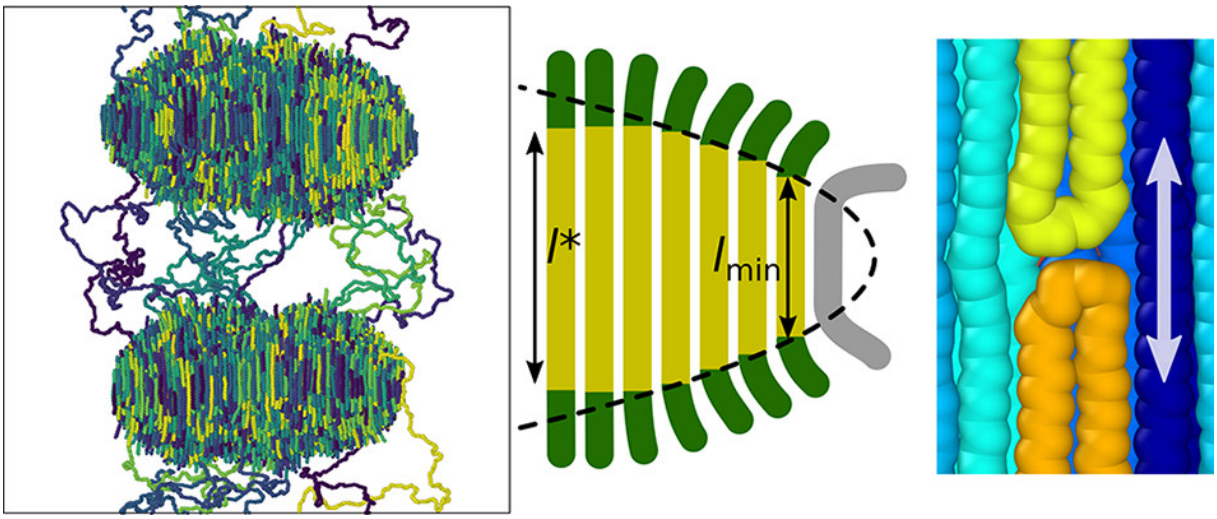

Figure 2.2. (left) Simulation results of PE lamellar growth. (middle) Thermal fluctuations create crystallizable stems of a minimum length needed to stably grow the lamella. (left) As stems grow in the crystal, slack from other stems propagates to account for the growth.[68]

Then, when the stems grow, they require slack length from the amorphous parts to be transferred to them. This often proceeds by diffusion of the slack through other stems in the chain. Additionally, this study was able to confirm assumptions about the origin of chain tilting in polymer crystals, which is considered to relieve steric bulk density at the crystal/amorphous interface and reducing entropy.[70]

There is some experimental validation to either treatment of defects, partial inclusion or complete exclusion. For instance, Wagener *et al.* have developed a highly precise method for synthesizing polyethylene (PE), Acyclic Diene Metathesis (ADMET), which allows for highly precise additions of defects along the backbone. By adding defects to every 21st unit, they were able to identify a clear boundary between defects that were able to be incorporated into the lattice (methyl and ethyl groups) and defects that were excluded into the amorphous layer (propyl to hexyl and even adamantyl groups).[71] Although the methyl and ethyl side-chain defects were able to binsert into the crystal structure, there were clear effects on the melting temperature, and therefore the lamellar

thickness, *l*, as determined by DSC. Specifically, *l* decreased from the pristine case to the ethyl-defect incorporated case, where the effect then began to saturate for the remaining samples. Because all samples had the same defect concentration and spacing, the saturation of the T_m is attributed to complete exclusion of the larger defects, where each sample has similar *l* and amorphous fractions. However, T_m of the ethyl and methyl samples were higher, with methyl being higher than ethyl. This is attributed to the fact that less amorphous fraction is generated as a result of the partial incorporation of defects, with a higher preference for incorporating smaller defects. Similar studies, with defects placed on every 39th unit, were conducted by the same group.[72] With the increased spacing between defects, it was found that even the ethyl groups were completely excluded from the crystalline lamellae. This serves to shed light on the impact of both defect size and spacing, or concentration, on their incorporation into crystalline domains. Smaller defects are much more likely to incorporated, as the enthalpic penalty for doing so is equally smaller. Interestingly, the comparison of defects on the 21st versus 39th units points to an increased tolerance of defect incorporation with less distance between defects, meaning higher defect concentrations, provided other defect types are suppressed, when backbone planarity can be maintained. These results highlight the sensitivity of crystalline lamellae in polymers to even small, planned defects. They also point to the ability to control crystal structure through precise modulation and choice of defects.

Looking at the direct impact of chemical defects along the backbone of polymers Puls *et al.* conducted a systematic study on crystallization of poly(ethylene oxide) (PEO) with the addition of defect moieties into the middle of the PEO chains. Different aryl groups were inserted into the middle of PEO oligomers and their crystals were studied by wide angle x-ray scattering and solid-state carbon NMR. It was found that chain tilting in the polymer crystal is essential for

compensating for these defects and that the angle of the tilt is correlated to the substitution of the aromatic group, as shown in Figure 2.3.[73] In fact, the authors demonstrated that, although the aromatic defects were initially excluded from the crystal lamella, annealing below the T_m caused the defect to be integrated into the lamella structure. The ability to tune the entire crystal structure, simply by planning few, mid-chain defects is expounded upon by Samiullah *et al.* in their work on PEO-triazole-$(CH_2)_n$-triazole-PEO crystals.[74] In that work, a PE separator between two triazole moieties was used to tune the morphology of the spherulites at different temperatures. Although there were significant contributions from the PE connector there was a noted dominance of the π-π interactions of the triazole moieties in determining the crystalline structure of the polymer.

These studies all indicate that the crystalline lamellae widths of polymers are influenced by a great many factors, such as molecular weight, defects, temperature, pressure, and much more. They also demonstrate that defect size, concentration, and ability to π-π interact, can be used to tune the crystalline structure and packing behavior to a high degree. Finally, there is evidence that π-π interactions are a dominant driving force polymer crystallization, even in non-conjugated polymers, which underscores both the fact that CP behave differently from non-conjugated polymers and the importance of understanding the crystallization behavior of CP. Although there

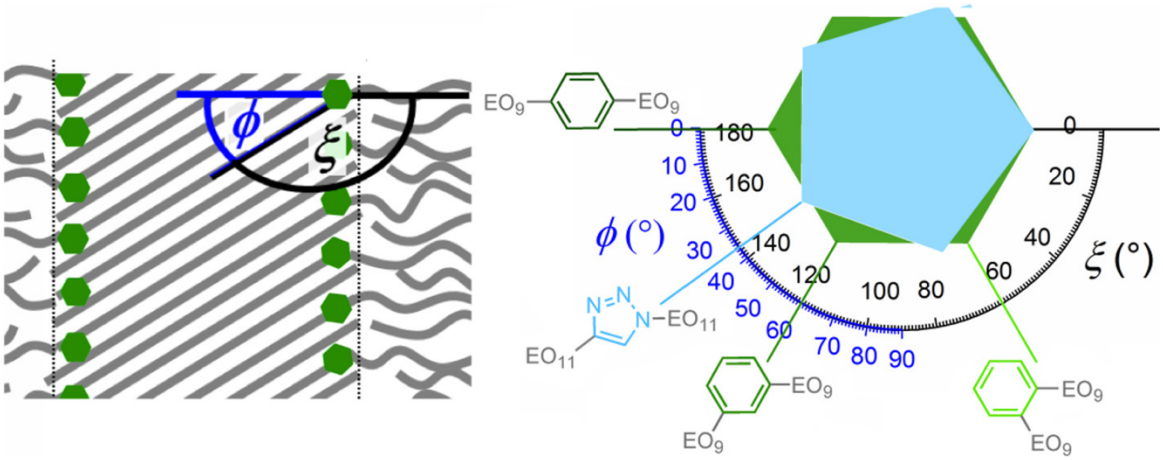

Figure 2.3. By inserting aromatic defects into the middle of PEO chains, the angle at which the polymers crystallize can be tuned via the substitution of the aromatic group.[73]

is rich literature behind the crystallization of non-conjugated polymers, it cannot be assumed that these concepts directly translate to or completely describe CP.

2.2 Chemical Defects in π-Conjugated Polymers

Although synthetic precision has drastically improved in the past years, defects in the chemical structures of CP are difficult to completely avoid.[75,76] Common imperfections, such as coupling defects during polymerization, dispersity in molecular weight, and end-groups, can disrupt crystallization and thereby affect many different material properties, including charge transport and mechanical stiffness. Such properties are also affected by processing conditions, which is beyond the scope of this study. The effects of chemical defects have been the subject of some study, particularly coupling defects.[77–82] In asymmetric monomer containing homopolymers, such as poly(3-hexylthiophene) (P3HT), this is defined as regioregularity (RR), which is the percentage of monomers coupled in the preferred head-to-tail (HT) conformation, rather than head-to-head (HH) or tail-to-tail (TT) conformations (Figure 2.4).

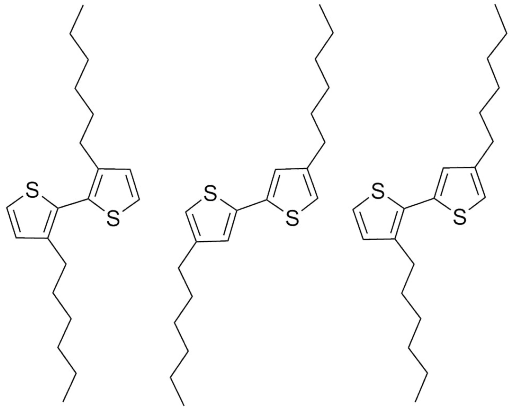

Figure 2.4. Regio-defects in P3HT: (left-to-right) HH and TT coupling, compared to the preferred HT coupling.

In order to relieve the steric interactions of the bulky side-chains, the incorrectly coupled monomers twist into a more *gauche* alignment, which reduces their p_z orbital overlap and disrupts π-conjugation along the backbone. This twist also reduces the ability of that polymer chain to pack closely with other chains, disrupting the crystal lattice and reducing crystallinity; such disruptions in crystallinity and orbital overlap are detrimental to charge conduction pathways in optoelectronic devices.[40–42] Coupling defects in donor-acceptor (D-A) copolymers can also include homo-couplings, which are beyond the scope of this investigation. Dispersity (*Đ*) in the molecular weight profile of the CP has been shown to also drastically reduce crystallinity because short chains have a higher concentration of end-groups per crystallizable monomer unit when compared to longer chains. What's more, CP of drastically different molecular weights have a tendency to crystallize differently, both with regards to crystal lattice dimensions and mechanism.[35,37,38,80,81,83] Finally, the effects of end-groups seem to be dependent on the type of end-group that is used. For instance, Kim *et al*. have shown that thin films of CPs with Br as an end-group have far less crystalline order than thin films from the same CP but with thiophene end-groups.[84] As seen in Figure 2.5, the common end-group, Br, has a van der Waals diameter of 0.37 nm, approximately the same size as the π-π stacking distance in P3HT, 0.38 nm. The introduction of this steric bulk disrupts close packing and, therefore, polymers with larger end-groups tend to have less order.[85–87] However, Koldemir *et al*. have shown that, despite being relatively large, toluene end-groups can actually serve to promote a higher degree of order in CP thin films than the same CP capped with H, the smallest possible end-group.[88] This was attributed to stronger aggregation in solution for the polymer capped with toluene-H end-groups.

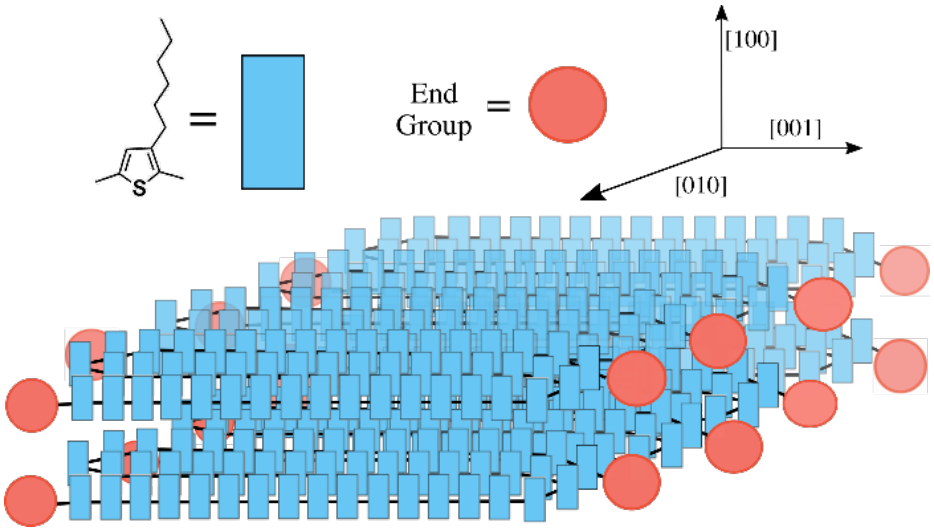

Figure 2.5. A representative diagram of a CP crystallite. Bulky end-groups can be similar in size to the intermolecular distance, which is disruptive to crystal growth.[89]

It seems apparent that the disruption of electronic properties and device performance and order tends to increase with the number of chemical structure defects in CP chains cast in thin films for devices, and further that these effects come as a result of changes in crystallinity and short-range order. Despite this, there have been relatively few investigations into understanding precisely why this occurs and where these defects reside in the thin film or how their location can be manipulated. In other words, there has been little investigation into how or why the defects affect the crystallinity. This is not the case for traditional, non-conjugated polymers, as an investigation into the role of chemical defects in crystallization began with a reformulation of the Thomson-Gibbs equation in 1955 by Flory.[64] The resulting equation described an ideal crystalline state that excluded defects completely into the surrounding amorphous domains so that the crystal lattice is preserved. In this ideal case, increasing the defect concentration also increases the amorphous fraction of the film as a result of more polymer being excluded from the crystals. This, in turn, decreases the crystal lamellar thickness, l_c. So, the melting temperature, T_m, is depressed by an

increasing defect concentration. Later, Sanchez and Eby further reformulated the Thompson-Gibbs equation to describe the more common case, where there is partial inclusion of defects into the crystal lattice, which tends to occur in kinetically limited processes.[65] Their reformulation includes an enthalpic penalty for the incorporation of defects, which distorts the crystal lattice and reduces intermolecular interactions, thereby lowering the enthalpy of formation, ΔH_f, for the crystal. In this model, T_m is decreased with increasing defect concentration as a result of both decreasing l_c and diminishing ΔH_f.

In the past few decades, researchers have developed a much deeper understanding of the crystalline behavior of non-conjugated polymers. In particular, polyethylene (PE) has been the subject of much research. This is due to a few reasons, namely, PE is one of the simplest possible polymer structures. This drastically simplifies analytical techniques like X-ray diffraction (XRD) or nuclear magnetic resonance (NMR), where increased structural complexity can cause increased complexity of signals produced, and also reduces computational complexities for simulations. Additionally, PE is of high interest for industrial purposes and highly precise polymerizations have been developed, which have allowed for detailed structure-property relationships to be constructed; phase diagrams of PE at different pressures and varied temperature and M_n have been developed, as just a few examples.[66,67] The crystal structure of PE throughout ranges of operating conditions and polymer profiles (e.g. M_n, $Đ$, etc.) have been systematically developed and corroborated. What's more, in-depth studies of local variations in crystallinity have shed light on semicrystalline polymer behavior.[90,91] Such an intimate knowledge of PE has been a significant achievement that has improved the implementation and understanding of PE and other non-conjugated polymers. For CPs, it has been difficult to even simply evaluate which defects are incorporated into the crystal lattice and the extent of their incorporation. This is because

of the difficulties associated with producing CP samples that have a range of discrete defect concentrations, and difficulties in analyzing the highly interconnected semicrystalline thin film structure of polymers.[92,93]

The complex nanostructure of polymer thin films is exemplified in Figure 2.6, which shows highly anisotropic, lamellar domains of crystalline polymer separated by amorphous domains that conform to Flory's model of complete exclusion of defects from the crystal lamellae.[36] According to that model, all the defects in the chemical structure, which are listed in Figure 2.6, would be excluded to or transported to the amorphous domains to preserve the short-range order of the crystal lattice. In the context of CPs, this means that regio-defects and end-groups would be expected to be excluded in such a model. Conversely, some or all types of defects could be incorporated into the crystal lattice in the model outlined by Sanchez and Eby. Because of the complex morphology of these thin films, it has been difficult to determine which model most accurately describes CPs. In order to reduce the complexity of the CP morphology, we used self-assembled nanowires of P3HT that were produced through the whisker method.[94] The precipitation of these nanostructures from a poor solvent is a kinetically limited process, meaning that it can still be used to probe the aggregation and close-packing of thin films produced using faster processing methods, such as spin-coating or blade-coating. However, the polymer chains in the nanowires are also able to reach a much more thermodynamically stable conformation because they age in solution for up to 72 hours, as presented in this investigation. The use of these nanowires allows for the examination of an upper threshold in the kinetically limited defect tolerance of crystalline domains, with minimal interference from amorphous domains. In order to precisely alter the defect concentration, we utilized our previously established synthetic routes for producing P3HT with high control over RR, molecular weight, $Đ$, and end-groups.[75] This allows

for nanowires to be made from P3HT with a range of defect concentrations and to have the resulting crystal structure examined. By examining different series of nanowire samples, we were able to identify the location of regio-defects and end-groups in highly ordered structures and elucidate the connections between the defects and their effects on material properties in a generalized manner.

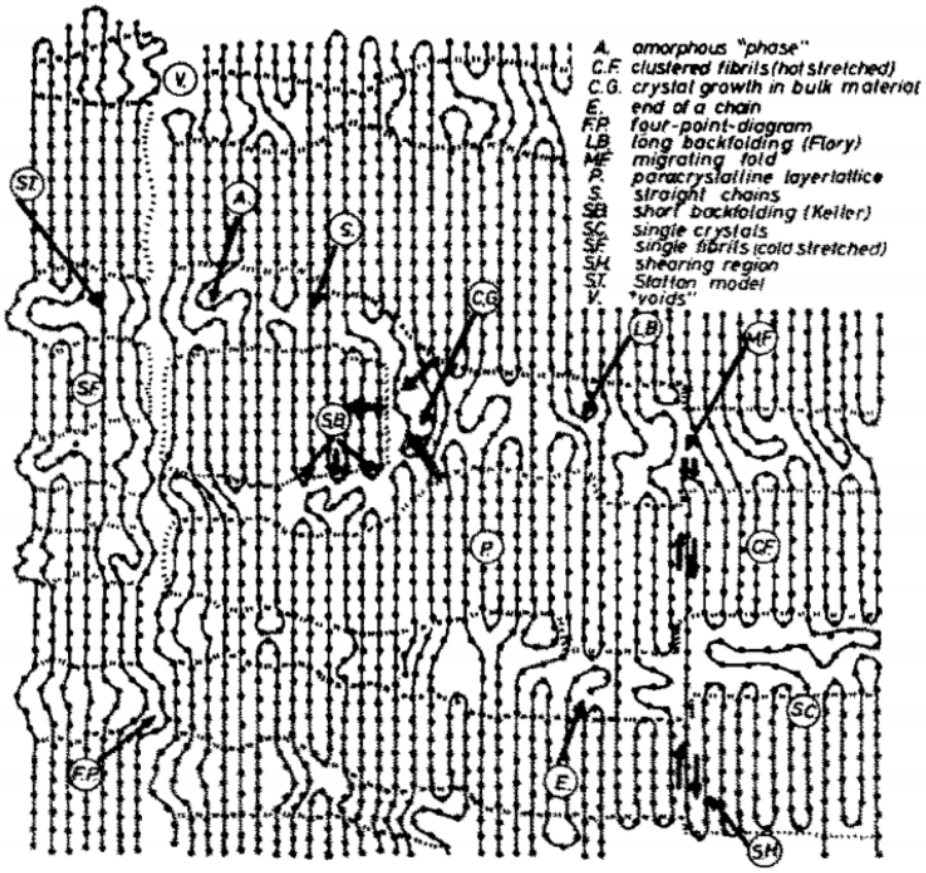

Figure 2.6. A top-down view of thin film morphology for traditional polymers following Flory's model of complete exclusion, with lamellar crystalline domains separated by amorphous domains and the defects only residing in the amorphous domains. As shown in this figure, the amorphous regions (A) contain all of the chemical defects, including short backfolds (SB), long backfolds (LB), chain ends (E), voids (V), migrating folds (MF), and Statton model (ST) defects, as well as the beginnings of new crystallites (CG). Depending

on processing, crystalline domains can be single fibrils (SF), clustered fibrils (CF), paracrystalline layerlattice (P), or single crystals (SC). Shown also are shearing region defects (SH) to the crystal lattice. Reproduced with permission. Copyright 1963 AIP Publishing LLC.[36]

2.3 Materials and Methods

2.3.1 *Materials*

All solvents and materials were purchased from Sigma-Aldrich and used as received, unless otherwise noted. Commercial P3HT was purchased from Rieke Metals (4002-E).

2.3.2 *Nanowire Production and Isolation*

Self-assembly of the nanowires was conducted via the whisker method. P3HT was either synthesized using previously described methods[75] or purchased and was added to anhydrous anisole at a concentration of 2 mg/mL under a nitrogen atmosphere in a glovebox. In order to ensure complete dissolution, the solution was heated and stirred at 110 ºC for 24 h, after which the heating and stirring was stopped and self-assembly was allowed to progress for 24, 48, or 72 h. The nanowire solution was then removed from the glovebox and transferred into a Teflon centrifuge tube and centrifuged for at least 3 cycles of 30 min at 12000 rpm in a Beckman-Coulter Allegra x-22 centrifuge. In between cycles, the supernatant anisole, which contains the unincorporated P3HT, was removed and replaced with fresh anisole. The supernatant from the first cycle was saved for analysis. When the supernatant anisole became clear and colorless, the remaining nanowires were transferred to a vial and dried under vacuum (~1 mTorr) on a Schlenk line.

2.3.3 *Size Exclusion Chromatography*

Size exclusion chromatography (SEC) was performed using a Malvern Viscotek TDA 305 GPC, coupled with a UV and Refractive Index (RI) detector with a polystyrene column and an anhydrous tetrahydrofuran (THF) eluent. This combination of light scattering, light absorption, and viscometry measurements allows robust detection of both low and high molecular weights. The injected solutions had a concentration of 1.0 mg/mL and a volume of 100 μL with a flow rate of 1 mL/min and detector temperature of 30 ºC. In order to determine M_n and M_w values for the samples, a light scattering method was employed using three different light sensors, allowing for an absolute determination of chain lengths. To use this universal calibration method, a dn/dc of 0.28 mL/g was experimentally determined and used. In tables S1-S3, DP was calculated from the M_n.

2.3.4 *^{1}H Nuclear Magnetic Resonance*

The nanowires were dissolved in deuterated chloroform at a concentration of at least 2 mg/mL. These samples were then analyzed using a Bruker AV-500 spectrometer and at least 256 scans were taken. RR was determined by comparing the HT coupling to the HH and TT coupling peak. DP was calculated in the case of the toluene-/-H polymers, by comparing the relative peak areas for the methyl protons on the toluene and the α- carbon protons on the hexyl side-chains of the polymer backbone. DP is reported from the calculated M_n of the measurement. ^{1}H NMR (500 MHz, $CDCl_3$): δ 6.98 (s, 1H), 2.80 (t, 2H, J = 7.7 Hz, head-tail coupling), 2.61 (t, 2H, J = 7.6, head-head, tail-tail coupling), 1.71 (quint, 2H, J = 7.6 Hz), 1.48-1.38 (m, 2H), 1.37-1.30 (m, 4H), 0.91 (t, 3H, J = 7.2 Hz).

2.3.5 *Matrix Assisted Laser Desorption/Ionization – Time of Flight (MALDI-TOF)*

MALDI-TOF measurements were made using a Bruker Autoflex II spectrometer. A terthiophene sample matrix was used and deposited *via* capillary tube. The samples were prepared by dissolving 1 mg/mL of P3HT into chloroform and depositing a small amount of the solution on top of the terthiophene matrix via capillary tube, following the protocol for the spot-then-spot method.

2.3.6 *X-Ray Diffraction (XRD)*

Nanowires were suspended in isopropyl alcohol and drop-cast onto sonicated and plasma-cleaned glass substrates. XRD analysis was performed on a Bruker D8 Discover in a small angle configuration.

2.3.7 *Differential Scanning Calorimetry (DSC)*

DSC was performed on a TA Q200 using aluminum sample pans. A heating trace from 30 – 300 ºC at a rate of 10 ºC/min was collected under a nitrogen purge flow. At least 3 mg was examined from each sample.

2.3.8 *PeakForce Quantitative Nanomechanical Mapping Atomic Force Microscopy (QNM)*

Freshly prepared and non-isolated nanowires were spin-coated onto cleaned and passivated silicon substrates. Substrates were cleaned by scrubbing with soap and DI water, followed by sonication in DI water, acetone, and isopropyl alcohol for 15 min each. Following sonication, the substrates were dried under a stream of air and subsequently plasma cleaned for 15 minutes using O_2 plasma. To passivate the substrates, the substrates were taken directly from the plasma cleaner placed under vacuum with an open vial containing 400 μL of octadecyltrichlorosilane (OTS). The system remained under dynamic vacuum for 1 hour and was then switched to static vacuum. The

system was heated at ~125 ºC for at least 3 hours. After this, the heat was turned off and the system was allowed to rest under static vacuum over night for vapor deposited, self-assembled monolayer OTS. AFM micrographs were obtained on a Bruker ICON AFM in Peakforce QNM mode. ScanAsyst-Air tips were used for these measurements (SiN/Al, ~70kHz, and 0.4 N/m). Measurements of nanowire widths and heights were taken from these micrographs. At least 100 nanowires from at least 3 different micrographs were measured and averaged to determine the reported heights and widths of the nanowires.

2.3.9 *Amplitude-Modulation, Frequency-Modulation Force Microscopy (AMFM)*

AMFM measurements were performed on an Asylum Research Cypher-ES system. For AM-FM Viscoelastic mapping we used built in routines provided by Asylum Research and µMasch tips (HQ:NSC18/Pt, ~75 kHz, and 2.8 N/M). All measurements were performed in a nitrogen environment.

2.4 Results and Discussion

In our prior work, we had shown that nanowires can be successfully created using P3HT that has RR as low as 93% with bulky Br end-groups, which is considered to be a higher defect concentration than desired for many device applications.[40] Increasing the RR was shown to promote the crystal coherence in the π-π direction, but the location of these defects in the nanowire structure was not investigated. As shown in Figure 2.7, there are two nanowire structures that could be expected to form. Model A follows Flory's model and assumes that all of the defects are being excluded to the perimeter of the nanowire, where the amorphous domain is expected to exist. If this case is the correct description, then it follows that increasing the concentration of defects would decrease l_c and increase l_a as more polymer is excluded from the crystalline domain. This

differs from model B, where some defects are incorporated directly into the crystal lattice at the expense of the ΔH_f for the crystal, as described by Sanchez and Eby. In this case, l_c would vary significantly less than in model A and the total width of the nanowire would remain the same, since the increase in the amorphous fraction of the nanowire would be diminished by defect inclusion. So, if both l_c and the width of the nanowire (l_c+l_a) remain constant, then model B would correctly describe the treatment of defects by the crystal lattice.

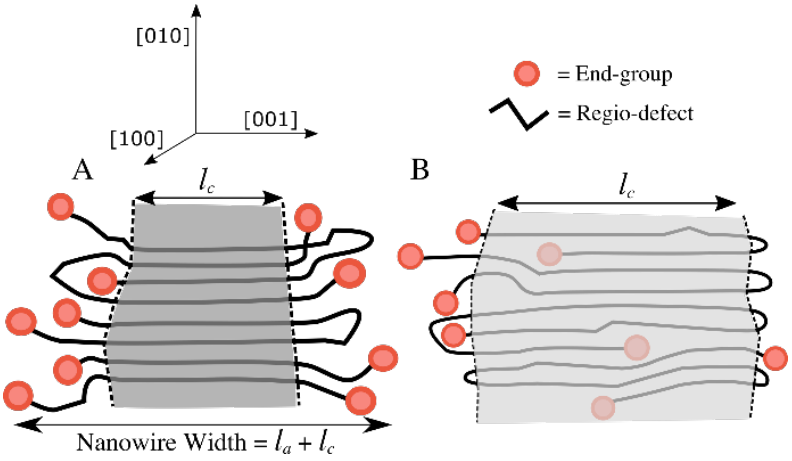

Figure 2.7. Proposed nanowire structures for the cases where there is either (A) complete exclusion of defects or (B) partial inclusion of defects into the crystal lattice. Darker grey indicates higher crystallinity.[89]

As an initial investigation into defect tolerance at high defect concentrations, nanowires were formed from commercially available P3HT, following the procedure outlined in the supporting information. In order to identify the preferential inclusion or exclusion of defects during nanowire formation, the P3HT that was unincorporated into the nanowire, which remained in solution during centrifuging, was analyzed and compared to the nanowire incorporated P3HT. As seen in Figures S2.1-S2.7 and summarized in Table S2.1, the nanowire self-assembly process tends to exclude polymers with RR below ~90%. This is assumed to occur because chains with lower RR present

too many backbone torsions to successfully fold and close-pack with other chains in such a highly ordered nanostructure.[95] Similarly, there was a decrease in the number of Br end-groups that were incorporated into the nanowires. This is identified by a suppression of the Br-H peaks in the MALDI-TOF spectra shown in Figures S2.8, S2.10, and S2.12 compared to Figures S2.9, S2.11, S2.13, and S2.14. This is summarized in Table S2.1, where it is apparent that there is a much smaller Br-H:H-H end-group ratio for the nanowire incorporated P3HT than the unincorporated and as-purchased P3HT. Finally, there was an exclusion of chains with a degree of polymerization (DP) of less than approximately 50 monomer units. Interestingly, this apparent threshold corresponds to l_c as determined by differential scanning calorimetry (DSC) and outlined in Table S2.1. The observed tendency to incorporate integer multiples of l_c will be explored to a greater extent below. The SEC analyses of these nanowires seem to indicate preferential exclusion of long chains from the nanowire, however, the most likely explanation for this result is that the longest chains were not solvated adequately by the anisole, which is an intentionally poor solvent for P3HT, during the self-assembly process, inhibiting their participation in nanowire formation. These results complement the findings of Roehling *et al*., which identified the preference to exclude smaller chains during nanowire formation, in part to reduce end-groups in the nanowire structure.[95] As the aging progressed, there was a noticeable increase in the ΔH_f of the nanowires, which is attributed to the increased time to approach a thermodynamically preferred, highly crystalline state.[95] Despite this increase in the crystallinity, there was no observed increase in l_c, as determined by the Broadhurst equation (Equation 2.1) and the peak melting temperature, located using DSC (Figure S2.15).[38]

$$T_m = T_m^o \frac{n+a}{n+b} \qquad (2.1)$$

In the above equation, T_m is the observed melting temperature peak, T_m^o is the melting point of an infinite crystal of P3HT, n is the number of repeat units the crystal is wide in the [001] direction, and a and b are constants. In addition to constant l_c, there was no observable difference in the heights or widths of the nanowires, as measured by AFM (Figure 2.8), nor in the coherence in the [010], π-π stacking direction, $\xi_{(010)}$, as determined by Scherrer analysis of the XRD spectra shown in Figures S2.17-S2.19.

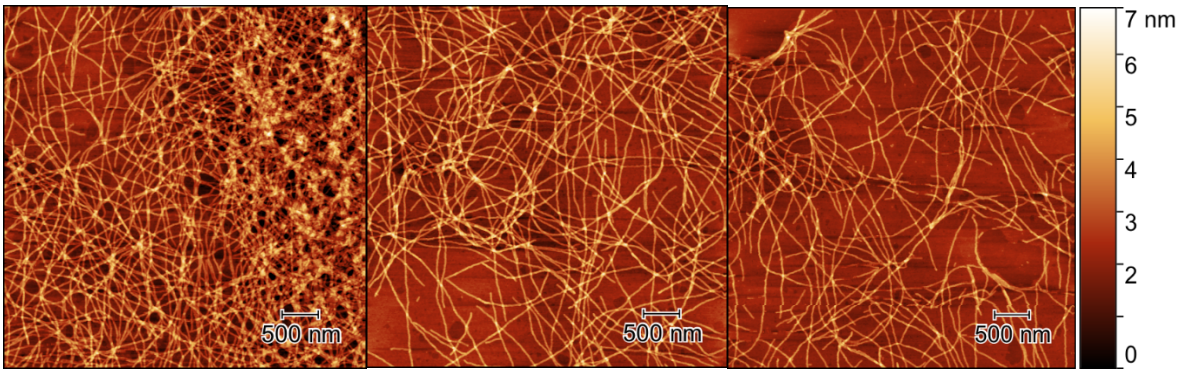

Figure 2.8. A representative PeakForce AFM image of P3HT nanowires that are aged (left-to-right) 24, 48, and 72 hours. Scale bars are all 500 nm. As seen in these height scans, and described in Table S1, there are no differences in the dimensions of the nanowires in these three different samples.[89]

So, despite the fact that there is inclusion of defects into the nanowire structure at different concentrations for the different aging times, there are no observed differences in the dimensions of the nanowire nor in l_c. This lack of variation in the width of the nanowires and l_c occurs despite differences in ΔH_f, which is illustrated clearly in Figure 2.9, which plots nanowire width and l_c as well as ΔH_f as a function of nanowire age.

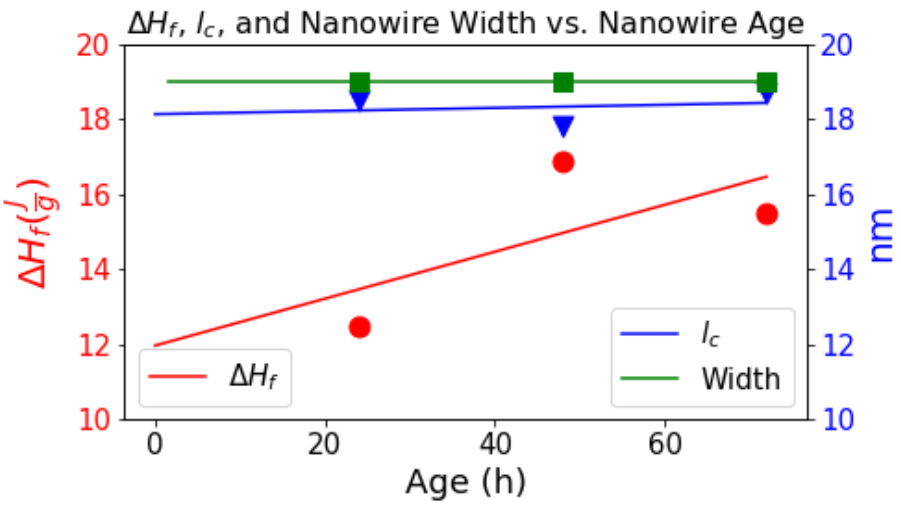

Figure 2.9: A plot demonstrating that, despite differences in the crystallinity that result from varied defect concentrations, there is little difference in the nanowire widths and l_c for the different samples. Linear fits provide visual guides for the data. Error in the data is associated with instrumental precision. These results are more completely shown in Table S.2.1.[89]

The fact that nanowire width and l_c remain constant, despite clear differences in defect concentration and ΔH_f demonstrates that regio-defects and bulky end-groups can be incorporated to some degree in the nanowire crystal lattice. These defect-induced distortions in the crystal lattice are evidenced in the UV-vis absorption profiles across the different nanowire ages, as show in Figure 2.10. In order to evaluate the different levels of lattice distortions and the relative degrees of *H*-like and *J*-like coupling, following the Spano model. [32–34,40] These properties are found through the ratio of the two identified peaks in Figure 2.10, $A_{0\text{-}0}$ and $A_{0\text{-}1}$, which are shown to give insight into the relative degrees of intra- and inter-chain order by Equation 2.2, below:

$$\frac{A_{0-0}}{A_{0-1}} \cong \left(\frac{1 - 0.24W/\hbar\omega_0}{1 + 0.073W/\hbar\omega_0}\right)^2 \qquad (2.2)$$

Where W is the free exciton bandwidth, in this case equal to 4 times the cofacial intrachain Coulombic coupling, J_0, assuming the Huang-Rhys factor is 1. Finally, $\hbar\omega_0$ is 180 meV, which is the energy of the primary vibronic mode associated with electronic transition in P3HT, symmetric ring stretching.[40] As shown in Figure 2.10, and detailed in Table S2.1, $A_{0\text{-}0}/A_{0\text{-}1}$ increases with age, indicating that there is more short-range order, *e.g.* backbone planarity and close-packing, in the nanowires as they approach a more thermodynamically limited structure. However, there was still a high degree of defect exclusion observed both for regio-defects and end-groups, which points to a limit in the inclusion of these defects. As such, the extent to which these individual defects can be incorporated into the crystal lattice and the consequences of that inclusion need to be determined.

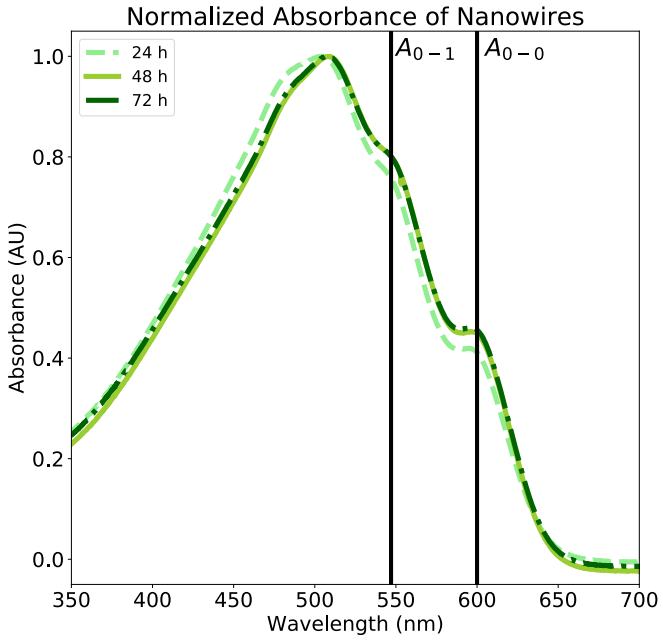

Figure 2.10. An overlay of the normalized UV-vis absorption spectra for the 24, 48, and 72-hour aged Rieke P3HT nanowires. The absorption peaks corresponding to the 0-0 and 0-1 transitions are marked reference. As seen in above plots, as age increases, so does the $A_{0\text{-}0}/A_{0\text{-}1}$ ratio, signifying more backbone planarity and increased short-range order.[89]

In order to examine the effects of regio-defect incorporation, a series of nanowires made from P3HT with increasing RR were examined, while holding the aging time, molecular weight, $Đ$, and end-groups constant. In these samples, the end-group is Br-H. The results of these experiments are seen in Table S2.2 and summarized in Figure 2.11. By increasing the RR of the P3HT from 93% to 99%, $\xi_{(010)}$ was increased by as much as 5-times the original value. Despite this drastic increase in crystalline order, there were still no observed changes in the dimensions of the nanowire or l_c, confirming that the regio-defects were incorporated into crystal lattices. By comparing the two 93% RR nanowires, Table S2.2 also shows that larger $Đ$ disrupts the crystallization and corresponds to a decrease in $\xi_{(010)}$, further confirming the observation by Roehling *et al*. that nanowire formation preferentially incorporates a narrow $Đ$ of CP to preserve crystalline structure.[95] Although these defects do not alter the dimensions of the nanowire or l_c, their incorporation reduced the hole mobility, μ_h, by almost 2 orders of magnitude, pointing to the disruption of the crystal lattice and short-range order and corroborating our observed trends in $\xi_{(010)}$, shown in Table S2.2.[40] These experimental results are in keeping with simulations, which have predicted the increase in trap states and paracrystallinity as RR diminishes.[78,96] Therefore, despite the ability of regio-defects to be incorporated into the crystal lattice of CP, there are corresponding distortions of the crystal lattice and reductions in short-range order and optoelectronic properties.

Table S2.1 indicated that there is a preference to exclude bulky end-groups, but that they are still incorporated into the nanowire. Additionally, there was an observed preference to incorporate P3HT with a DP corresponding to integer multiples of l_c. In order to investigate these trends and the extent to which DP can be used to tune the incorporation of end-groups, a series of nanowires

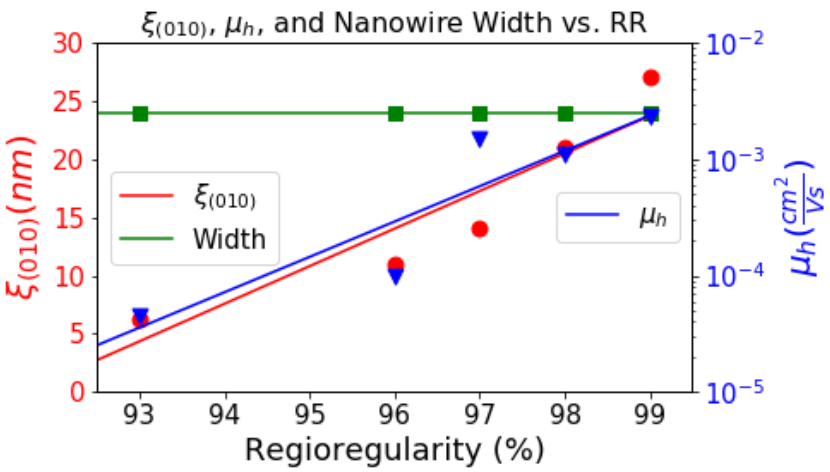

Figure 2.11: A plot generated from data in Table S2.2. The hole mobility, nanowire width, and $\xi_{(010)}$ are plotted as a function of regioregularity. Linear fits provide visual guides for the data. Error in the data is associated with instrumental precision. Changes in regioregularity have drastic effects on the short-range order of the nanowires, as measured by both XRD and OFET mobility.[89]

made from highly regioregular P3HT with $Đ$ below 1.3 were made. These P3HT samples were all synthesized with toluene-H end-groups, because the toluene moieties were expected to be able to participate in the π-π interactions of the crystal lattice, which was anticipated to increase the incorporation of the end-groups by decreasing their distortion of the crystal lattice. Further, to investigate the role of DP in the incorporation of end-groups, the nanowires were formed from different P3HT samples with DP corresponding to multiples of the l_c that was noted in Table S2.1, which was 50 monomer units. The predicted nanowire structures resulting from integer (harmonic) and non-integer (non-harmonic) multiples of 50 monomer units are displayed in Figure 2.12, the results of the analysis of the nanowires are shown in Table S2.3.

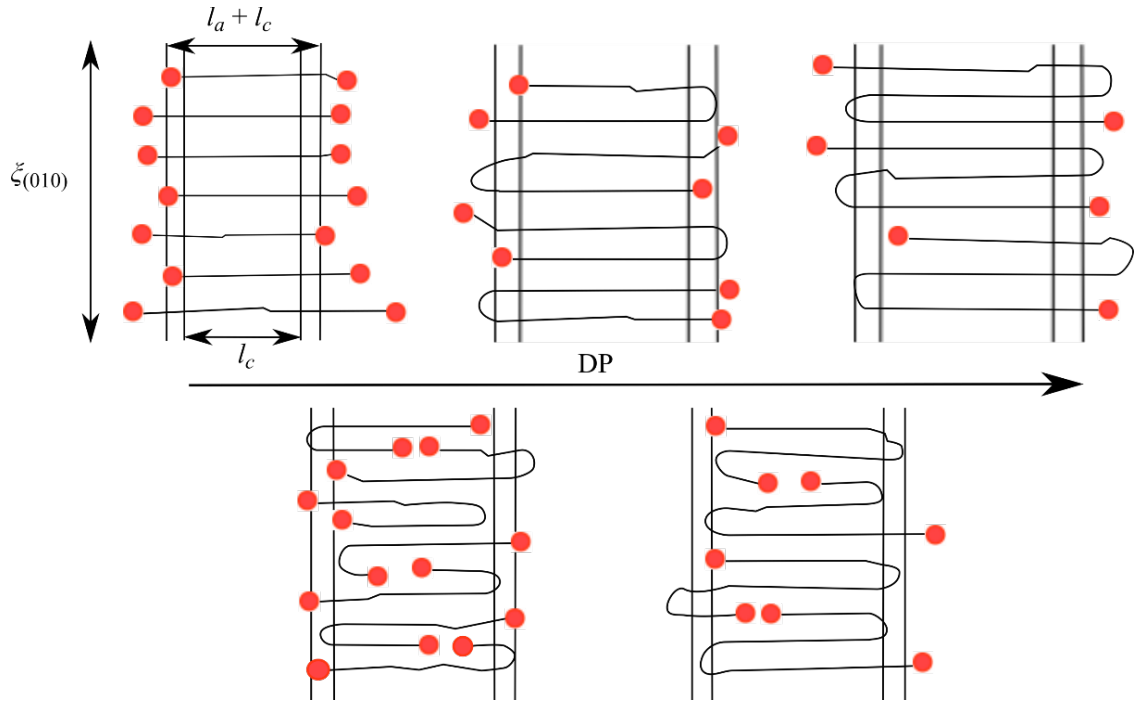

Figure 2.12. Predicted structures of the nanowires that are described in Table S3, with (top, left to right) DP = 50, 100, 150 and (bottom, left to right) DP = 75, 125. l_c remains relatively consistent for all samples above DP = 50.[89]

The nanowires that had the smallest observed l_c were those made from the DP = 50 P3HT, whose l_c neatly corresponded to the full DP of the P3HT, as shown in Table S2.3. This smaller l_c is evidenced by the depression of the melting point of the 50 DP nanowires, relative to the other samples, seen in Figure S2.20. This smaller l_c was in keeping with our predicted structure because 50 DP is at the approximate transition between chain-extended and chain-folded P3HT, so the chains were expected to stack, rather than fold, as shown in Figure 2.12.[38] As the DP increased beyond 50, the chains folded during nanowire formation and there was a slight increase in the observed l_c of the nanowires, shown in Table S2.3. This increase is attributed to the ability of π-π interacting toluene end-groups to be incorporated into the crystal lattice, which allows for more monomer units to participate in the lattice, lengthening l_c and, particularly for harmonic DP,

increasing ΔH_f, as seen in Figure 2.13. We note here that this helps explain the observation made by Koldemir *et al*. that toluene-H capped polymers have stronger aggregation in solution.[88] Because there is less disruption of the crystal lattice and more crystallizable units when toluene-/-H end-groups are used in the nanowires, as opposed to bromine-/-H, CP chains can more strongly interact with each other when π-π interacting end-groups are utilized.

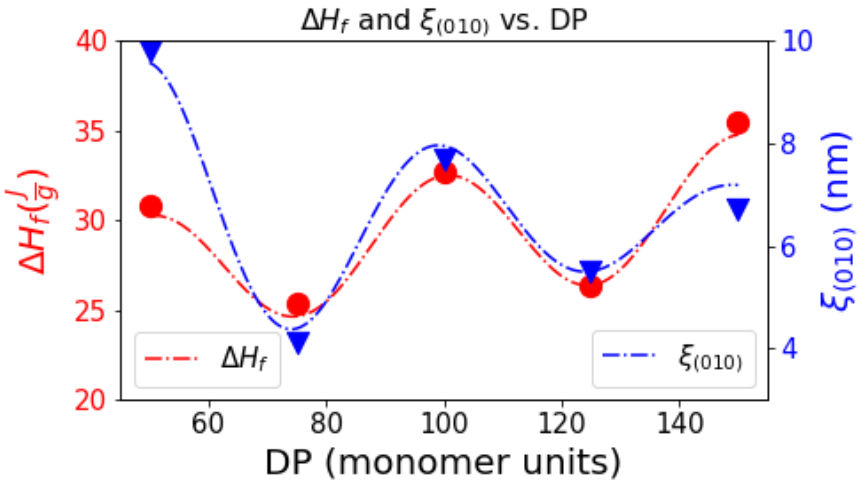

Figure 2.13: A plot showing the enthalpy of fusion and coherence *versus* DP for a series of P3HT nanowires, described in Table S2.3. Error in the data is associated with instrumental precision. This plot illustrates the effects of harmonic vs. non-harmonic DP on the crystallinity and short-range order of nanowires. Sinusoidal curves are fitted to emphasize the role of DP on the incorporation of end-groups.[89]

For non-harmonic DP, the l_c also corresponds to our predicted folding patterns, which incorporate the end-groups much more often, thereby decreasing ΔH_f. In the DP = 75 nanowires, the l_c is 67 monomer units, which can be constructed from ~35 monomer unit-long halves of two different chains in the same row. So, with each chain folded into 35 unit halves and ~5 folding units, which are excluded from l_c,[97,98] 35+35+5 = 75, which corresponds to our chain length. The units in the fold of the polymer are excluded from l_c because they are in the all *cis* conformation,

which disrupts conjugation in between those units by reducing *p* orbital overlap.[98] This folding structure is graphically described in Figure 2.12. Similarly, for P3HT of DP = 125, the l_c is equal to the remaining units of two different chains after folding twice, with 5 folding units in each chain being excluded from l_c, as shown in Figure 2.12. Because their end-groups cannot be neatly excluded to the nanowire edge, they are incorporated into the lattice and disrupt intermolecular interactions, reducing ΔH_f, so that the long-rang order of the nanowire structure is preserved. Further, because the DP = 125 nanowire has complete folds between the incorporated end-groups, its ΔH_f is larger than the DP = 75 nanowires. As expected, nanowires that incorporate end-groups into the crystal lattice display markedly lower ΔH_f as a result of the lattice distortion introduced by the end-groups and decreasing crystallinity by as much as 20% from nanowires made from P3HT chains that can neatly stack with end-groups at their edges. When the DP is increased from 50 by integer multiples of l_c to 150, the ΔH_f grew from 30.8 to 35.5 J/g. Interestingly, despite the increase of ΔH_f, there was an observed decrease in $\xi_{(010)}$ with larger integer multiples of 50, which is visible in the diminishing (010) peaks in Figures S2.21-S2.25 and Figure 2.13 as DP increases for harmonic DP. This is attributed to the fact that there are more chain folds required for these longer lengths. As the number of required folds increases, the likelihood that a folding or stacking fault occurs also increases, thereby decreasing $\xi_{(010)}$. Because the DP = 50 polymers did not have to fold, it is reasonable that those nanowires have the highest coherence, since crystals grow by first appending the stem and adsorbing units *via* rearranging and 'reeling' in segments to the crystal growth face. Once adsorbed to the width of the growth face, the remaining polymer folds to adsorb, creating more opportunities for crystallographic faults.[68,99]

So far, we have demonstrated that defects in the chemical structure of P3HT can be incorporated into the crystal lattice, but that the type of defect and its steric bulk influence the extent of its

disruption of the crystallization and final structure. Specifically, polymer chains with <10% regio-defects and aromatic end-groups are readily incorporated into the crystal lattice. In general, we have also seen that the presence of defects frustrates crystallization, with bulkier defects being excluded to a greater extent because they reduce structural coherence and short-range order more severely. As a result, defects that can interact favorably with the lattice are more readily incorporated and can be used to modify and promote short-range order, as with the toluene end-groups. To directly observe these effects, we formed nanowires from 3 different P3HT samples and probed their structure using amplitude-modulated, frequency-modulated (AMFM) force microscopy, a bimodal AFM technique that is capable of simultaneously measuring the Young's modulus (E) of a material and topography with a resolution on the 10 nanometer scale (Figure 2.14).[100,101] AMFM has previously been used to distinguish between crystalline and amorphous regions of P3HT thin films.[102] In order to distinguish the different polymer samples, they will be referred to by their defect types and concentration following the convention: (end-group)-(DP)-(RR)-(dispersity). So, Tol-200-100-narrow has the lowest defect concentration with toluene-H end-groups, a DP of 200 (an integer multiple of l_c), RR = 100%, and a narrow $Đ$ of 1.1. Br-275-98-narrow has a slightly higher defect concentration, having bulkier Br-H end-groups, a DP = 275 (a non-integer multiple of l_c), RR = 98%, and with a narrow $Đ$ of 1.2. Finally, Br-150-91-wide is commercially available P3HT with a higher concentration of defects, having Br-H end-groups, a DP of 150, RR = 91%, but with a wide $Đ$ of 1.8.

The topography scans (Figure 2.14, A-C) show nanowires with similar dimensions between each sample, however, the nanostructure of the nanowires is different for each sample. Tol-200-100-narrow nanowires exhibit large crystal grains in many different nanowires, which are represented

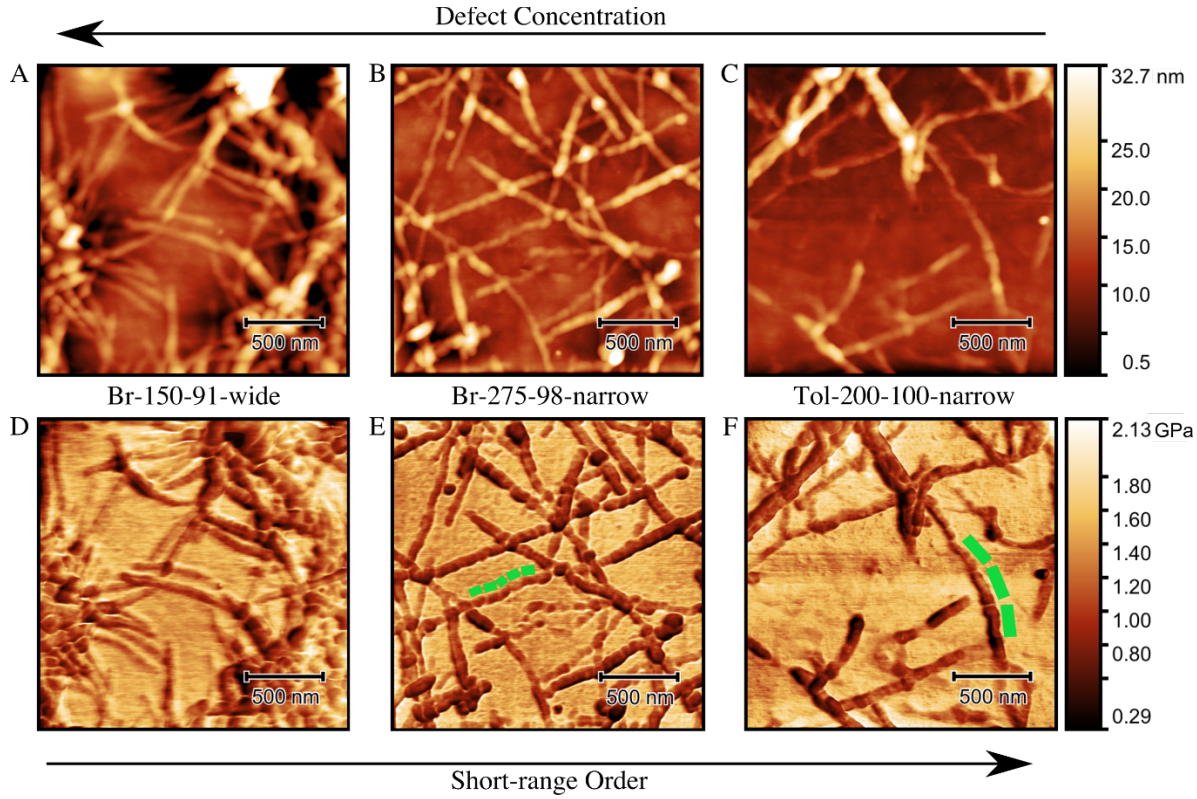

Figure 2.14. (A-C) 2 × 2 μm topographical scans of nanowires formed from Tol-200-100-narrow, Br-275-98-narrow, and Br-150-91-wide (right-to-left). (D-F) Young's modulus scans of the same nanowires. All images are from AMFM scans, all scale-bars are 500 nm. Larger segments are seen in nanowires made from P3HT with lower defect concentrations and π-interacting end-groups. As indicated, defect concentration increases from right-to-left, and short-range order increases from left-to-right. The length of segments, or crystal grains, in the nanowires are denoted in E and F with green rectangles. Grain size increases as defect concentration is reduced.[89]

with green rectangles in Figure 2.14 F. Br-275-98-narrow nanowires also show crystal grains in many of its nanowires, also highlighted with green rectangles in Figure 2.14 E, but these appear much smaller than those shown in the Tol-200-100-narrow sample. While there are visible grain segments at these low defect concentrations, there are no discernible crystal grains in the Br-150-

91-wide nanowires. In fact, the nanowires in Figure 2.14 A and D are remarkably homogeneous. The root-mean-square roughness (r_{rms}) of line-scans along the nanowires' long-axis reflects these observations. The Br-150-91-wide nanowires had the smallest r_{rms} variation in both height and modulus, (0.3 ± 0.1 nm, and 0.05 ± 0.01 GPa variation) these nanowires have few distinguishable structure features along their backbones. Tol-200-100-narrow nanowires were the next smoothest (rms roughness in height 0.4 ± 0.1 nm and rms variation in modulus 0.08 ± 0.008 GPa). These nanowires had the larger crystal grains and some fluctuations in the *E* within the grains. Finally, the Br-275-98-narrow had similar r_{rms} in height, but the largest variation in modulus (0.4 ± 0.2 nm and 0.09 ± 0.03 GPa). This follows, as the Br-275-98-narrow nanowires have smaller segments and, correspondingly, more grain boundaries, as well as some fluctuations in *E* within the nanowire segments. The differences in nanowire structure are ascribed to two main effects of the defects– slowing crystal growth and the disruption of short-range order. As examined above, the incorporation of defects slows down crystal growth by reducing the inter-chain interactions of crystallizing stems.[68,73] Since the NWs grow from the end by attaching stems, the termination of a grain would come from either the lack of stems with low enough defect concentration to participate in crystallization, or the presence of defects and the leading edge frustrating further stem appending.[68,99] So, following this, the area between the grains corresponds to a thin bridging layer of P3HT that was still able to crystallize. This description is confirmed by observing that the height of these inter-grain domains are ~2 nm, which corresponds to 1 vertical layer of P3HT.[98]

Of the three imaged polymers, Tol-200-100-narrow had the fewest defects to incorporate, so its nanowire growth was minimally disrupted, short-range order remained high, and large grains were able to grow. Br-275-98-narrow also had relatively few defects, but its DP was non-harmonic, so the bulky Br end-groups were forced to incorporate more often into the nanowire structure. As a

result, the grain growth was interrupted more often, and the grains were correspondingly smaller. Finally, the Br-150-91-wide had a high concentration of regio-defects, bulky end-groups, and a large $Đ$. This means that its crystal grain growth was slow because it was interrupted by defects often. As a result, the coherence in the [010] direction is minimized and any boundaries between the small grains are nearly indistinguishable from the rest of the nanowire.

These differences in nanowire structures are more clearly visible in Figure 11 D-F, which show the corresponding E scans of the nanowires. These scans are essentially a measure of the strength of the intermolecular interactions in the nanowires, which can be used to evaluate and describe differences in the local crystallinity of the polymer.[103,104] As noted above, the Br-150-91-wide nanowires are much more homogenous than the other two samples, resulting from the slow and frustrated crystal growth. Conversely, the Br-275-98-narrow nanowires are largely dark ($E \approx 1.0$ GPa) but have noticeable lighter grains ($E \approx 1.5$ GPa) and areas within the grains. Similarly, the Tol-200-100-narrow nanowires have visible fluctuations in E between grains and within each grain. Because differences in modulus of P3HT result from varied intermolecular interactions, these differences in modulus also correspond to local variations in the ΔH_f of the crystal. The fluctuations within the nanowire grains in Figures 2.14 E and F are seen more than just parallel to the scan direction of these images, which is horizontal. Because they occur along many different axes, we can conclude that the local fluctuations in ΔH_f are not solely from tip-surface interactions. Instead, they are local disruptions in short-range order, presumably as a result of defect inclusion into the crystal lattice. The largest fluctuations in E occur between crystal segments of the same nanowire, at the grain boundaries. These bridging layers are shown to be stiffer than the nanowire bulk in Figures S2.26-S2.28. The increased stiffness arises both because a reduction in thickness tends to increase modulus and because the grains incorporated defects to a point where crystal

growth was stymied, and only the crystalline bridging layer was able to grow.[105,106] So, the *E* of the grain is diminished by the defect incorporation, while the bridging layer retains a less-distorted and stiffer lattice. These observations on the impact of defects and crystallization on the short-range order and material properties of CP are reinforced by the UV-vis analysis of the imaged polymers, as shown in Figure 2.15. The calculated $A_{0\text{-}0}/A_{0\text{-}1}$ values were 0.75 for Tol-200-100-narrow, 0.74 for Br-275-98-narrow, and 0.66 for Br-150-91-wide. As short-range order increased, the optoelectronic properties are improved through increased planarity and orbital overlap. These results demonstrate that there is inclusion of defects into lattices and that this inclusion results in the noted differences in crystal growth and short-range order, confirming the results of Tables S2.1-S2.3. Interestingly, despite these differences and widely varied defect concentrations, each of these polymers was able to self-assemble into nanowires and maintain long-range order. This points to a preference of CP to sacrifice short-range order to maintain long-range and structural order.

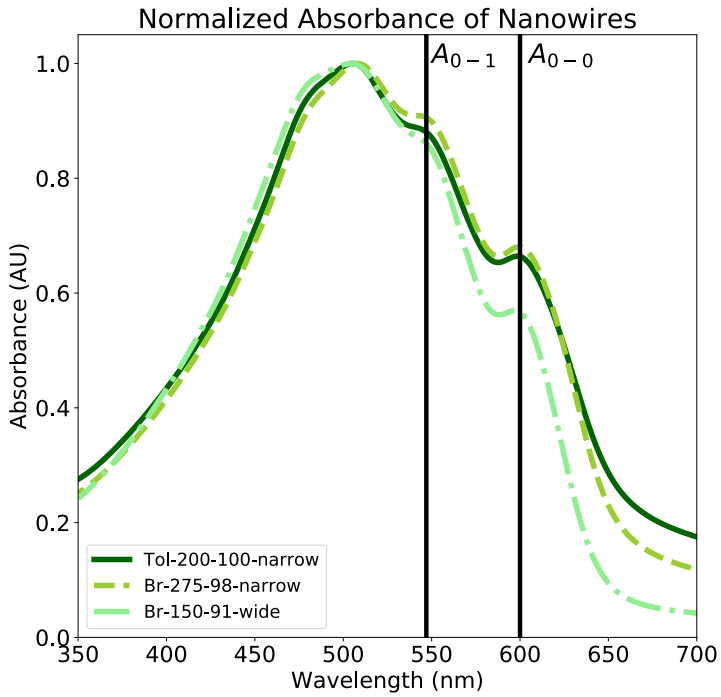

Figure 2.15. An overlay of the UV-vis absorption profiles for the nanowires shown in Figure 11. The absorption peaks corresponding to the 0-0 and 0-1 electronic transitions are marked for reference. An increase in the $A_{0\text{-}0}/A_{0\text{-}1}$ ratio signifies increased short-range order and electronic coherence along the backbone. As discussed, Br-150-91-wide had the most defects, least order and, correspondingly the lowest $A_{0\text{-}0}/A_{0\text{-}1}$ ratio. Conversely, Tol-200-100-narrow had the fewest overall defects and therefore has the highest $A_{0\text{-}0}/A_{0\text{-}1}$ ratio.[89]

2.5 CONCLUSIONS

It has been demonstrated that both regio-defects and end-groups can be partially incorporated into the crystal lattice of CPs and that this incorporation disrupts structural coherence and short-range order. Regio-defects can be included at concentrations as high as 10%, although this comes at the cost of decreasing both the charge mobility of the nanowires and ΔH_f of the crystallites. This may parallel the observation that CPs have been shown to have high paracrystallinity, even in films that are highly crystalline and well aligned.[57] In other words, regio-defects may affect the crystal lattice to the same degree as typical cumulative disorder, which is highly tolerated by the crystal lattice of CP. It has also been demonstrated that end-groups can be incorporated into the crystal lattice, although there is a strong preference to exclude them. Particularly in the case of Br, the steric bulk of the end-groups severely disrupts the crystal lattice. Importantly, our results reveal that end-groups can be selected to participate more easily in the crystal lattice. By choosing small end-groups, their incorporation can occur with a significantly reduced enthalpic penalty. Further, by selecting end-groups that can participate in π-π interactions, such as toluene, the lattice distortions resulting from the end-group incorporation can be mitigated and long-range order can be promoted. This underscores the importance of considering the identity of end-groups during the

design of a polymer for a given application, where morphology and crystallinity can directly affect device performance, such as with OFET and OPV.

Our results have also pointed to another route to mitigate the inclusion of end-groups, which is to 'tune' the DP of the polymer to be equal to an integer multiple of the observed l_c. By doing so, chain-folding ensures that the end-group will be located at the edge of the crystalline domain and thereby increase the crystallinity of the nanowire by as much as 20%. This observation is expected to be translatable to thin film active layers for optoelectronic devices, and is anticipated to prove particularly effective in devices that have their active layers deposited through techniques like blade-coating, which align polymer chains into highly crystalline and nano-structured thin films *via* sheer force, because of their structural similarity to nanowires.

2.6 SUPPORTING INFORMATION

Tables

Table S2.1. The results of analyzing nanowires made from commercial P3HT, aged for different times. Numbers in parenthesis indicate results from analyzing the unincorporated P3HT for that sample. Corresponding data is shown in Figures S2.1-S2.19.

Age (h)	%RR	[a]End-Group ratio	*Đ*	DP	$A_{0\text{-}0}$ / $A_{0\text{-}1}$	[b]ΔH_f (J/g)	[b] % Crystal	[c]l_c (nm)	l_c (units)	[d]$\xi_{(010)}$ (nm)	[e]Width (nm)	[e]Height (nm)
24	90 (86)	2.7 (4.5)	1.5 (2.0)	107 (54)	0.54	12.5	25.5	18.5	47	6	19 ± 0.6	5 ± 0.1
48	91 (86)	2.8 (4.6)	1.6 (2.2)	164 (44)	0.56	16.9	34.5	17.8	46	5.8	19 ± 0.6	5 ± 0.2
72	91 (85)	2.4 (4.5)	1.8 (2.6)	156 (35)	0.57	15.5	31.7	18.7	48	5.8	19 ± 0.3	5 ± 0.4

As purchased	90	4.7	1.8	186	n/a	15.5	31.6	17.2	44	n/a	n/a	n/a

[a]Ratio of Br-H:H-H chain termination. Determined by MALDI-TOF.

[b]Calculated from DSC. A value of $\Delta H_f^\infty = 49$ J/g is used in % crystallinity calculations.[37]

[c]Calculated using equation 1.

[d]Result of Scherrer analysis.

[e]Average of 100 nanowires, as measured by AFM.

Table S2.2. The results of analyzing nanowires made from P3HT of varying RR.[40]

Aged (h)	RR (%)	End-Group	$Đ$	DP	[a]$\xi_{(010)}$ (nm)	[b]Height (nm)	[b]Width (nm)	Width (units)	μ_h ($cm^2/V•s$)
72	93	Br-H	1.8	114	5	5 ± 1	24	63	n/a
72	93	Br-H	1.5	114	6.2	5 ± 1	24	63	$4.5x10^{-5}$
72	96	Br-H	1.1	108	11	5 ± 1	24	63	$1.0\ x10^{-4}$
72	97	Br-H	1.1	126	14	5 ± 1	24	63	$1.5\ x10^{-3}$
72	98	Br-H	1.2	96	21	4 ± 1	24	63	$1.1\ x10^{-3}$
72	99	Br-H	1.2	120	27	5 ± 1	24	63	$2.3\ x10^{-3}$

[a]Results of Scherrer analysis.

[b]Average of 100 nanowires, as measured by AFM.

Table S2.3. The results of analyzing nanowires made from P3HT of varying M_n. P3HT with integer multiples of l_c are above the bold line. P3HT with non-integer multiples are below the bold line. Results of XRD and DSC analysis are shown in Figures S20-S25.

Aged (h)	RR (%)	End-Groups	*Đ*	DP	[a] ΔH_f (J/g)	[a] % Crystal	[b] l_c (nm)	[b] l_c (units)	[c] $\xi_{(010)}$ (nm)
72	99	toluene -H	<1.3	150	35.5	72.4	26.3	67	6.7
72	99	toluene -H	<1.3	100	32.7	66.7	26.8	69	7.7
72	99	toluene -H	<1.3	50	30.8	62.9	20.5	52	9.8
72	99	toluene -H	<1.3	125	26.4	53.8	24.0	62	5.5
72	99	toluene -H	<1.3	75	25.4	51.9	26.1	67	4.1

[a]Calculated from DSC. A value of ΔH_f^∞ = 49 J/g is used in % crystallinity calculations.[37]
[b]Calculated using equation 1.
[c]Results of Scherrer analysis.

Figures

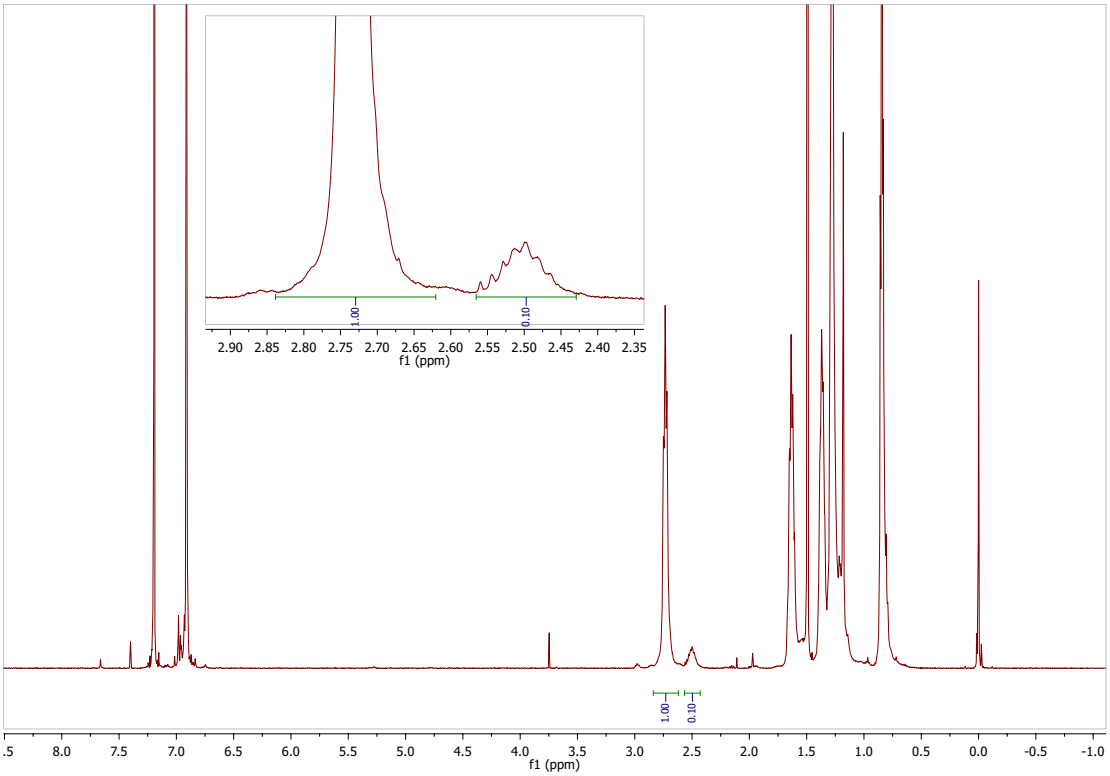

Figure S2.1. [1]H NMR of 24 h nanowire incorporated polymer.[89]

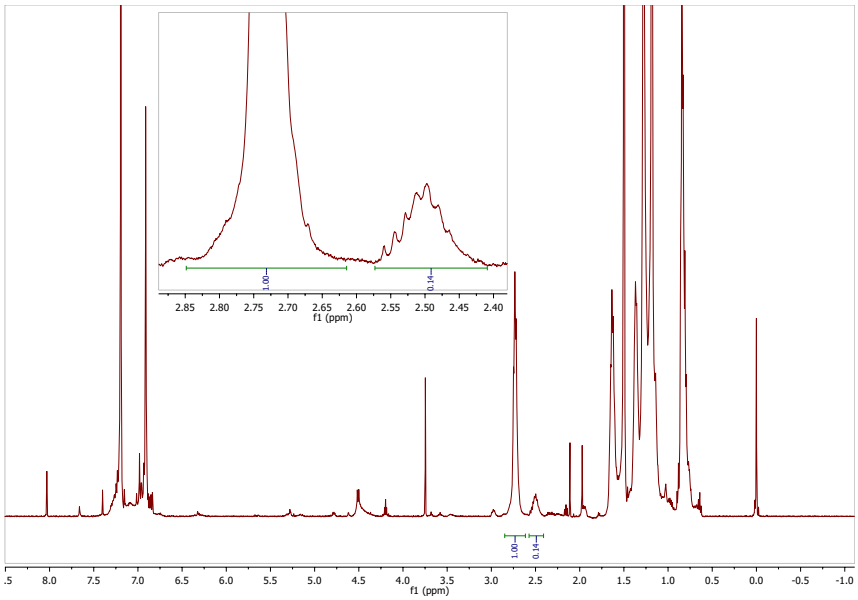

Figure S2.2. [1]H NMR of 24 h nanowire decanted polymer.[89]

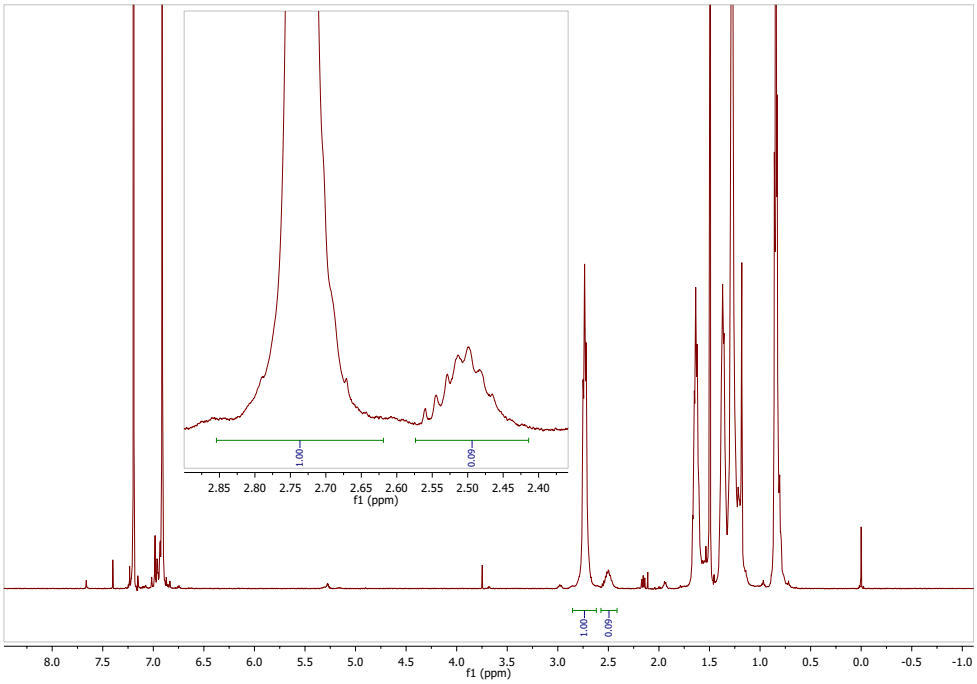

Figure S2.3. [1]H NMR of 48 h nanowire incorporated polymer.[89]

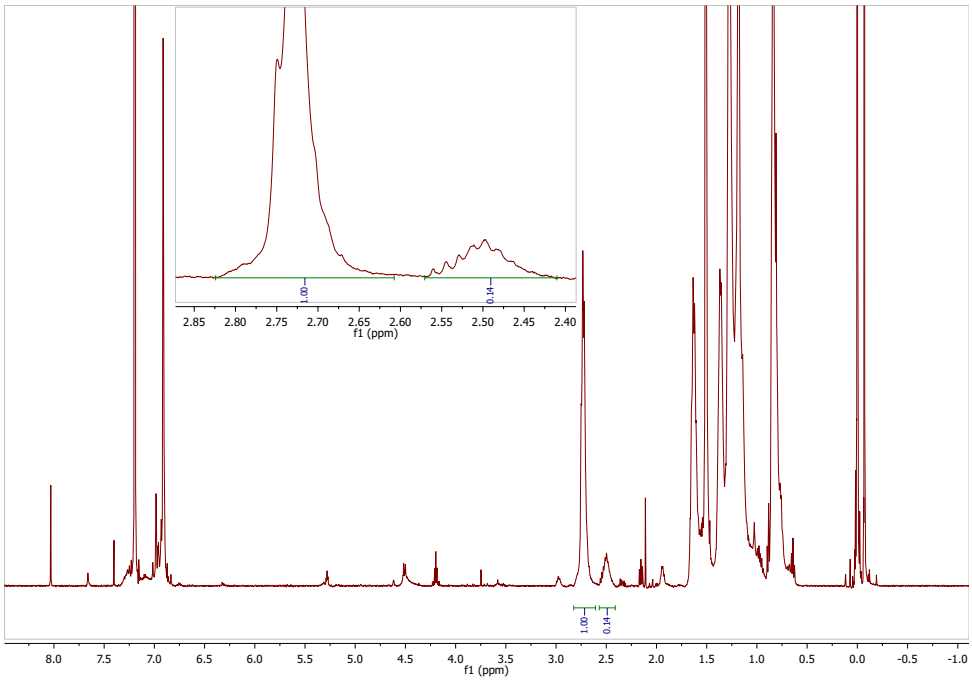

Figure S2.4. [1]H NMR of 48 h nanowire decanted polymer.[89]

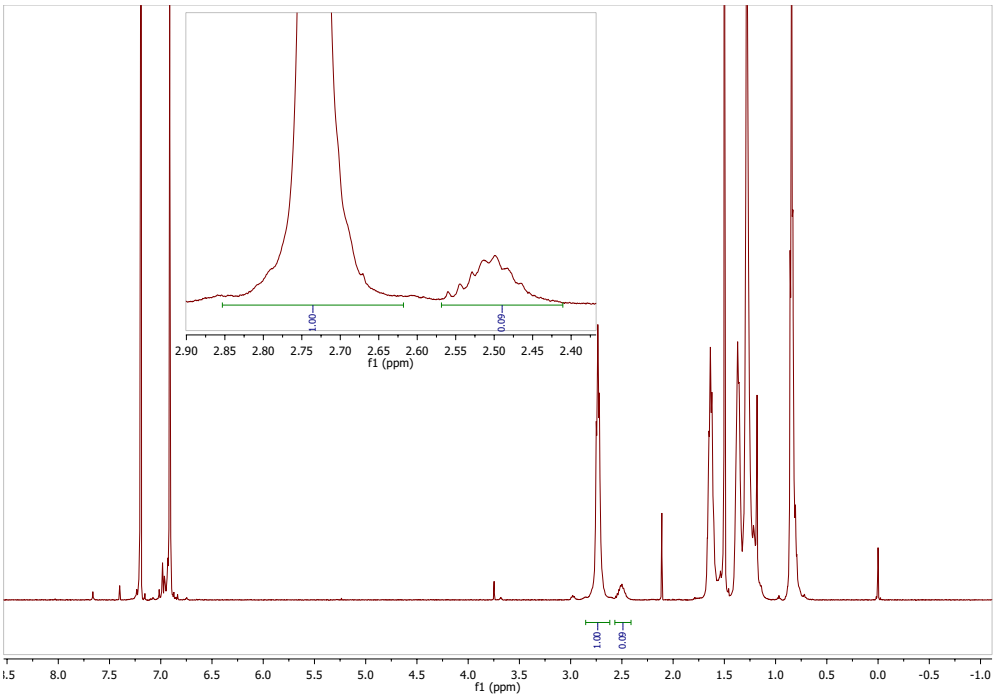

Figure S2.5. [1]H NMR of 72 h nanowire incorporated polymer.[89]

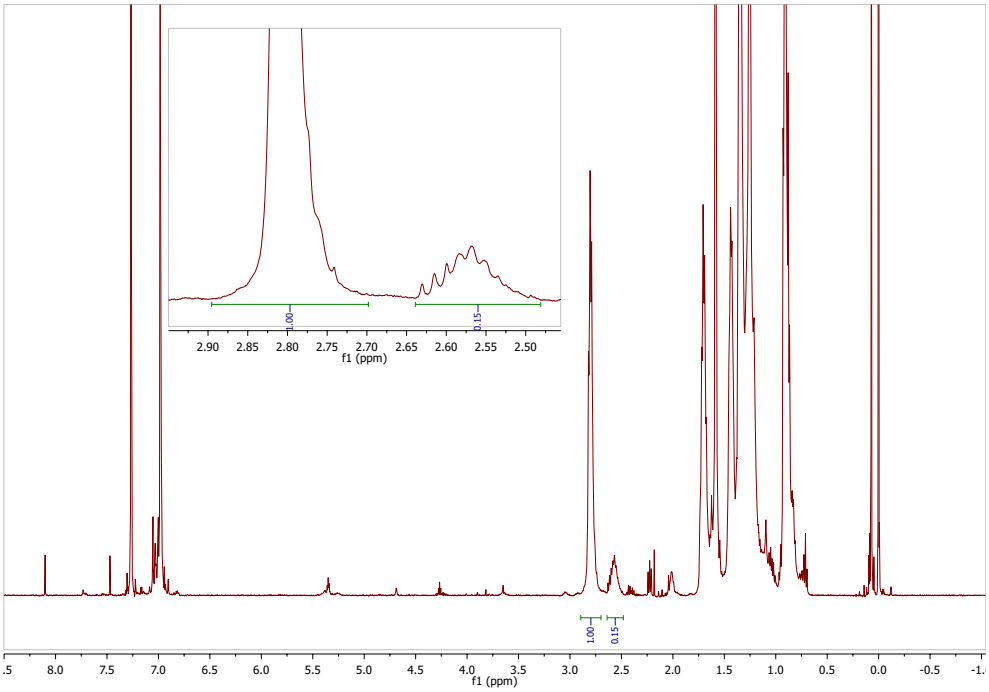

Figure S2.6. [1]H NMR of 72 h nanowire decanted polymer.[89]

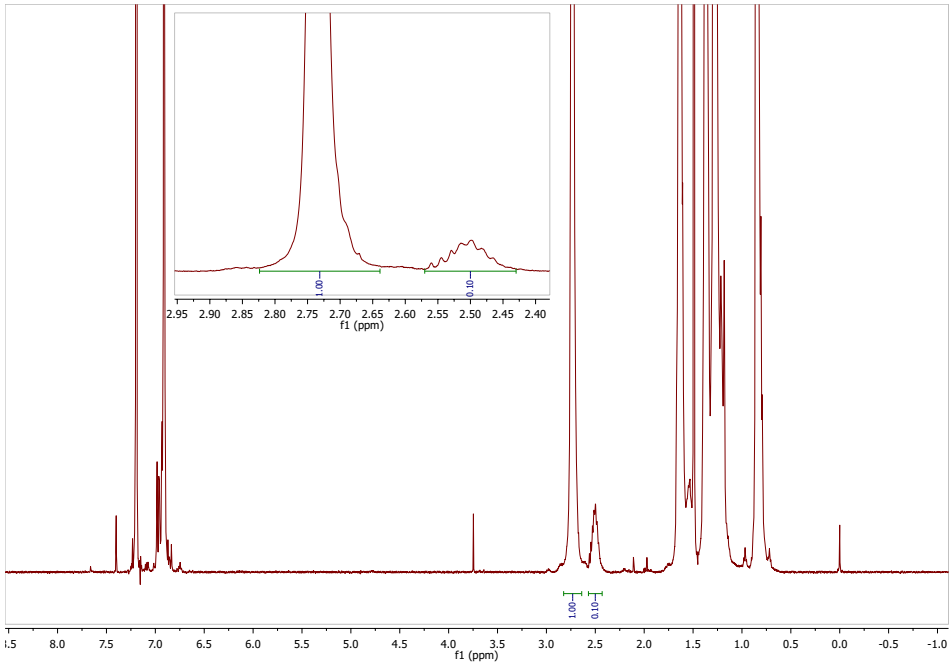

Figure S2.7. [1]H NMR of as-purchased commercial polymer.[89]

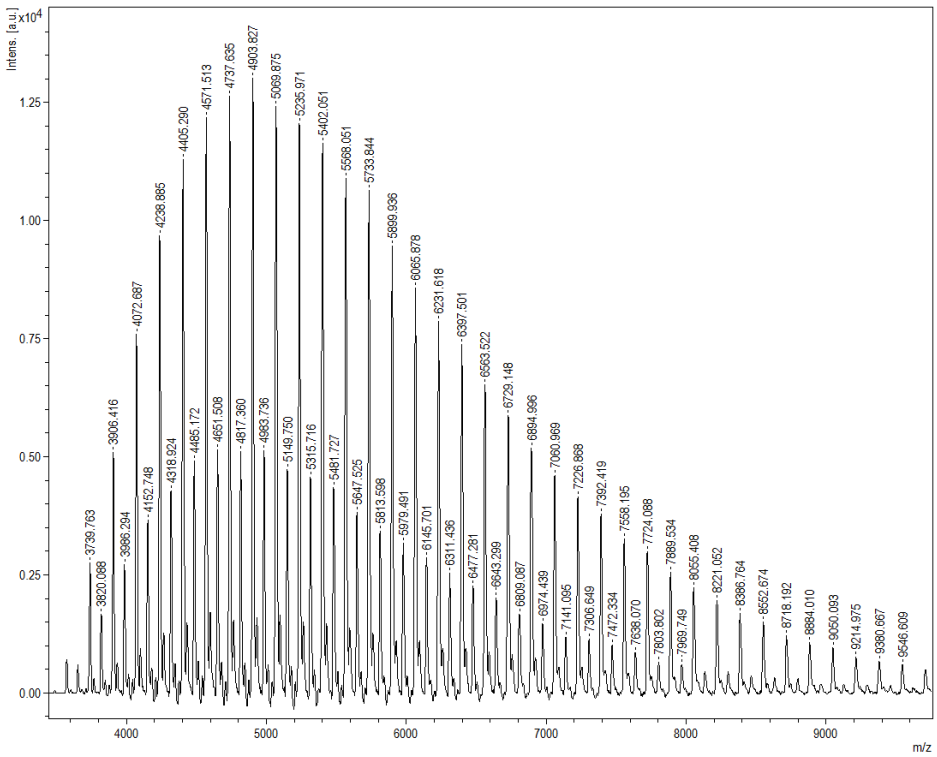

Figure S2.8. MALDI- TOF of 24 h nanowire incorporated polymer.[89]

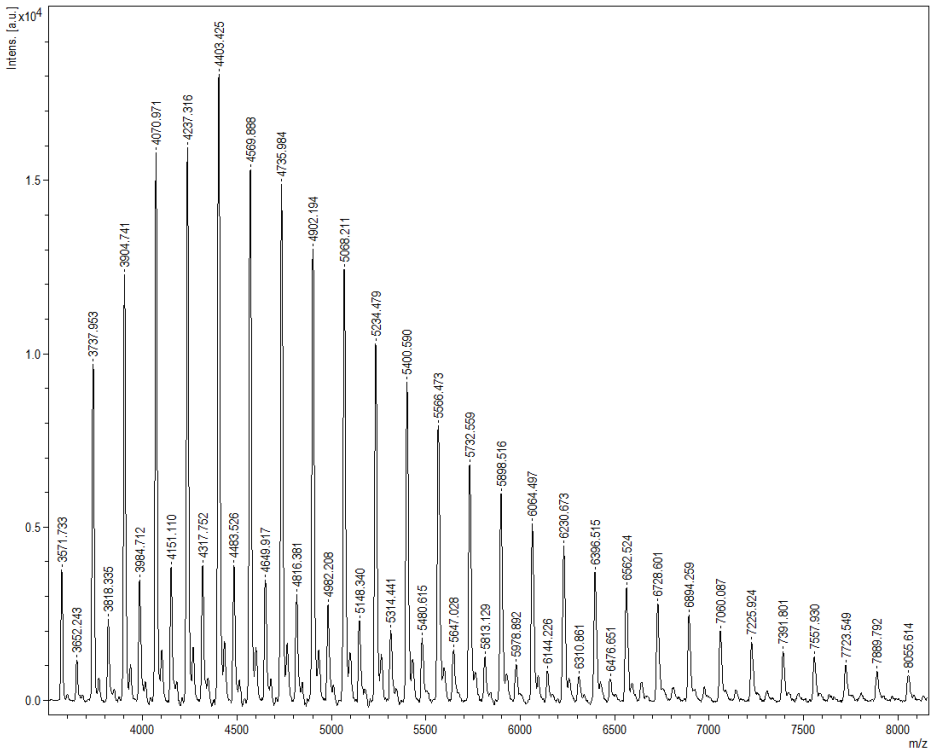

Figure S2.9. MALDI- TOF of 24 h nanowire decanted polymer.[89]

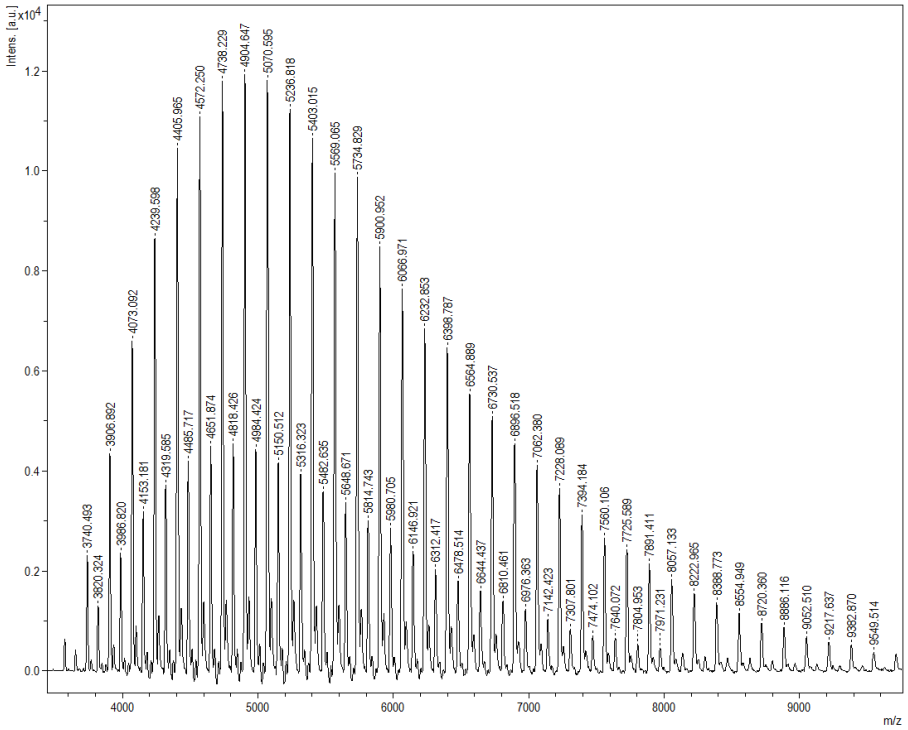

Figure S2.10. MALDI- TOF of 48 h nanowire incorporated polymer.[89]

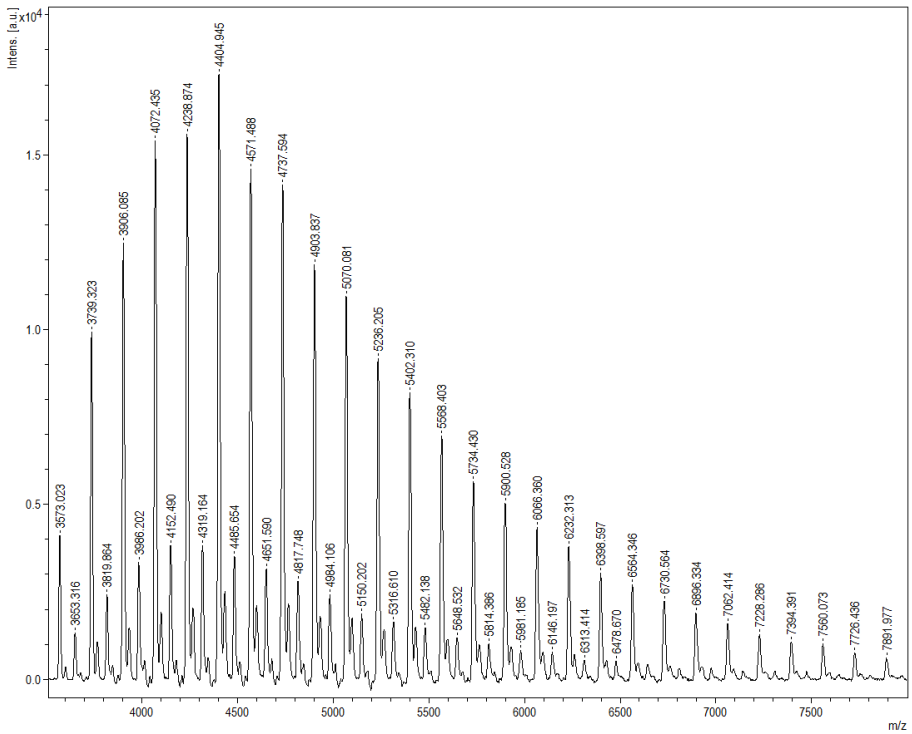

Figure S2.11. MALDI- TOF of 48 h nanowire decanted polymer.[89]

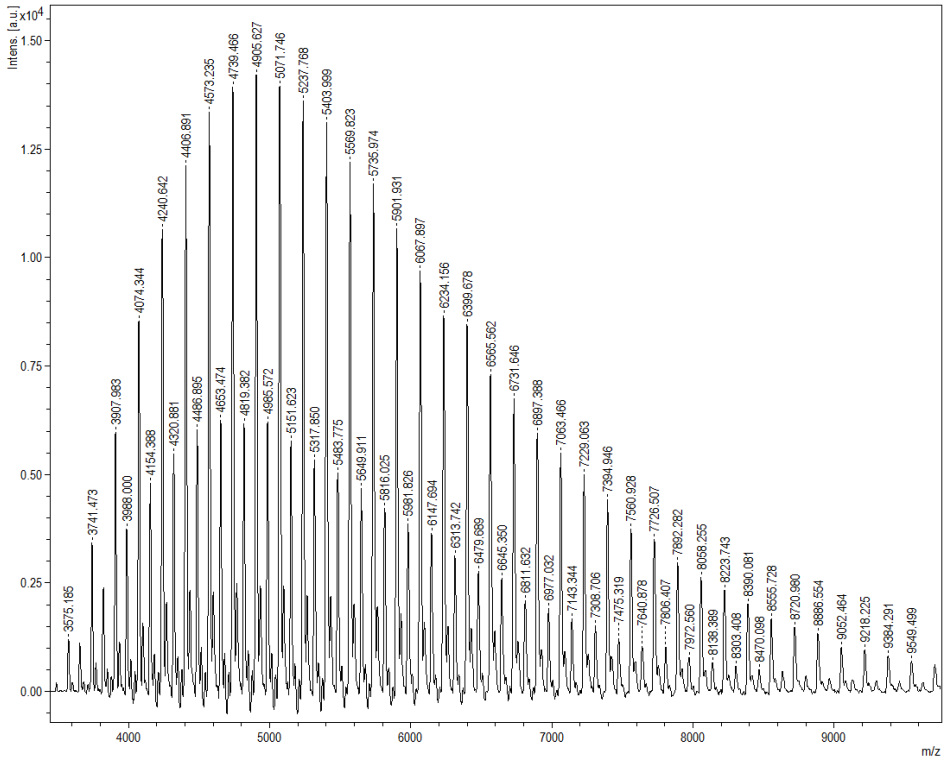

Figure S2.12. MALDI- TOF of 72 h nanowire incorporated polymer.[89]

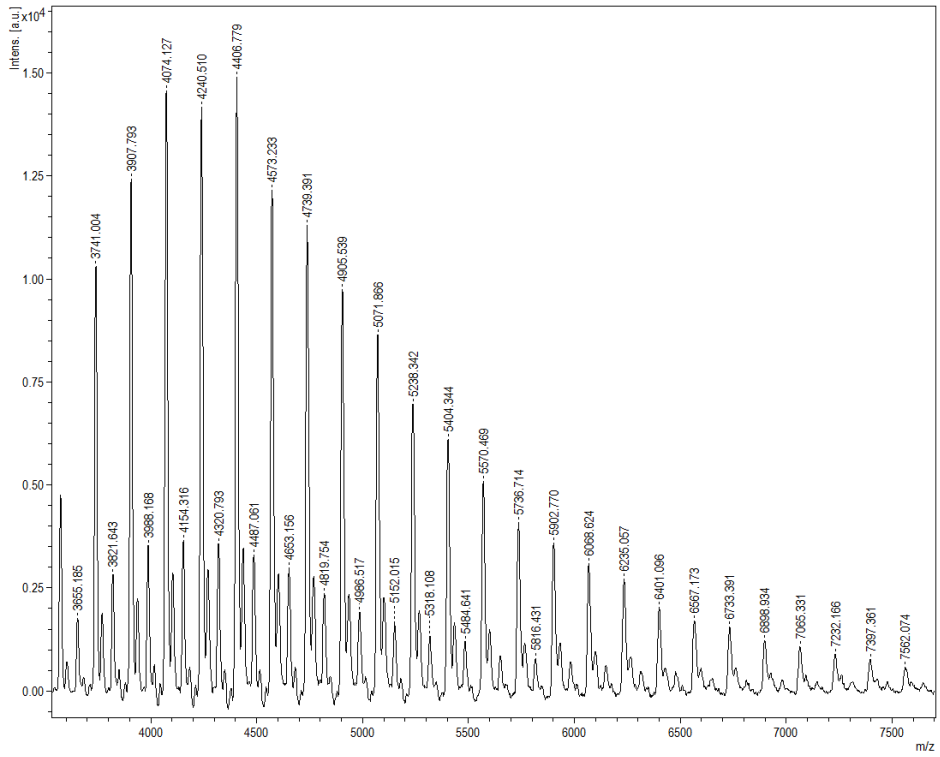

Figure S2.13. MALDI- TOF of 72 h nanowire decanted polymer.[89]

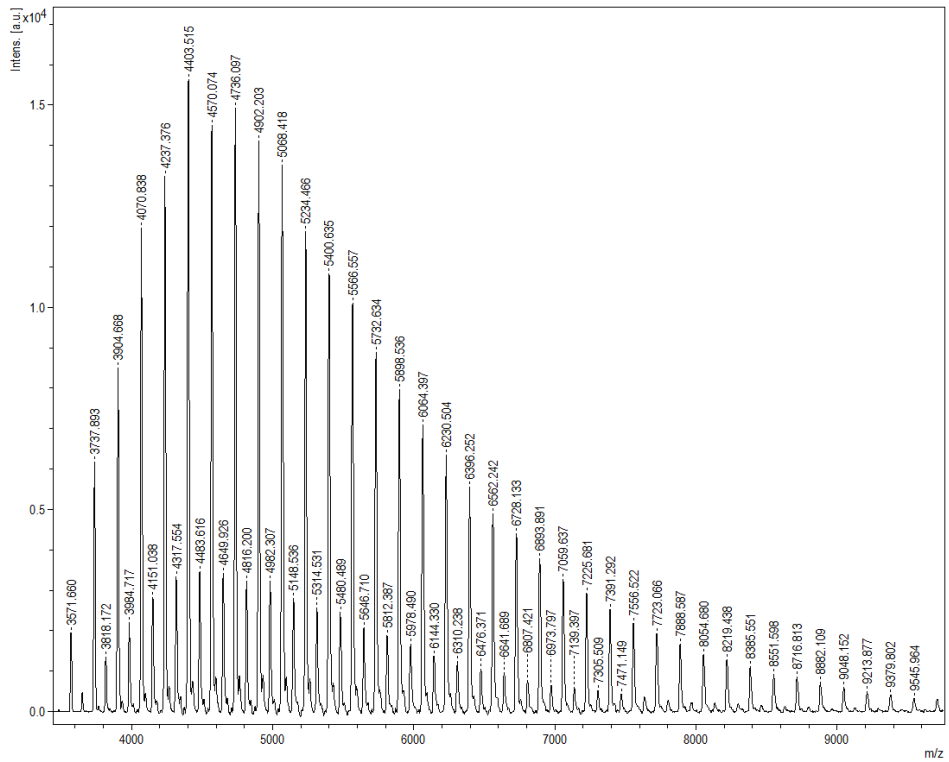

Figure S2.14. MALDI- TOF of as-purchased commercial polymer.[89]

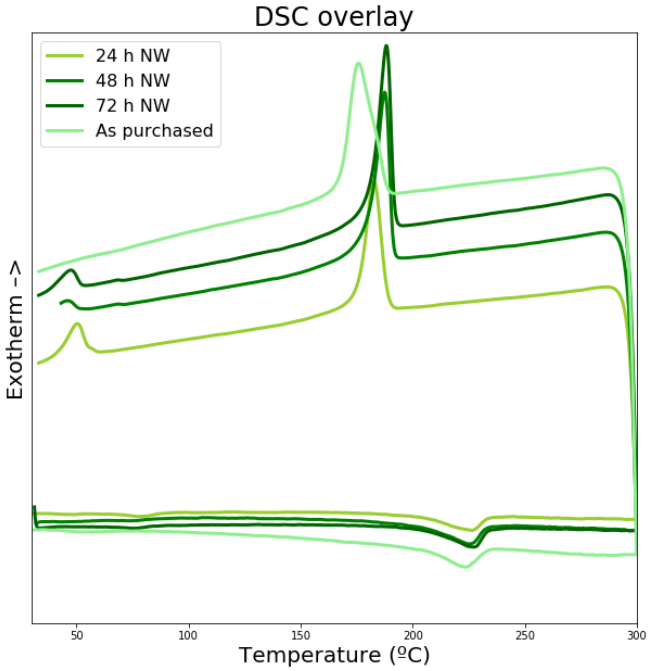

Figure S2.15. DSC overlay of commercial polymer nanowire aging series polymer.[89]

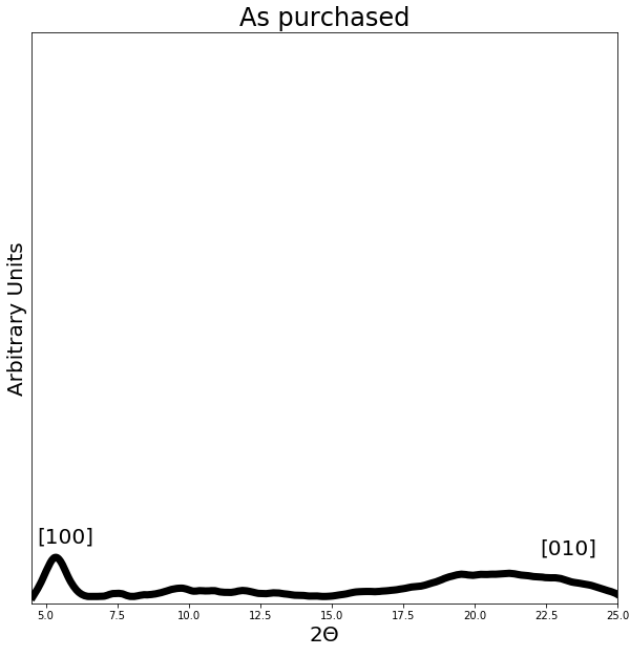

Figure S2.16. XRD spectra of the as purchased commercial P3HT.[89]

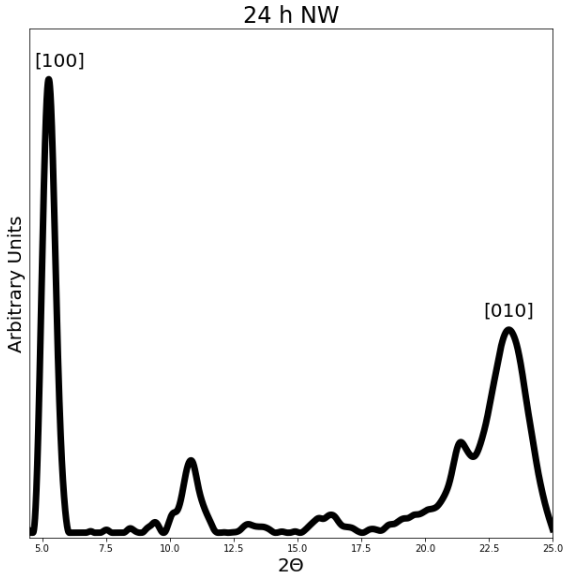

Figure S2.17. XRD spectra of 24 h aged commercial P3HT nanowires.[89]

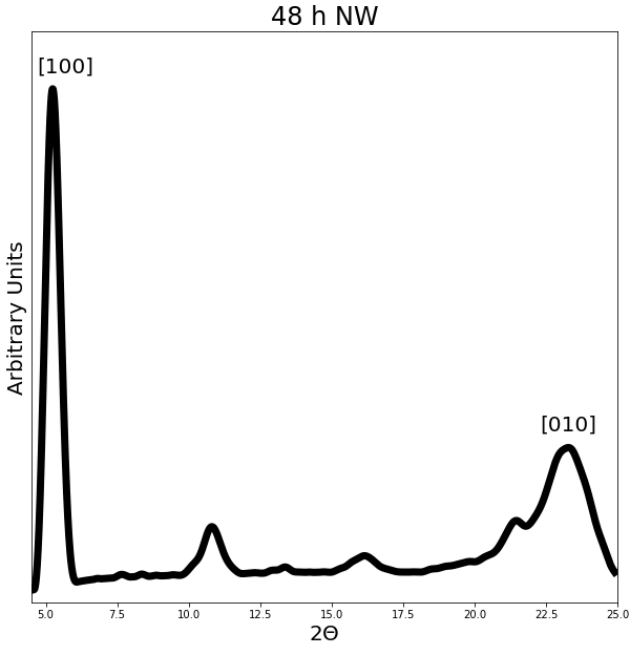

Figure S2.18. XRD spectra of the 48 h aged commercial polymer nanowires.[89]

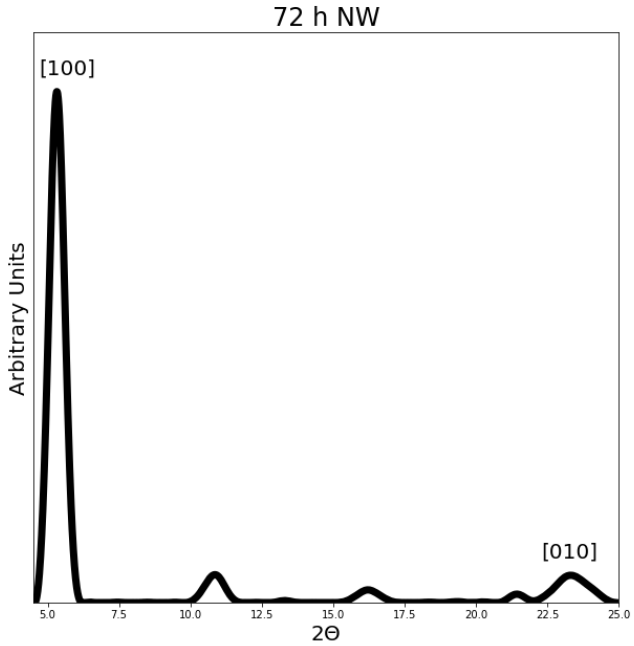

Figure S2.19. XRD spectra of the 72 h aged commercial polymer nanowires.[89]

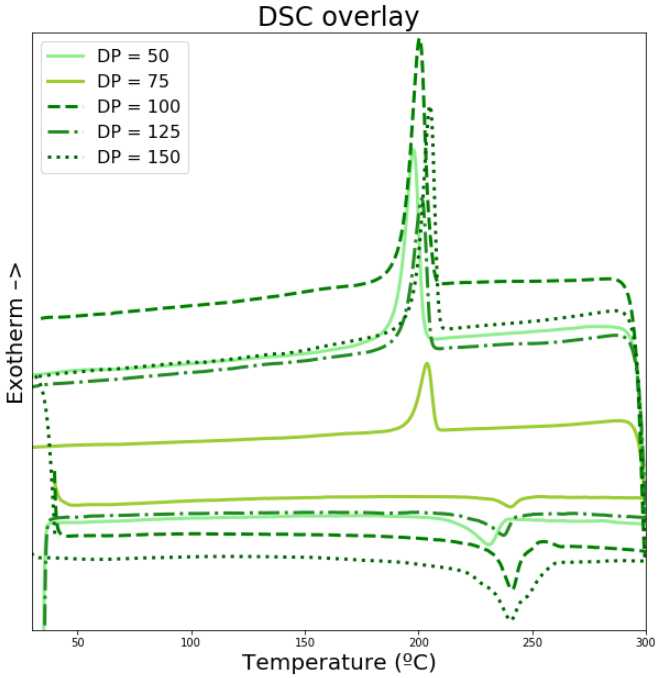

Figure S2.20. DSC overlay of synthesized polymer nanowires.[89]

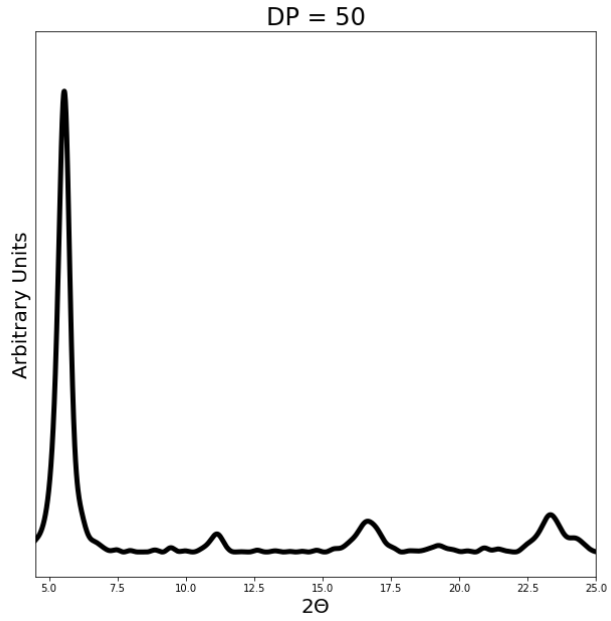

Figure S2.21. XRD of DP = 50 P3HT nanowires.[89]

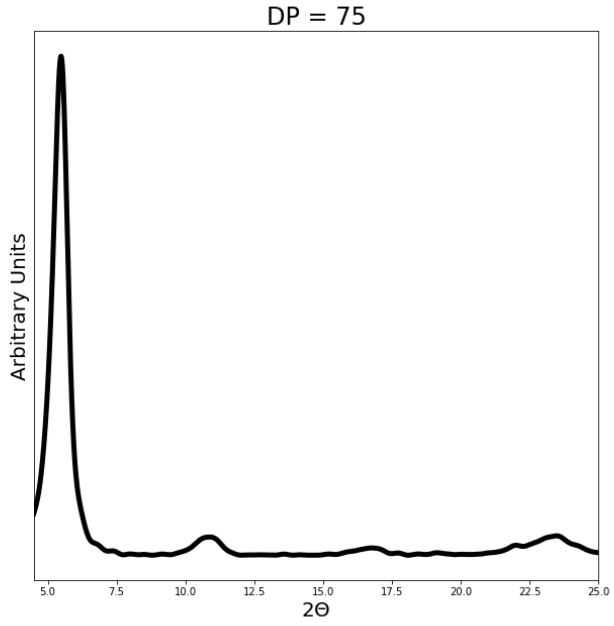

Figure S2.22. XRD of DP = 75 P3HT nanowires.[89]

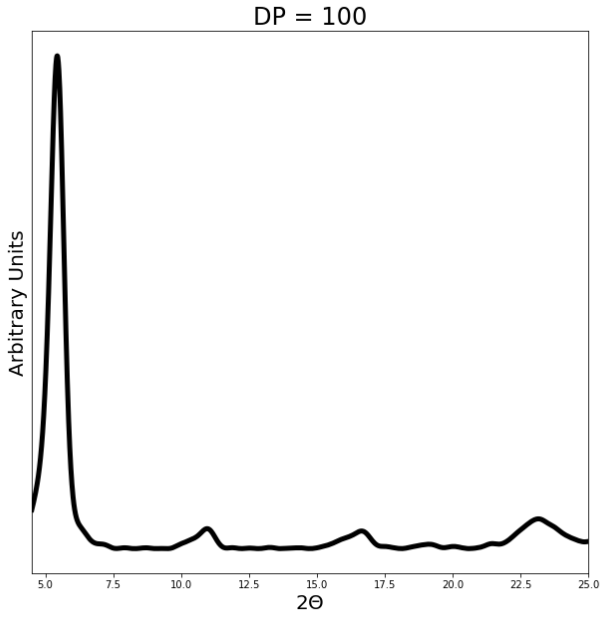

Figure S2.23. XRD of DP = 100 P3HT nanowires.[89]

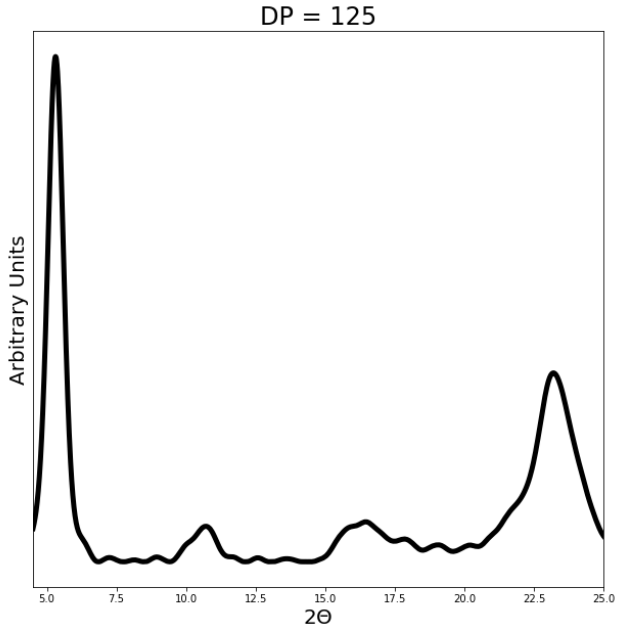

Figure S2.24. XRD of DP = 125 P3HT nanowires.[89]

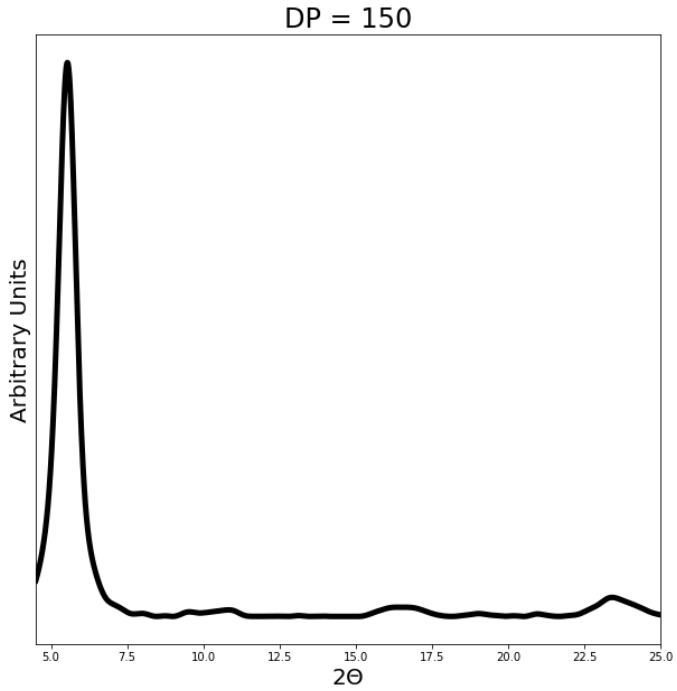

Figure S2.25. XRD of DP = 150 P3HT nanowires.[89]

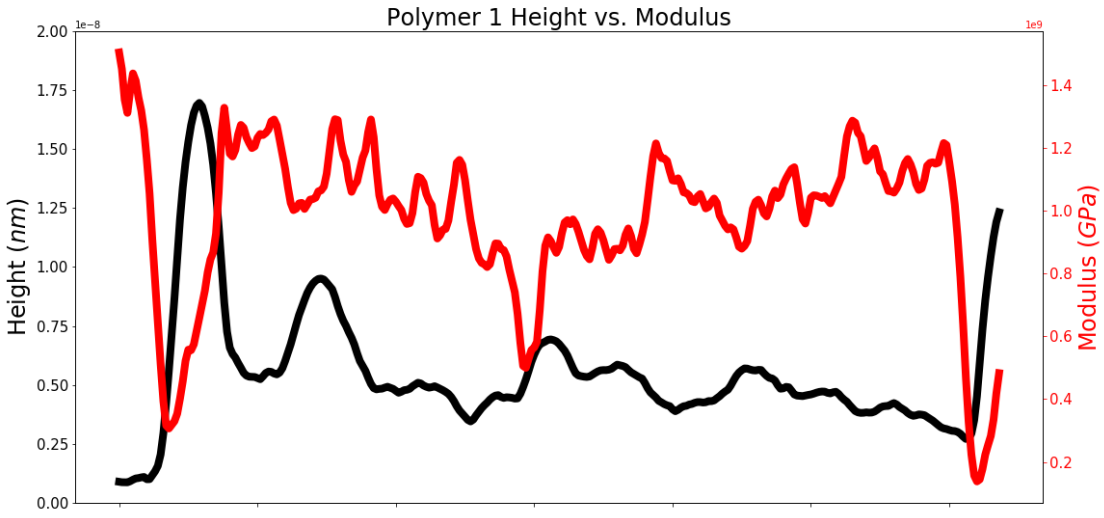

Figure S2.26. AMFM line-scans of Tol-200-100-narrow nanowire properties, along the [010] direction.[89]

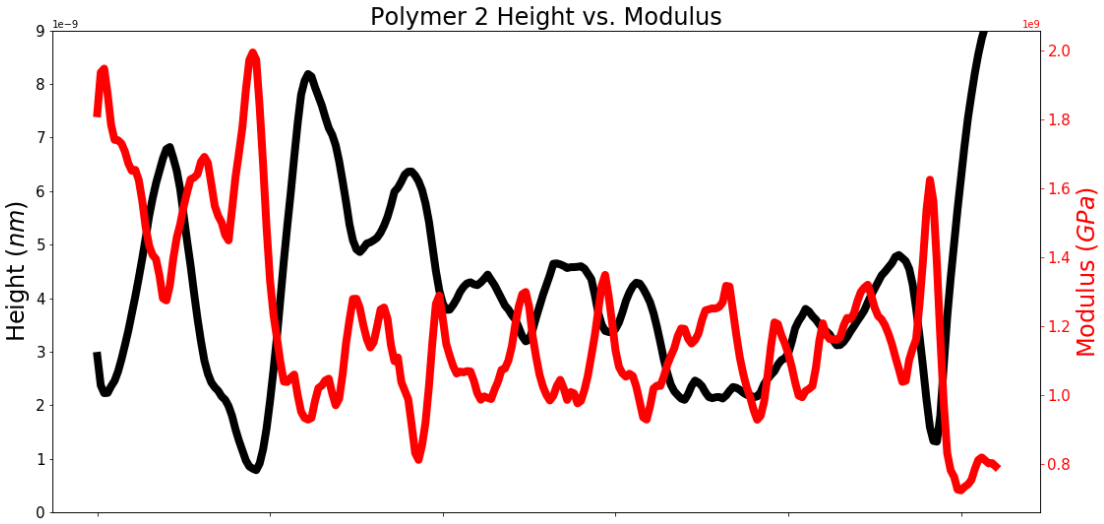

Figure S2.27. AMFM line-scans of Br-275-98-narrow nanowire properties, along the [010] direction.[89]

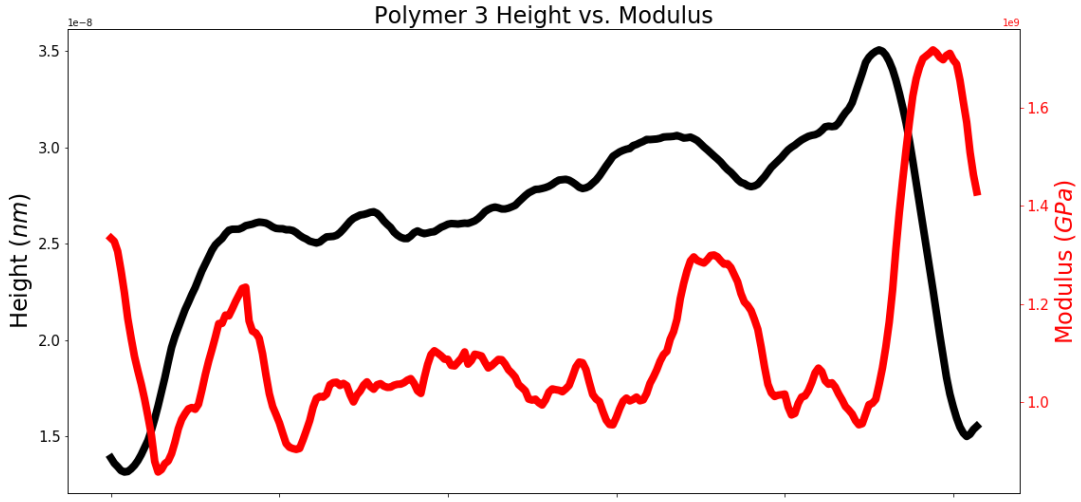

Figure S2.28. AMFM line-scans of Br-150-91-wide nanowire properties, along the [010] direction.[89]

Chapter 3. A GENERALIZABLE FRAMEWORK FOR ALGORITHMIC INTERPRETATION OF THIN FILM MORPHOLOGIES IN SCANNING PROBE IMAGES

*The work in this chapter has been previously published as an article: *ACS J. Chem. Inf. Model.* **2020** . DOI: 10.1021/acs.jcim.0c00308

3.1 INTRODUCTION

Thin-film and flexible electronic technologies, including devices such as photovoltaic cells, field effect transistors, and thermoelectric devices are enabled by materials such as π-conjugated polymers (CPs).[46,87,94,107–118] There are many promising candidate materials for active layer materials in these devices, which have highly tunable properties. All of these materials share a similar bottleneck: their device performance and stability are strongly dependent on their morphology at the micro- and nanometer- scale.[55,85,108,119–124] For any candidate material to achieve commercialization, it is necessary to predictably link parameters such as chemical structures, intermolecular interactions, processing conditions, and composition to final device performance, without the need to take an Edisonian approach to synthesis and optimization. The thin film morphology of a device active layer is a critical piece in this connection, so it is important to establish reproducible and quantitative descriptors of such morphology.

Devices made from thin-film electronic materials have greatly improved over the past decades, and CP-based devices have their electronic performance in some applications, such as organic electrochemical transistors (OECTs), conjugated polymers can outperform inorganic materials.[85,102,125] Due to the intrinsic connections between their device properties and their chemical structures, molecular weight, and intermolecular interactions, CP-based devices can be

exceedingly complex. Compounding this, CP morphologies often have dimensions that range from nanometers to micrometers. Such domains are difficult to interpret in single component films and become even more complex in blends of two or more components.[37,38,40,58,81,86,89] Though this frustrates the analysis of polymers, it also contributes to their tunability and responsivity and allows researchers to access specific performances, structures, and properties. This versatility also makes CPs well-suited for developing tools that quantify morphology.

Despite its importance, it has been difficult to quantitatively describe morphologies and nanometer-scale structure of thin films and interfaces. Imaging techniques, such as scanning probe microscopy (SPM), have been extensively developed and deployed to observe surfaces at this length scale for a wide variety of materials through the imaging of properties, such as conductivity or viscoelasticity, which are used in the present work.[102,126–129] The set of material properties that can be investigated by SPM techniques is rapidly expanding, and probe samples on length-scales ranging from Angstroms to millimeters.[103,130–133] These observations have enabled significant progress in understanding morphologies, but are traditionally constrained to qualitative or semi-quantitative sampling, as a result of the difficulty of hand-measuring features in microscopy images. Fortunately, the modularity and sensitivity of these instruments allow for a wide range of material properties to be simultaneously measured with topography. The resulting data have similarly formatted outputs, simplifying the comparison of different properties across a single scan.

There has been compelling research from various groups on utilizing computer vision and machine learning approaches to automatically identify features in micrographs and SPM measurements.[11,42-52] These approaches often use supervised models, which inherently restrict their application to materials or morphologies that are similar to the samples used in training the model.

Moreover, the performance of supervised models is connected to the number of samples in the training dataset. This limits their applications further, as it is first necessary to analyze and manually label a significant amount of data to build a large training set in order to improve the accuracy of these supervised learning approaches. In contrast, the data agnostic nature of unsupervised classification is particularly useful in building base models for the characterization of materials; such models can be easily extended to different materials, instruments, and techniques because they do not require training data.[145]

In this study, we present an open-source and adaptable Python toolkit, m2py, which is capable of interpreting and labeling morphological domains and features in images that have widely varied morphologies. Moreover, the m2py toolkit contains modular classes and functions that can be assembled into a customizable workflow to extract meaningful information from the domains and features in the SPM data. The m2py library simplifies the application of computer vision techniques; in particular, the workflow used herein enhances feature signals prior to applying a series of unsupervised methods. Once identified, m2py generates label maps of the identified features, so that they can be individually addressed and analyzed. These label maps can then be used to generate quantitative descriptions of the morphological information that has always been present in the SPM data. In this work, we have shown that domain size and major axis length are calculatable from m2py labels. Future work will also extract further morphological descriptions, such as aspect ratio, orientation, and perimeter length, so that the connection between such descriptors and device performance can be evaluated. In this work we demonstrate m2py's versatility in morphological classification by applying a generic m2py workflow to thin films of semicrystalline poly(3-hexylthiophene) (P3HT) in organic field-effect transistors (OFET) active layers, blended binary thin films of P3HT: phenyl-C_{61}-butyric acid methyl ester ($PC_{61}BM$) and

poly[[4,8-bis[(2-ethylhexyl)oxy]benzo[1,2-b:4,5-b']dithiophene-2,6-diyl][3-fluoro-2-[(2-ethylhexyl)carbonyl] thieno[3,4-b]thiophenediyl]] (PTB7):$PC_{71}BM$ in organic photovoltaic (OPV) active layers, and self-assembled nanostructures of P3HT spin-coated onto inorganic SiO_2 or ITO substrates. The m2py toolkit is compatible with any SPM technique, which we demonstrate by applying the same m2py workflow to measurements from force-distance mapping AFM (FDM), amplitude-modulated frequency-modulated bi-modal AFM (AMFM), and conductive AFM (C-AFM), three techniques that each have different degrees of spatial resolution and data dimensionality.

3.2 Materials and Methods

Unless indicated otherwise, all materials were purchased and used as-received from Sigma-Aldrich. P3HT was purchased from Rieke Metals or synthesized using previously reported methods;[75] PTB7 was purchased from Cal-OS; and $PC_{71}BM$ was purchased from Solenne BV. Si/SiO_2 and glass/ITO substrates were purchased from WRS.

3.2.1 *m2py Development*

All modules were written in Python. NumPy[146] was used for the preparation and manipulation of data. SciPy[147] was used for signal processing. Matplotlib[148] was used to create all plotting capabilities. scikit-learn[149] was used for dimensionality reduction and model training. Finally, scikit-image was used for semantic segmentation.[150]

3.2.2 *Substrate Preparation*

All substrates were cleaned by scrubbing with soap and DI water, followed by sonication in deionized water, acetone, and isopropyl alcohol for 15 min each. Following sonication, the

substrates were dried under a stream of air and subsequently plasma cleaned for 15 minutes using O_2 plasma.

For P3HT OFET and nanowire films, passivated substrates were used. To passivate the substrates, the substrates were taken directly from the plasma cleaner and placed under vacuum within a crystallization dish to allow the vapors from an open vial containing 400 μL of octadecyltrichlorosilane (OTS) to interact with the surface. The system remained under dynamic vacuum for 1 hour and was then switched to static vacuum. The system was heated at 125 °C for at least 3 hours to ensure evaporation of the OTS. After this, the heat was turned off and the system was allowed to rest under static vacuum over-night to allow the OTS vapor to self-assemble on the surface. Physisorbed and self-polymerized OTS was removed by rinsing with isopropyl alcohol, leaving behind only the self-assembled monolayer of OTS, onto which the P3HT and nanowire films were directly spin-coated.

PTB7:$PC_{71}BM$ and P3HT:$PC_{61}BM$ OPV films were spin-coated on top of ZnO hole-transport layers, following the canonical inverted architecture film stack.[114]

3.2.3 *Thin Film Sample Preparation*

The PTB7:$PC_{71}BM$ blends (1:1.5, total concentration 25 mg mL^{-1} in CB) and P3HT:$PC_{61}BM$ blends (1:0.95, total concentration 30 mg mL^{-1}) were stirred in chlorobenzene overnight at 70 °C prior to spin-coating. P3HT thin films were dissolved into chloroform at a concentration of 5 mg mL^{-1} and stirred at 50 °C overnight prior to spin-coating. Spin-coating was performed using the following spin-speed and durations, respectively: PTB7:$PC_{71}BM$ (1000 rpm, 2 min), P3HT:$PC_{61}BM$ (1000 rpm, 60 sec), and P3HT (2500 rpm, 60 sec). Solution preparation and spin-coating were all carried out in a nitrogen glovebox.

The P3HT:$PC_{61}BM$ and P3HT thin films were annealed at 175 °C for 30 min and 150 °C for 50 min, respectively. PTB7:$PC_{71}BM$ films were used as-cast.

3.2.4 *Nanowire Film Preparation*

For the nanowire solution, P3HT was added to anhydrous anisole at a concentration of 2 mg mL^{-1} under a nitrogen atmosphere in a glovebox. In order to ensure complete dissolution, the solution was heated and stirred at 110 °C for 24 h, after which the heating and stirring was stopped and self-assembly was allowed to progress for 72 h. The resulting nanowire suspension was spin-coated directly onto the passivated substrates.

3.2.5 *Force-Distance Mapping Atomic Force Microscopy (FDM)*

AFM micrographs were obtained on a Bruker ICON AFM in Peak- force Quantitative Nanomechanical Mapping mode. ScanAsyst-Air tips were used for these measurements (SiN/Al, ~70kHz, and 0.4 N m^{-1}).

3.2.6 *AMFM*

AMFM measurements were performed on an Asylum Research Cypher-ES system. For AM-FM Viscoelastic mapping, we used built-in routines provided by Asylum Research and μMasch tips (HQ:NSC18/Pt, 75 kHz, and 2.8 N m^{-1}). All measurements were performed in a nitrogen environment.

3.2.7 *Conductive Atomic Force Microscopy (C-AFM)*

C-AFM measurements were performed on an Asylum Research Cypher-ES system. For conductivity mapping, we used built- in routines provided by Asylum Research and μMasch tips (HQ:CSC38/Cr-Au, 10 kHz, and 0.03 N m^{-1}). A bias of -2 V was applied between the tip and the

substrate, which was grounded through the sample holder using silver paint. All measurements were performed in a nitrogen environment.

3.3 Results and Discussion

SPM data is structured as a stack of 2-dimensional matrices with each layer in the stack (commonly referred to as a channel), representing a different aspect of the material's response.[151,152] The methodology primarily used in this investigation, FDM, has six channels of signals: adhesion, deformation, dissipation, modulus, height, and stiffness. By comparing the values from each channel for each pixel, pixels can be sorted, filtered, or clustered by their similarity. A summary of the m2py workflow is shown in Figure 3.1.

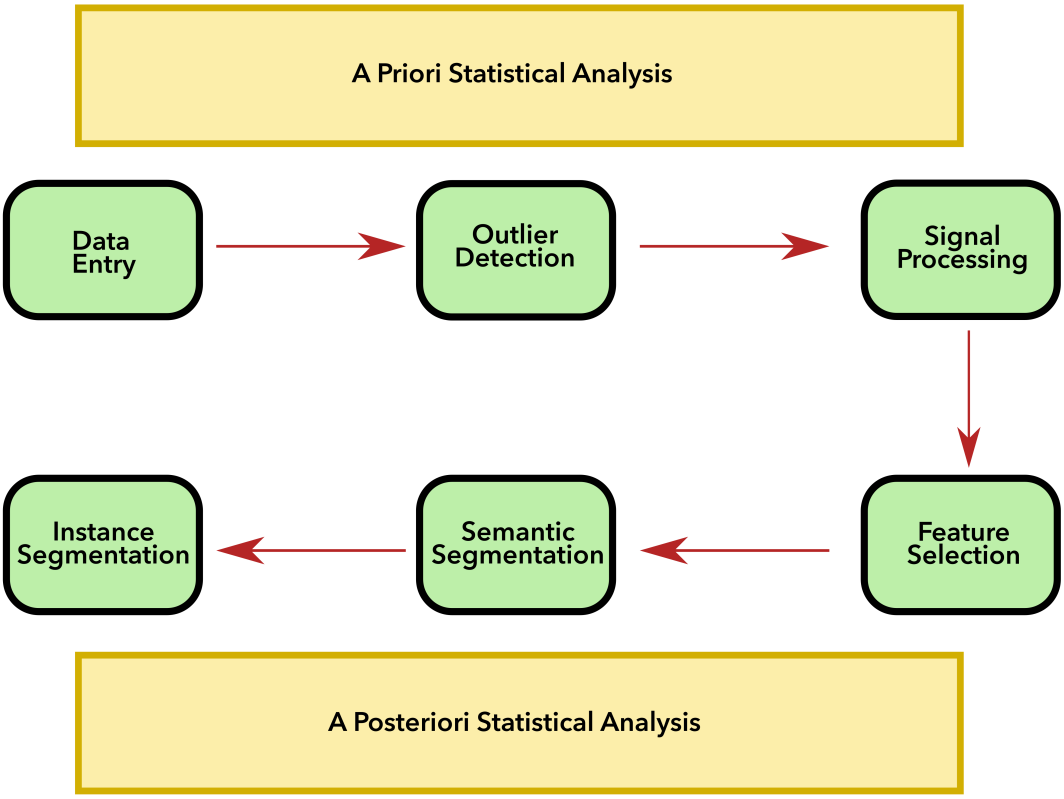

Figure 3.1. A generalized m2py workflow. Raw or pre-cleaned data is fed in by the user. Next, outlier removal and fast Fourier transforms are applied to increase the sensitivity of m2py's segmentation modules. Feature selection finds the most descriptive features from the data while reducing data dimensionality to distill the material-property signals. This is followed by semantic segmentation (pixel classification) and then instance segmentation (pixel clustering). Statistical information can be extracted at any point in the workflow.[153]

3.3.1 *Data Intake and Pre-Processing*

The SPM community has developed robust toolkits for viewing SPM data and converting between file formats. Packages such as Gwyddion can parse instrument specific and open-source file formats and perform automated routines that handle SPM data in a tensor fashion. However, these tools primarily accelerate data processing and improve interpretation of the image by the microscopist.[151,152,154] They do not seek to identify and label segmented domains for algorithmic analysis, nor do they enable any automation of the identification. By relying on these familiar tools for data cleaning and translation into NumPy-readable file types, m2py is able to process data from virtually any source.

Once the SPM data is converted to a NumPy format, the material-property signals need to be enhanced. Outlier detection and image denoising are essential at improving the signal to noise ratio of the raw SPM data. These outliers need to be removed early, as they can overpower material-property signals during later clustering methods. Examples of outliers includes pixels associated with surface aggregates, pin-holes, or tip-scars. The m2py method pre_processing.extract_outliers() recognizes these pixels and generates a Boolean matrix of outlier labels so that the corresponding pixels are ignored by the subsequent classification models, improving their results. This method has adjustable windows and thresholds and is typically

applied to the height channel. The output of outlier detection is illustrated in Figure S3.1. For further noise reduction, the method pre_processing.frequency_removal() applies image compression via fast Fourier transform to each layer using an adjustable band-pass filter to remove noise signals at high or low frequencies.[147] An example of this method being used to remove low-frequency background noise is shown in Figure S3.2. Additionally, the Fourier-space signal data can be accessed and used to analyze the orientation, alignment, and signals within images.[52]

3.3.2 *Feature Selection and Semantic Segmentation*

Following outlier removal and signal processing, pixels are analyzed and classified into a user-specified number of phases using a combination of Principal Component Analysis (PCA) and the Gaussian Mixture Model (GMM). PCA serves as the feature selector combining all data channels into fewer but more informative features, while retaining most of the information / variance of the system.[134,149] Even though the generated principal components are linear combinations of the input channels, they represent a complex vector-space relationship to the original data. Through the retention of only the most informative features, PCA speeds up the computationally expensive process of classification by minimizing the number of channels to examine. So, incorporating PCA into the m2py workflow is often beneficial to further enhance materials response signals prior to classification.[134,155] An example of PCA selection of material response information for FDM measurement of an annealed P3HT:$PC_{61}BM$ thin film is shown in Figure 3.2. Once PCA has been applied, the principal components can also be accessed and analyzed through the SegmenterGMM() class. A principal component of the OPV film from Figures 3.2a and b is shown in Figure 3.2c and an example of cross-correlation of those principal components is plotted in Figure 3.2d. In Figures 3.2b, c, and d, the red and blue colors indicate the final GMM phase

classification of each pixel. Even though the number of channels is reduced by half in this example, the cross-correlation in Figure 3.2d confirm that the principle components retain the signal clusters visible in the input channel cross-correlations of Figure 3.2b.

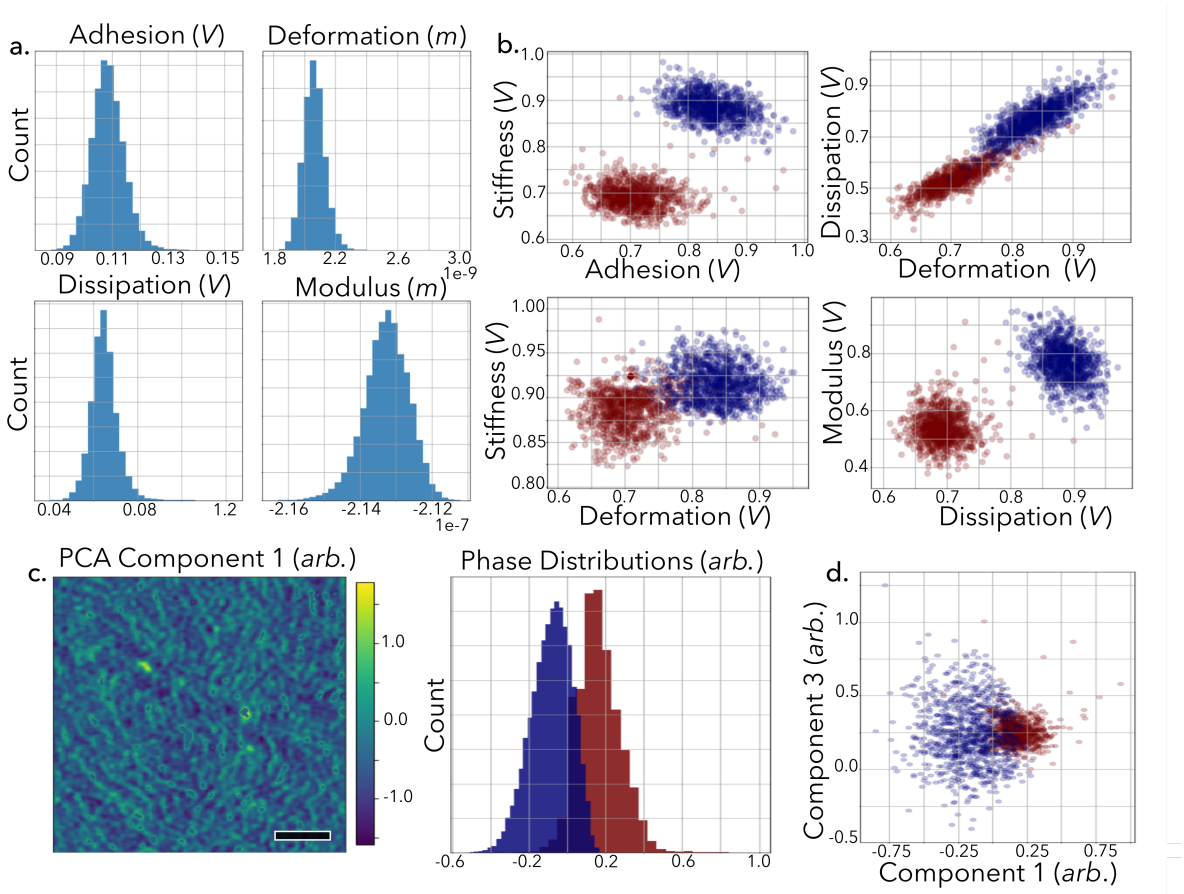

Figure 3.2. Signal distributions and cross-correlations are easily extracted throughout the workflow. **a.** Four input material-property distributions from an annealed P3HT:$PC_{61}BM$ thin film. Input channel units are relative. **b.** Cross-correlations from the same sample after GMM segmentation, with red and blue representing the two GMM labeled phases. **c.** (*left*) An example principal component from PCA of the same sample. Principle component units are arbitrary. (*right*) The property distributions for each of the two GMM phase for the principal component. **d.** Cross-correlation between principal component 1 and 3, color-coded by their GMM phase labeling. Scale bar is 200 nm, images are 256 × 256 pixels.[153]

Once the material response signals have been selected by applying PCA, GMM is used as a semantic segmenter to classify pixels by their clustered material response signals. Afterwards, m2py assigns each pixel a phase label corresponding to its GMM classification. The number of phases is easily tuned by a user; for instance, if a user is expecting a binary blend to have two phase-pure regions, and one blended region, the GMM can be made to deconvolute the SPM data into three distinct phases. A more detailed discussion of the GMM implementation is presented in the Supporting Information on page S8.

PCA and GMM are combined and implemented through the SegmenterGMM() class. Which features are used to segment and classify individual pixels has a significant impact on the overall performance. To clarify both the use of the SegmenterGMM() class and the impact of user choices on overall classification, several examples are presented below.

One common consideration is whether or not the height channel should be included during GMM phase label assignment. Depending on the magnitude of the differences in the material-response signals that the GMM segmenter uses to classify the pixels, height information can be either advantageous or disruptive when included. Omission of height data tends to be useful if the topographical features are not reflective of the underlying morphological domains, and thereby misrepresent the true morphology of the film, or when the material-response signals show only small fluctuations. This is the case with P3HT thin films, where surface features are often dictated by drying kinetics and surface-air interactions, rather than phase separation into crystalline and amorphous domains.[156–158] This is demonstrated in Figure 3.3, where the modulus and adhesion channels show small domains (Figure 3.3a.), as expected of P3HT skin-layers.[159] When height information is included, GMM results show large domains (Figure 3.3b) that do not reflect the small, isotropic domains that are seen in the five material-property channels. Exclusion of the

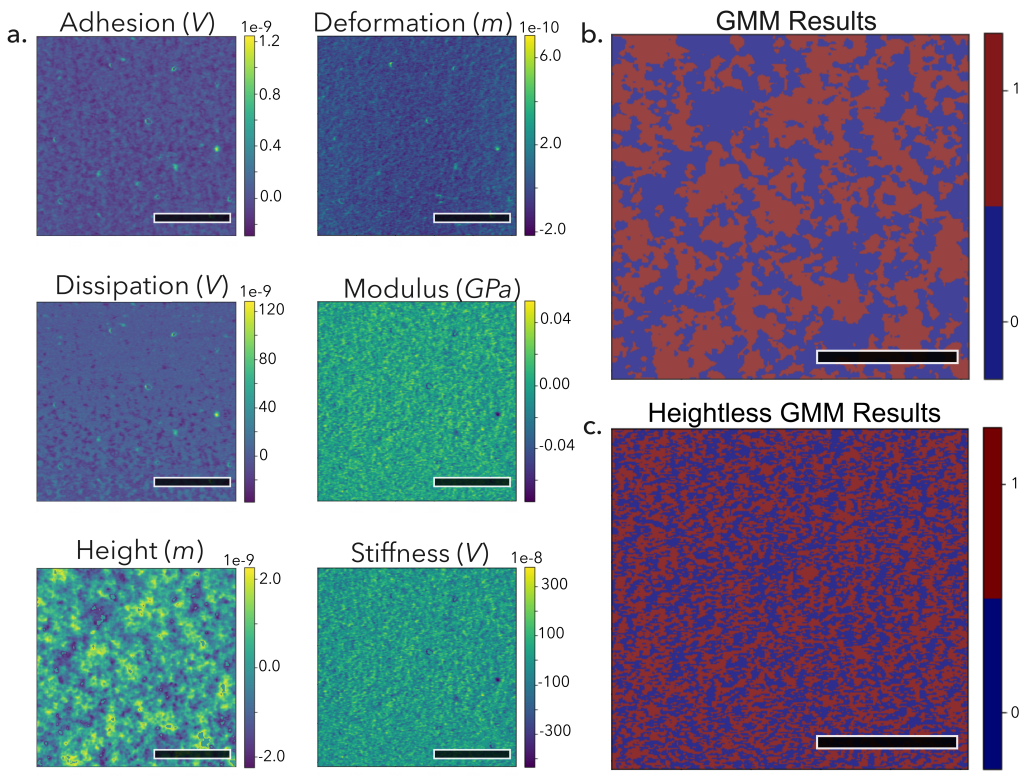

Figure 3.3. Input data and the GMM label maps from FDM measurements of a P3HT OFET active layer. **a.** The input data channels after outlier and noise removal. Colorbar units are relative. **b.** GMM labeling when the height channel is included. **c.** GMM labeling when the height channel is excluded. All scale bars are 500 nm, imaged at 512 × 512 pixels.[153]

height channel is accomplished with the 'heightless' flag during the SegmenterGMM() class instantiation, and the corresponding results of this heightless classification, Figure 3.3c, are far more representative of the morphological domains visible in Figure 3.3a.

In cases where differences in material properties are significantly large, such as with PTB7:$PC_{71}BM$ binary blends (Figure 3.4), the topographical features can actually improve GMM interpretation by correcting edge-induced tip-surface interactions. Figure 3.4b and c show this improvement in GMM labeling of a PTB7:$PC_{71}BM$ thin film with and without height, respectively.

The spherical domains seen in the height channel of Figure 3.4a appear symmetric, despite being scanned left-to-right. This is not the case in the stiffness channel, where the left edges of the aggregates appear far softer than the right edges. This is caused by the probe-scanning direction–significant changes in sample thickness change the amount of the tip surface-area contacting the surface and artificially increases or reduces the measured adhesive forces as a result of the measurement's dependence on the probe tip's contact-radius.[160] This effect is graphically explained in Figure 3.4d.

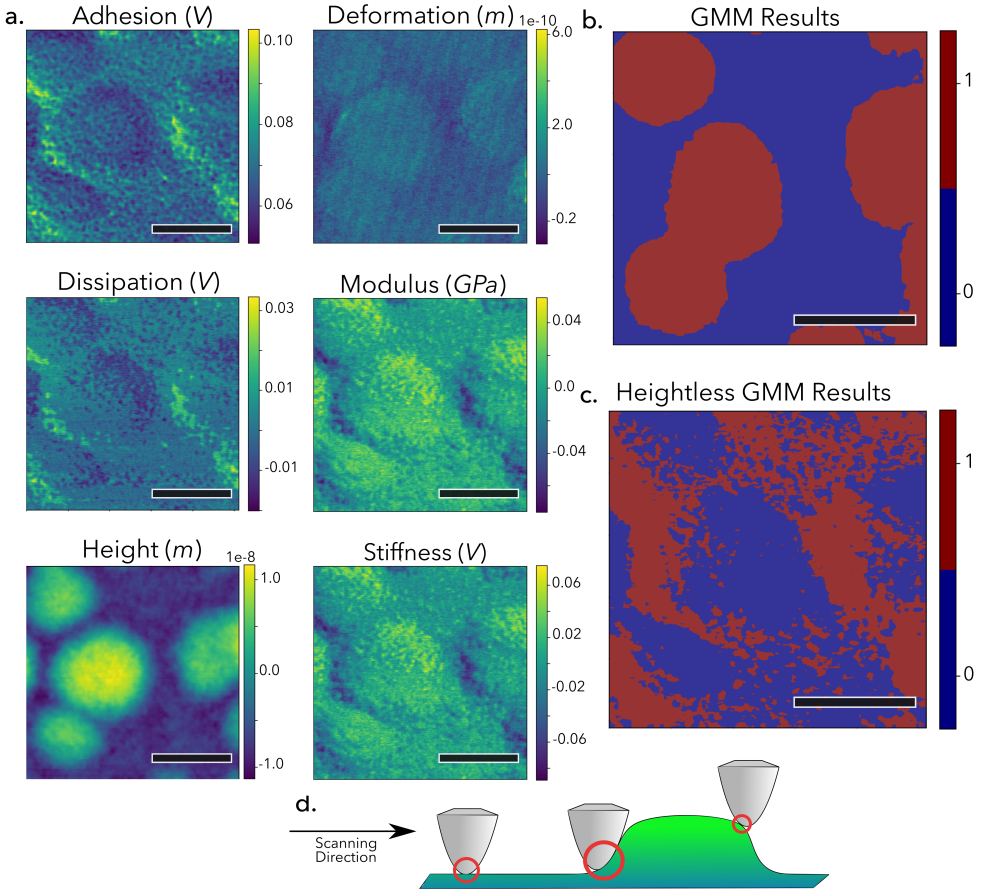

Figure 3.4. Input data and GMM label maps from FDM measurements of a PTB7:$PC_{71}BM$ thin film OPV active layer. **a.** The input data channels after outlier and noise removal. Colorbar units are relative. **b.** GMM labels when the height channel is included. **c.** GMM

labels when the height channel is excluded. **d.** Graphical explanation of how large features can artificially alter measured material response signals by varying the amount of surface-area contact between the probe-tip and sample surface. The scale bars are 200 nm, images are 256 × 256 pixels.[153]

Therefore, in this example, excluding the height channel from classification eliminates edge-induced distortions from the GMM labels. Analogous effects follow for other SPM techniques, where inclusion of topography data can see similar improvements. Judicious selection of which channels to use or remove can make a significant improvement in the quality of data produced through m2py.

Thus far, we have examined isotropic domains, but CP often exhibit highly anisotropic morphologies; nevertheless, the efficacy of GMM classification is not dependent on the size or shape of domains. This is because GMM classification depends on materials property signals, rather than strictly edge detection, as most supervised techniques do. An exploration of the use of m2py's GMM tool in classifying anisotropic morphologies is visible in Figure 3.5. A GMM label map for annealed P3HT:$PC_{61}BM$ is shown in Figure 3.5a, below its input channels and GMM labeled property distributions. As seen in these results, even though the bulk heterojunction (BHJ) morphology is markedly different from the morphologies in previous figures, the same workflow and GMM segmenter was able to cluster material response signals into highly anisotropic and asymmetric domains, closely matching the input data's morphology.

As an examination of a case of significant anisotropy, P3HT nanowires were also examined with the same m2py workflow. The results of the GMM classification are shown in Figure 3.5b, above their input channels and GMM labeled property distributions. Even though these P3HT nanowires are even more anisotropic than the BHJ domains, m2py is still able to accurately parse

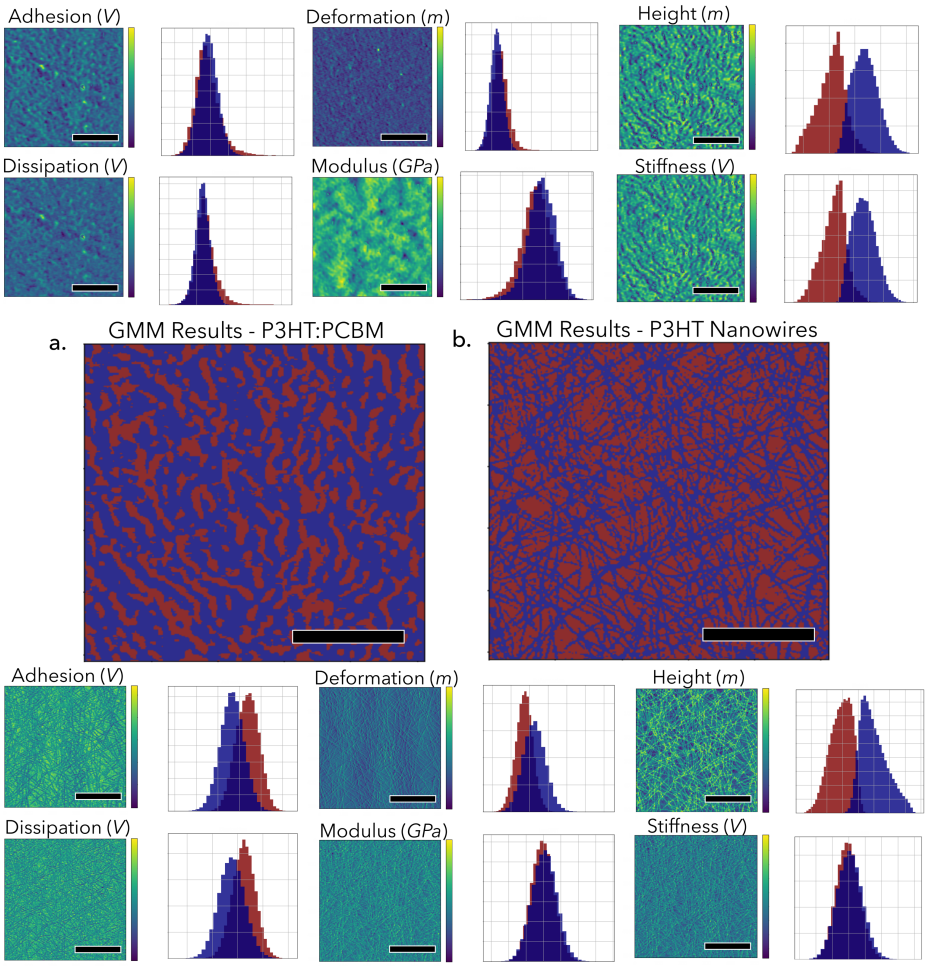

Figure 3.5. Results of GMM segmentation on two different samples. **a.** Two component classification of a P3HT:$PC_{61}BM$ thin film, where red and blue corresponds to the different components. The input channels are shown in the top two rows alongside their material-property signal distributions that are color coded by GMM component. Scale bars are 200 nm, images are 256 × 256 pixels. **b.** Results of two component classification of P3HT nanowires (blue) spin-coated onto a passivated SiO_2 substrate (red). The input channels are shown in the bottom two rows, alongside their corresponding material-property signal distributions color coded by GMM phase components. Scale bars are 500 nm, images are 512 × 512 pixels.[153]

between the nanowires, the SiO_2 substrate, and scanning defects, such as tip-scars. This is a useful result because tip-scars occur commonly with sharply featured samples, such as nanowires, and can visually resemble the material domains. Regardless, of this effect m2py is able to distinguish nanowires from tip-scars by using differences in their material response signals. Despite the complex and varied morphologies of CP thin films, m2py's workflow has no problem interpreting both highly anisotropic CP morphologies and simpler or axisymmetric morphologies.

3.3.3 *Instance Segmentation*

The identification of each pixel's GMM phase within a scan allows a great deal of insight into SPM images, but much of the salient information lies in the size and distribution of pixel clusters, which construct the morphological domains and features. Unlike semantic segmentation, instance segmentation (pixel clustering) requires different techniques to handle different morphologies. The m2py toolkit currently implements two different instance segmentation methods: connected components labeling and persistence watershed segmentation (PWS), although additional instance segmentation methods could be easily integrated into m2py workflows.

The connected component labeling mechanism takes in the label map from GMM segmentation and applies a graphical algorithm that clusters tangential pixels that have the same GMM phase label.[150] Those connected pixels that have the same GMM label are assigned a unique domain label. The level of connectivity can be adjusted to include either only the four pixels that share an edge with the pixel in question, or to also include the four corner pixels. The total number of unique labels denotes the total number of domains present in the sample. Domains are sorted by size before receiving a label, meaning that domain 1 has the most pixels, and the domain with the

fewest pixels is listed last. Adjustable thresholding is used as needed to combine domains that may be too small to be physically valid.

The other instance segmentation method, PWS, applies a watershed approach to identify domains. Watershed segmentation is commonly used in greyscale morphology description.[161] In m2py, we use a single channel – the height channel is used as default – to act as the magnitude values that form watershed-derived segments, which represent morphological domains. Other channels or labels, such as a principal component, can be used for PWS segmentation instead of height, as desired. Standard watershed approaches tend to over-segment images. To address this issue, the PWS model employs persistent homology to merge watershed-derived segments incrementally to form larger domains.[162] Initially, too many segments arise due to noise, which indicates that a low merging threshold will result in too many identified domains. As the threshold is increased, these over-segmented regions merge and fewer domains remain. At the critical point where the most noise is eliminated and the most domains are preserved as segments, there is a sharp decrease in the number of domains, as shown in Figure 3.6. A rigorous discussion on selecting the appropriate instance segmenter, based on morphological structures, is given in the Supporting Information. Figure S3.3 shows a comparison of instance segmenters on 4 different morphologies. In short, we find that PWS is better for more isotropic morphologies and systems where tangential domains may be separate, whereas connected components labeling is ideal for highly anisotropic and irregularly shaped morphologies. Figure 3.6 shows the analysis of a PTB7:$PC_{71}BM$ sample and throughout the m2py workflow. The clearly visible spherical aggregates in the input height channel resembles the same information observed in the rest of the channels. GMM identifies these aggregates as a different phase than the matrix constituent, and labels them accordingly. Next, the height channel is used for instance segmentation with PWS.

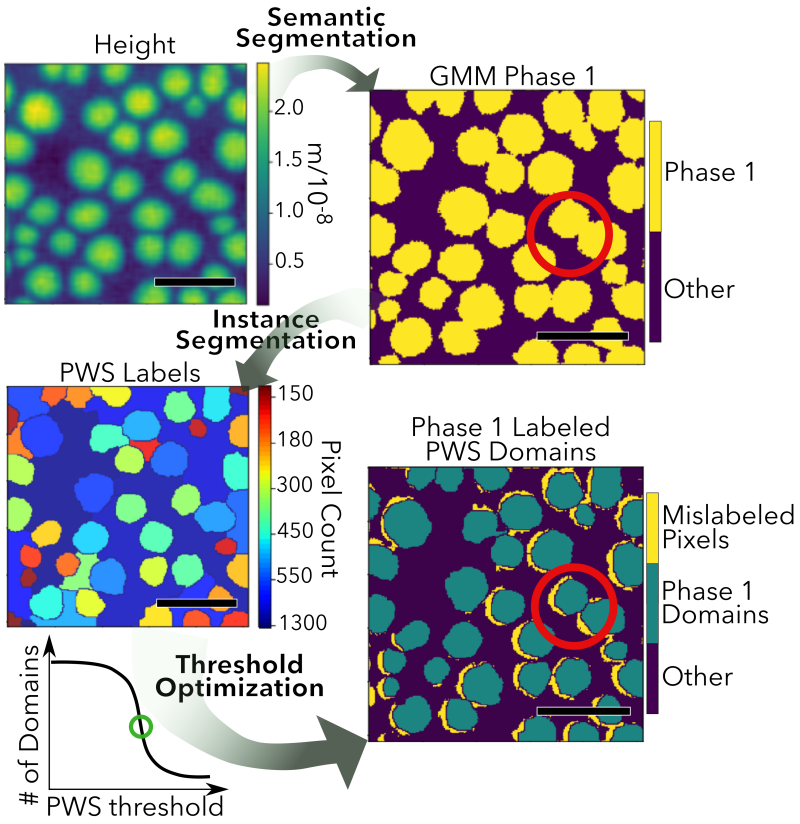

Figure 3.6. A representative channel from a FDM image of PTB7:$PC_{71}BM$ is shown, followed by the results throughout m2py analysis of the image. First undergoing semantic segmentation, the resulting GMM phase labels show the spherical aggregates to be a distinct phase from the matrix. Phase 1 is shown in yellow, phases 2 and 3 are combined in purple. Next, the height channel is used in instance segmentation by the PWS method, producing individually indexed morphological domains. The color of each individual domain is selected according to its size. Finally, PWS labels that correspond to GMM phase 1 are plotted in green and the mislabeled phase 1 pixels plotted in yellow for contrast. Scale bars are 1 μm, images are 512 × 512 pixels.[153]

The individual aggregates, as well as different domain boundaries in the matrix, are identified and labeled according to their size. Finally, the PWS domains corresponding to the GMM phase 1

pixels are shown. By comparing these PWS labels against those from the initial GMM segmentation, we can see that the PWS slightly underestimates the size of these domains, as represented by the residual yellow coloration. In this case, the labelling error is less than 7% of the total image area. This error may reflect the dilation of GMM labels from tip-effects, as a learning from multiple channels, some more highly influenced by tip-radius, while PWS is based on a single channel. Erosion operations have been implemented to successfully reduce tip distortions, however tip-deconvolution during pre-processing would more accurately reflect the surface morphology in GMM labeling. Future work will include expanding m2py's pre-processing and segmentation modules with such functions.

Regardless of the instance segmenter that is used, a major consideration of instance segmentation is to establish a threshold for what comprises a morphological domain. Molecular and crystal structure information is useful for establishing a minimum number of pixels required to be labeled as an individual domain. In m2py, this instance segmentation threshold, label_thresh, is easily altered in the post_processing.py module to suit the parameters of the material and measurement. In our FDM experiments, the probe tips had radii of ~7 nm, which correspond to ~19 monomer units of P3HT or ~5 monomer units of PTB7. Given the community understanding of the crystallographic dimensions of these materials, the amount of polymer that interacts with the surface area of the probe tip is similar in size to a domain and could reasonably be considered an entire domain or aggregate. Therefore, a single pixel could be the optimal threshold, although higher resolution measurements would certainly provide a more detailed insight into the exact morphological structure.[57,62,163] The P3HT nanowires shown in Figure S3.1 have been measured in previous work to be 20 nm wide, or approximately 2 pixels, with lengths of up to a micron.[40,89] A threshold of 4 pixels, therefore, can provide detailed morphological insight for our imaged

nanowires and P3HT thin films. Lastly, phase-separated, binary thin films may have dimensions of domains on a similar length scale, but these morphologies tend to require larger thresholds because the total area of the domain is larger. For example, the domains shown in the third row of Figure S3.1 contain at least 100 pixels each, with the background domain containing tens-of-thousands of pixels. These results emphasize the need for material-specific information to correctly interpret morphologies, although only minimal prior knowledge is needed for m2py to correctly identify morphologies.

3.3.4 *Final Output and Transferability*

As m2py classifies and clusters each pixel, it creates new label maps that can be analyzed separately or collected and appended to the original 3D image matrix for further analysis. Because these label maps correspond to the pixels in the original image, the properties of each pixel within any given phase or domain can be easily accessed. For example, histograms of the materials-property signals in each phase is easily determined from the GMM labeling. Further, by using the unique domain labels from instance segmentation each domain can be quantitatively examined. These domains can then be sorted by their corresponding GMM label, as shown in Figure 3.7b. Then, domain metrics are readily extracted, such as length, width, perimeter, and orientation.[150] Because the domains are uniquely labeled, these domain measurement methods can be iteratively applied to all of the domains in an image, as shown in Figures 3.7c-e. When sorted by GMM label, the size of the domains in each phase can also be determined, as presented in Figure 3.7c. In the example shown, an annealed P3HT:$PC_{61}BM$ thin film's height channel is shown (Figure 3.7a) and GMM segmenting labels for 2 distinct phases are created (Figure 3.7b). After semantic segmentation, it is clear that phase 1 domains comprise the matrix, which is colored red in the

domain label map. However, it is visible that the matrix phase is not entirely co-continuous, so non-contiguous phase 1 domains are considered separate from the large matrix domain by the instance segmenter and therefore receive unique domain labels (Figure 3.7b, *left*). The matrix domain is the largest in the sample and is visible as the 'outlying' data point in the major-axis length and area plots, as shown in Figures 3.7c-e.

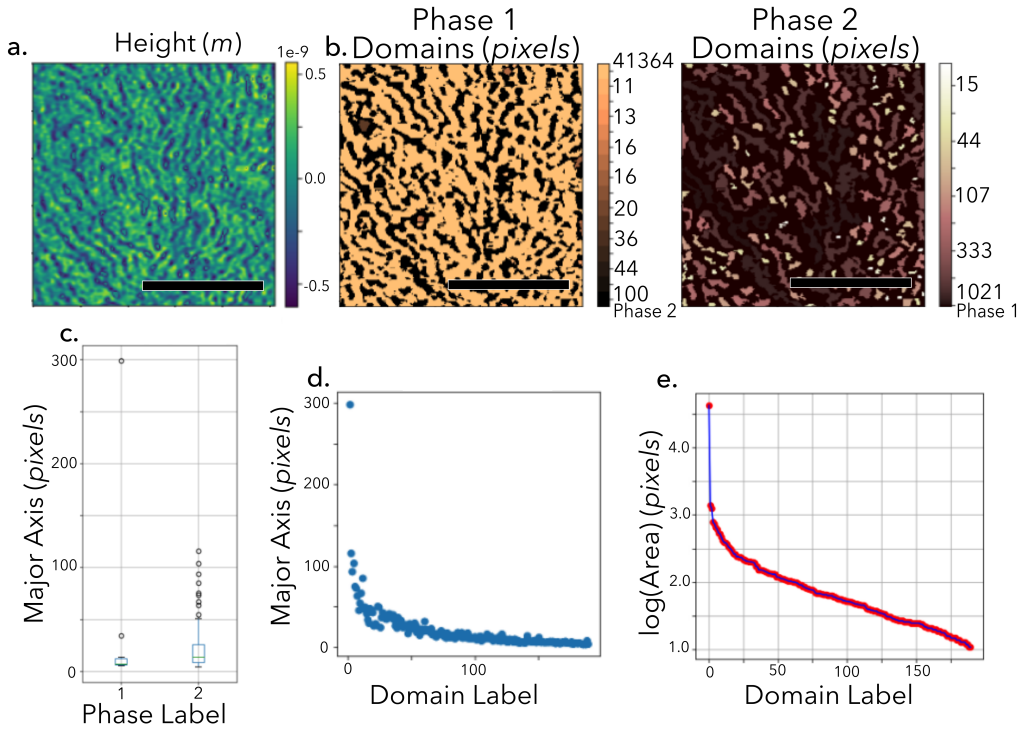

Figure 3.7. Throughout the m2py workflow, labels can be used to calculate and analyze relative ratios, property distributions, and domain descriptors. Simple examples are presented for a P3HT:$PC_{61}BM$ thin film. **a.** The height channel from FDM analysis of a P3HT:$PC_{61}BM$ thin films is shown. Colorbar units are relative. **b.** Domain labels are determined by connected components labeling and then sorted by their GMM label. The color of each individual domain is selected according to its size. (*left*) Phase 1 domains, with black domains being phase 2. The co-continuous matrix domain is remapped to the lightest color for visibility. (*right*) Phase 2 domains, with black domains being phase 1. **c.**

The major-axis length, in pixels, of connected components labeled domains, sorted by GMM label. **d.** The major-axis length, in pixels, of connected components labeled domains. **e.** The log of connected components labeled domain areas in pixels. The scale bars are 1 μm and the images are 500 × 500 nm and are 256 × 256 pixels.[153]

These results illustrate m2py's ability to identify and quantify morphological domains in SPM FDM data. In order to ensure the compatibility of this toolkit with other SPM techniques, m2py includes a config.py module where users can define the channels and dimensions of their unique SPM measurement. The specific parameters of each technique are defined in a python dictionary within the config.py module, where users can enter the number of channels, the type of information the channels contain (*e.g.* "Young's Modulus" or "Phase"), and the dimensions of their scans. As shown in Figure 3.8, m2py is already adapted to C-AFM and AMFM images. In Figure 3.8a, the results of AMFM imaging of P3HT nanowires on passivated ITO glass are shown next to their m2py label maps. On the far right, the domains corresponding to the nanowire phase (phase 1) are plotted in yellow. Figure 3.8b shows a similar sample of P3HT nanowires imaged through C-AFM next to the corresponding m2py label maps, Because the probe-tip used in C-AFM is far larger than that of AMFM, ~50 nm and ~11 nm respectively, the nanowires appear distorted in Figure 3.8b. However, we observe in Figures 3.8a and 3.8b that the recognized nanowire domains closely resemble the input data. By applying a morphological dilation and subsequent erosion,[150] the m2py toolkit's interpretation is not hindered by these varied probe-tip resolutions, nor by the reduced number of input data channels. To use, expand, or contribute to the m2py toolkit, readers are directed to the open-source Github repository github.com/ponl/m2py. We hope the community will aid in suggesting additions, developing modules, and optimizing the toolkit. We believe that

our customizable workflow can augment and expound upon any existing SPM interpretative software and incorporate into any Python-based tools.

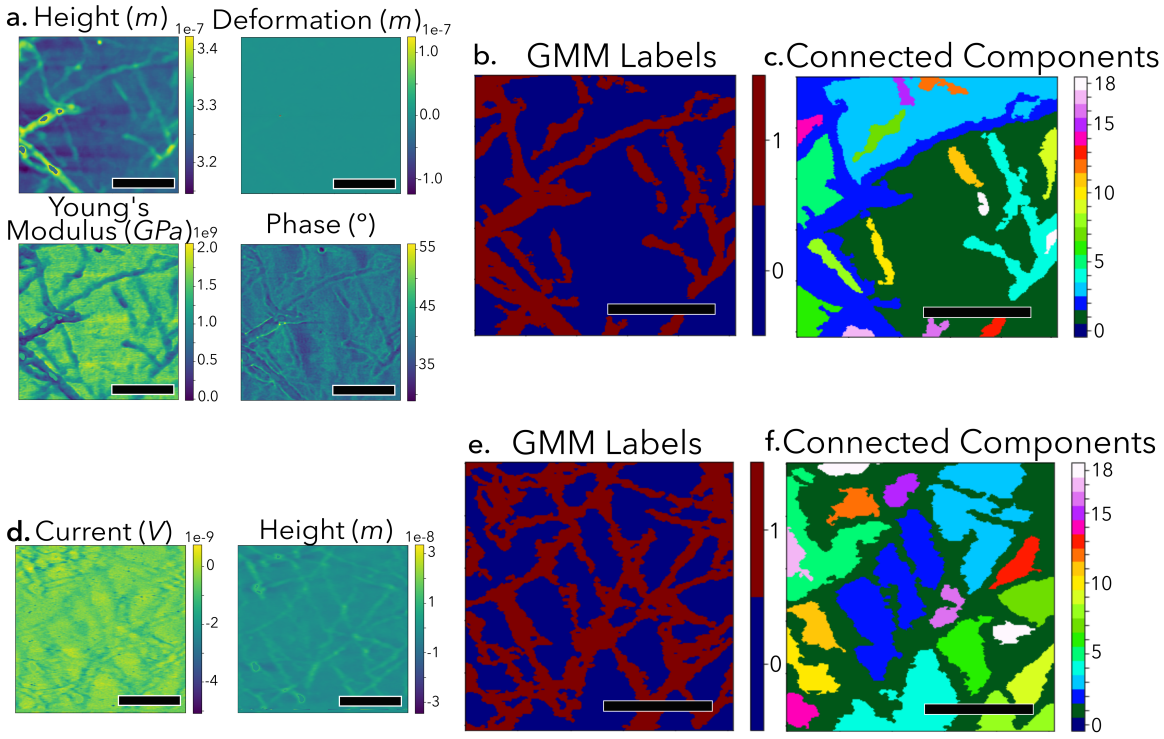

Figure 3.8. Input data channels and m2py labeling results for P3HT nanowires spin-coated onto passivated ITO glass. **a.** Property channels of AMFM measurements of P3HT nanowires on ITO glass. Colorbar units are relative. **b.** GMM labels with coloring corresponding to GMM phase labels. **c.** Connected components labels. The color of each individual domain is selected according to its. **d.** Property channels for C-AFM measurements of P3HT nanowires on ITO glass. Colorbar units are relative. **e.** GMM labels with coloring corresponding to GMM phase labels. **f.** Connected components labels. Scale bars are 200 nm, images are 256 × 256 pixels.[153]

3.4 CONCLUSIONS

The m2py library is a set of modular and adaptable tools for the quantitative description of morphologies from SPM images. By implementing a combination of numerical and unsupervised methods, m2py enhances and isolates material-property signals, which are then used to classify each pixel and cluster them into their corresponding domains. This study has highlighted m2py's capacity to interpret and identify morphological domains across a wide range of samples of π-conjugated polymers. The resulting labels maps can be used to quantitatively describe the labeled morphologies. Our general workflow is easily modified and allows users to quantitatively evaluate and compare morphological features, domains, and phase distributions in an automated fashion. Finally, additional preprocessing, subsampling, and segmentation methods will be added to improve and expand m2py's morphological interpretations, handle RGB or electron microscopy images, and facilitate their labeling. Future work will report on these additions and seek to understand the connection of such morphological descriptions to device performance will use the m2py framework to quantitatively describe and optimize the morphologies of thin film electronic materials.

3.5 SUPPORTING INFORMATION

3.5.1 *Data Intake and Pre-Processing (Continued)*

It is well known that outliers and aberrant data points can distort data analysis. In the case of unsupervised image segmentation, outlier pixels can overwhelm clustering mechanisms by having signals that can be up to orders of magnitude larger than the material-property signals of interest. In order to detect and remove such signals, m2py implements two methods. The first, shown in Figure S3.1, convolves the input channels with a blurring filter to diminish small differences

between pixels. Then we apply a z-score filter to extract outlier pixels. By default, this method flags all pixels that are 2.5 standard deviations from the mean value. This method results in a Boolean label map, where outliers are flagged with the value 1. This method can be applied to either a single channel or all channels, with the default being only the height channel. If multiple channels are evaluated, the Boolean label map is a composite of all flagged pixels from all channels evaluated. Using this map, outliers can be either ignored (for the purposes of further analysis) or have their values re-mapped (for the purposes of visualization).

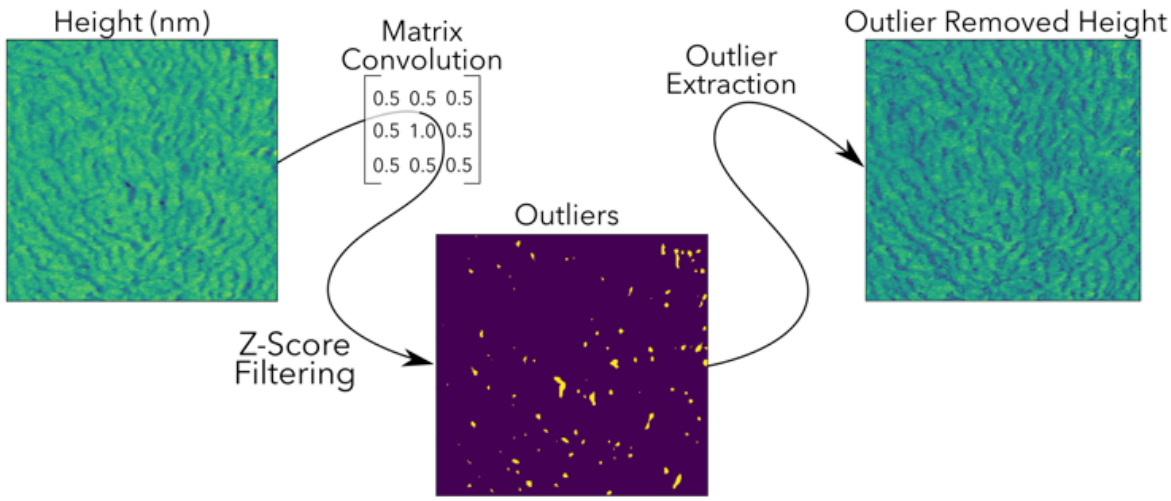

Figure S3.1. In order to detect outlier pixels in an image, the z-score of all pixels is computed. Z-score values surpassing an adjustable threshold are identified as outliers. Outliers are re-assigned the median value of the channel to improve visualization of the sample. P3HT:$PC_{61}BM$ FDM, 500 × 500 nm and imaged with 256 × 256 pixels.[153]

The second method for outlier removal applies image denoising via a fast Fourier transform (FFT). In SPM images, there are often noise signals in either the low-frequency or high-frequency regime. Transforming the image into Fourier-space allows these specific signals to be identified

and removed through a band-pass filter. As shown in Figure S3.2, keeping the lowest frequency signals sharpen the edges and features of morphological domains.

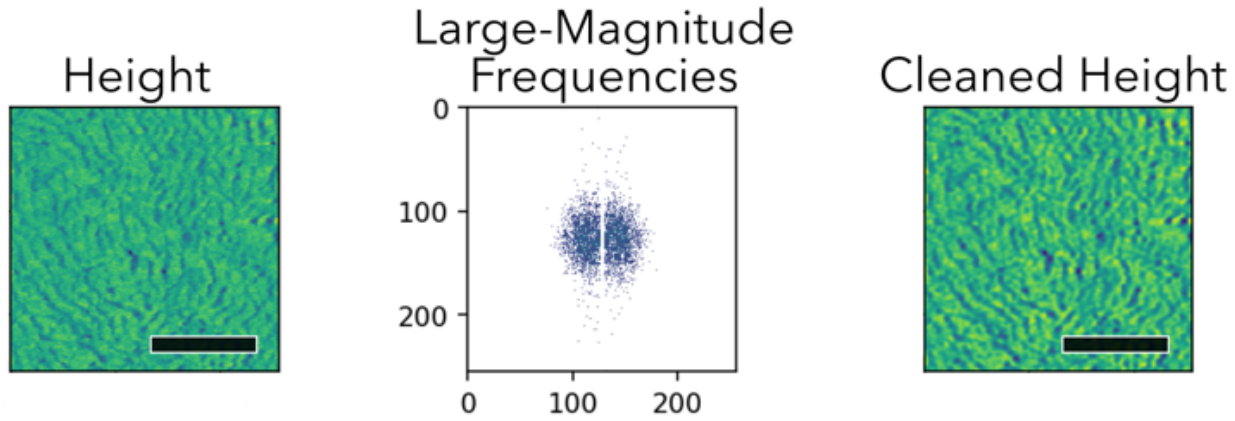

Figure S3.2. In order to enhance the clarity of images and remove background noise, each channel undergoes a fast Fourier transform. While in Fourier-space, an adjustable band-pass filter is applied to remove noisy frequencies. Shown above is an example channel from a P3HT:$PC_{61}BM$ FDM image before and after the 5% lowest-magnitude frequencies are removed (*i.e.* 95% of the signals remain). The scale bar is 200 nm, image is 256 × 256 pixels.[153]

3.5.2 *Feature Selection (Continued)*

Beyond channel exclusion, such as the 'heightless' flag described in section 2.2, m2py has additional methods that amplify material-property signals for GMM classification. For instance, in order to probe for non-linear relationships, the 'non-linear' flag in the SegmenterGMM() class automatically appends the square, cube, inverse, and absolute value of each channel as new channels. Doing so allows for more complex relationships between channels and within data to be

explored by the microscopist and utilized by the rest of the m2py workflow. This function is easily expanded or modified to allow for the probing of different non-linear relationships in segmentation_gmm.py.

In some cases, the information gathered from individual pixels is insufficient for the GMM segmenter to accurately segment into their corresponding components. This can occur when a phase exhibits a wide range of values for a given property. To resolve this, the user can include wider context from the sample by using neighboring pixel values to weight the classification. By including local environment information in classifying the pixel, accuracy of classification can be increased. This functionality is also accessed during the SegmenterGMM() instantiation by calling a padding value to include information from the neighboring pixels (*i.e.* a padding value of 1 will include 8 tangential pixels). Finally, all the raw features and newly appended features must go through standardization prior to passing them to principal component analysis. M2py's default standardization method transforms the input domain for each feature to the [-1, 1] domain, which is a valid range given that we have already removed outliers from the underlying distributions. The backup method is to transform the underlying feature distributions to standard normal distributions. Both of these methods are configurable during the SegmenterGMM() instantiation.

3.5.3 *Semantic Segmentation*

In order to optimize GMM segmentation, the raw data can be expressed as a collection of N pixels, $\{x_j\}_{j=1}^{N}$, with each pixel having M features (*i.e.*, $x_j \in M$). In essence, the underlying distribution of the data features, $p(x)$, is modeled as a convex sum of K Gaussian kernels, where K denotes the user-specified number of components. That is,

$$p(x) = \sum_{i=1}^{K} \phi_i N(x|\mu_i, \sigma_i)$$

where

$$N(x|\mu_i, \sigma_i) = \frac{1}{\sigma_i\sqrt{2\pi}} \exp\left(-\frac{(x-\mu_i)^2}{2\sigma_i^2}\right)$$

and

$$\sum_{i=1}^{K} \phi_i = 1.$$

In order to optimize the parametric values arising from the GMM framework ($\mu, \sigma,$ and ϕ), we use the expectation maximization (EM) algorithm to solve the GMM optimization problem. We start by initializing the parameters $\{\mu_i\}_{i=1}^{K}$, $\{\sigma_i\}_{i=1}^{K}$, and $\{\phi_i\}_{i=1}^{K}$ in the following fashion: the means $\{\mu_i\}_{i=1}^{K}$ get assigned randomly sampled pixel values, the variances $\{\sigma_i\}_{i=1}^{K}$ get assigned the sample variance of the system, and the component distribution priors $\{\phi_i\}_{i=1}^{K}$ are initialized with equally likely contributions. Then we proceed iteratively with the expectation and maximization steps as follows:

Expectation step: The likelihood that data point x_j is generated by component C_k is given by

$$\gamma_{j,k} = p(C_k|x_j, \phi_k, \mu_k, \sigma_k) = \frac{\phi_k N(x_j|\mu_k, \sigma_k)}{\sum_{i=1}^{K} \phi_i N(x_j|\mu_i, \sigma_i)}.$$

Maximization step: Update the model parameters accordingly:

$$\phi_k = \sum_{j=1}^{N} \frac{\gamma_{j,k}}{N},$$

$$\mu_k = \frac{\sum_{j=1}^{N} \gamma_{j,k} x_j}{\sum_{j=1}^{N} \gamma_{j,k}},$$

and

$$\sigma_k = \frac{\sum_{j=1}^{N} \gamma_{j,k}(x_j - \mu_k)^2}{\sum_{j=1}^{N} \gamma_{j,k}}.$$

The expectation and maximization steps are repeated until the convergence criteria has been satisfied. Finally, the probability of data point x belonging to component C_k is given by,

$$p(C_k|x) = \frac{\phi_k N(x|\mu_i, \sigma_i)}{\sum_{i=1}^{K} \phi_i N(x|\mu_i, \sigma_i)}.$$

3.5.4 *Instance Segmentation (Continued)*

Because m2py has multiple instance segmenters that cluster GMM-labeled pixels into domains, selecting the correct segmenter is crucial. Here, we show that methodologies tend to be more suited for some morphologies over others by examining four different, common morphologies. The simplest morphology, unexplored in this work, is a uniformly ordered atomic lattice. Although m2py modules are expected to be compatible with these techniques, discussion of their segmentation and thresholding are beyond the scope of this investigation. On the other hand, SPM imaged samples with lower resolution on a larger scale, and are widely used in investigating CP. Further, polymers have greater amorphous content, with even highly aligned and crystalline CPs having a metric of cumulative lattice disorder, paracrystallinities, as high as 10%.[57] This makes their morphologies more locally stochastic and, therefore, more difficult to precisely image and interpret. In the active layers we have imaged in this work, the rapid drying of spin-cast films causes kinetically trapped and stochastically distributed, liquid-liquid phase-separated morphologies. Such a morphology is exemplified by an unannealed PTB7:$PC_{71}BM$ thin film (Figure 3.4).[109,164,165] As shown by the annealed P3HT:$PC_{61}BM$ sample (Figure 3.5a), thermal annealing allows the thin films to evolve towards a more thermodynamically preferred and anisotropically structured morphology. Both of these morphologies are well classified by m2py,

as evidenced by the structural similarity of the domain label maps to their input data. This is shown for four different samples in Figure S3.3.

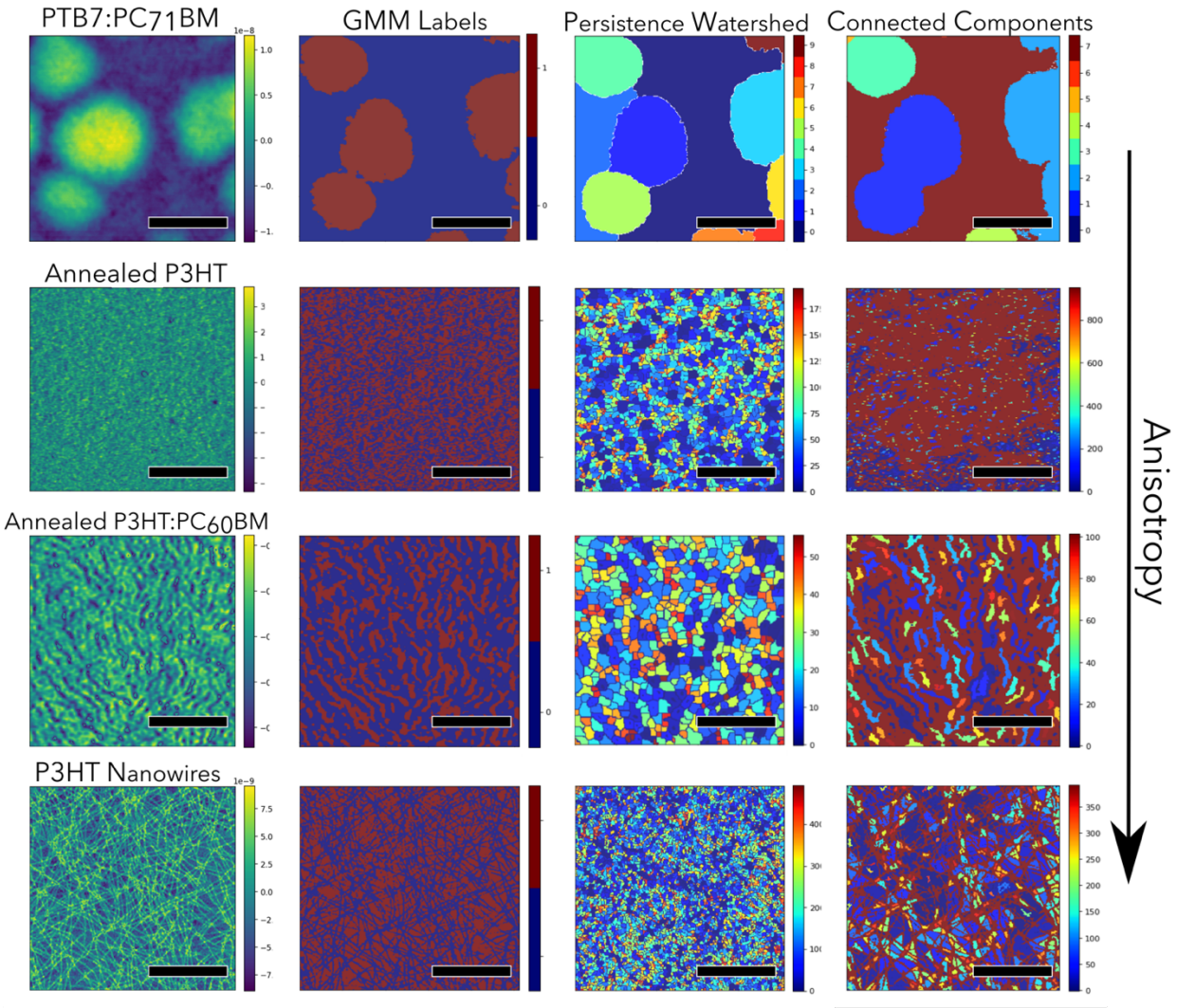

Figure S3.3. Results of m2py semantic (GMM) and instance segmentation (persistence watershed and connected components) for four different samples, one per row. The height channel of each sample is shown in the far-left column, GMM results are shown in the second column. PWS labels, sorted by their size are shown in the third column, and connected components labeling in the fourth. Scale bars are (top to bottom) 200 nm, 200 nm, 500 nm, and 200 nm, and images are 512 × 512, 512 × 512, 512 × 512, and 256 ×

256 pixels, respectively. False color bars on the clustering images correspond to the domain indexing labels, which are integers.[153]

The top row of Figure S3.3 shows the simplest active layer morphology presented in this study, monodisperse spheres embedded in a homogeneous matrix. This morphology has highly symmetric, smooth features where spherical, $PC_{71}BM$-rich domains are separated by the PTB7-rich matrix. This sample presents a semi-diffuse transition between the $PC_{71}BM$-rich domain and the PTB7-rich matrix, the details of which are well captured by the GMM segmentation. The subsequent instance segmentation of this image is best handled with PWS, which is able to distinguish tangential but separate domains of the same component. The difference in performance between these connected components labeling and persistence watershed is visible in the last two figures of the row. It is always difficult to identify the ideal threshold for merging segments, which distinguishes between segmenting tangential domains of the same phase, and over-segmenting the whole domain. Fortunately, a biproduct of persistent homology is the persistence diagram, which simplifies the automation of selecting an ideal threshold selection by measuring how many segments would exist for each possible threshold. The persistence diagram identified threshold is also ideal for a thin film of annealed P3HT, shown in the second row of Figure S3.3. Even though the GMM segmentation is able to identify many different, small domains of amorphous and crystalline P3HT, connected components segmentation combines tangential domains of the same component. However, PWS interprets high symmetry morphologies more consistently with observations of the input data and doesn't necessarily combine tangential domains.

CP active layers can also often exhibit highly anisotropic domains, especially when the thin films are highly crystalline and molecules become more aligned.[166] Even amorphous CPs blended with another material can show a bi-continuous phase distribution.[124,167,168] As opposed to spheres in a

matrix, bi-continuous morphologies exhibit intricately intertwined domains, seen in the third row of Figure S3.3. The $PC_{61}BM$-rich phase is the blue phase in the GMM results, shown in the second column, and it separates the highly anisotropic and asymmetric P3HT-rich domains, shown in red. This morphology is interpreted well by GMM, but PWS over-segments the domains into smaller, more spherical domains that do not resemble the morphology in the input data, exemplified by the height channel in the first column. The connected components methodology is most effective in clustering this morphology's domains because it combines tangential domains of each component into non-spherical domains, which are well isolated by the matrix. Even in the extreme, connected anisotropy of P3HT nanowire networks, shown in the fourth row of Figure S3.3, the connected components segmenter distinguishes nanowires from substrate best. Therefore, when morphologies are anisotropic and asymmetric, the connected components segmenter outperforms the persistent watershed method.

Chapter 4. USING QUANTITATIVE MORPHOLOGY TO EXPLAIN AND PREDICT DEVICE PERFORMANCE

4.1 INTRODUCTION

The performance of thin film electronic devices is strongly dependent on the morphology of the active layer. In order to gain an understanding of CP morphology and its development it is crucial to develop methods for extracting quantitative morphological information on the nanometer- and micrometer-scale, as it is often features at these length scales that determine bulk performance for CP-based devices.[169–172] The current standards for quantitative measurements of morphological parameters, such as crystal structure and crystallinity, are XRD and DSC, which are bulk-averaged measurements. This means that they are insensitive to minute changes in local- and device-scale morphology. In order to progress towards truly predictive models of device performance, quantitative, reproducible and spatially resolved descriptions of local morphology are critical.

The work presented in this chapter builds on the m2py labeler.[173] In order to examine how informative the m2py labels are, and how predictive they are of device performance, two different datasets are labeled and used to train supervised regressors. Specifically, m2py phase and domain labels are given to the active layers of OPV and OFET devices, which have received different thermal annealing treatments, and the labeled data is used to predict final device performance. The OPV dataset will be the focus of this report, but future publications will include analysis of the OFET dataset as well. These devices are created from common and well-studied organic semiconductors, P3HT:$PC_{61}BM$ and P3HT respectively, and are subjected to thermal annealing conditions that are commonly used in investigating the optimization of CP thin film electronics. This work investigates various methods of incorporating morphological information into models

that predict performance and how these labels affect the accuracy of both traditional regressors (decision trees, support vector machines, and ridge regression) and artificial neural networks. The error and accuracies of these different models and datasets are compared; these trends are used to determine the extent to which morphological information improves predictions of device performance.

4.2 Methods and Materials

Unless indicated otherwise, all materials were purchased and used as-received from Sigma-Aldrich. P3HT was purchased from Rieke Metals or synthesized using previously reported methods;[75] PTB7 was purchased from Cal-OS; and $PC_{71}BM$ was purchased from Solenne BV. Si/SiO_2 and glass/ITO substrates were purchased from WRS.

4.2.1 *Regression and Code Development*

All modules were written in Python. NumPy[146] was used for the preparation and manipulation of data. PyTorch was used to create and train all networks.[174] Matplotlib[148] was used to create all plotting capabilities. scikit-learn[149] was used for regression and optimization.

4.2.2 *Substrate Preparation*

All substrates were cleaned by scrubbing with soap and DI water, followed by sonication in deionized water, acetone, and isopropyl alcohol for 15 min each. Following sonication, the substrates were dried under a stream of air and subsequently plasma cleaned for 15 minutes using O_2 plasma.

For P3HT OFET, passivated substrates were used. To passivate the substrates, the substrates were taken directly from the plasma cleaner and placed under vacuum within a crystallization dish

to allow the vapors from an open vial containing 400 μL of octadecyltrichlorosilane (OTS) to interact with the surface. The system remained under dynamic vacuum for 1 hour and was then switched to static vacuum. The system was heated at 125 °C for at least 3 h to ensure evaporation of the OTS. After this, the heat was turned off and the system was allowed to rest under static vacuum over-night to allow the OTS vapor to self-assemble on the surface. Physisorbed and self-polymerized OTS was removed by rinsing with isopropyl alcohol, leaving behind only the self-assembled monolayer of OTS, onto which the P3HT and nanowire films were directly spin-coated.

4.2.3 *Thin Film Deposition*

P3HT:$PC_{61}BM$ blends (1:0.95, total concentration 30 mg mL^{-1}) were stirred in chlorobenzene overnight at 70 °C prior to spin-coating. P3HT thin films were dissolved into chloroform at a concentration of 5 mg mL^{-1} and stirred at 50 °C overnight prior to spin-coating. Spin-coating was performed using the following spin-speed and durations: P3HT:$PC_{61}BM$ (1000 rpm, 60 sec) and P3HT (2500 rpm, 60 sec). Solution preparation and spin-coating were all carried out in a nitrogen glovebox.

4.2.4 *OPV Devices and Testing*

Freshly cast active layers were sealed under nitrogen and transferred to a different glovebox for thermal evaporation of the contact electrodes. Using an Ångstrom Engineering NextDep PVD system, 10 nm of MoO_3 were deposited, followed by 100 nm of Ag. Both films were deposited at 0.5 Å/s under no more than 10^{-6} torr of pressure. Through a photomask, 8 different back contacts and a single front contact was deposited. After contact deposition, the devices were annealed for the various temperature ranges prescribed by Table 4.2, still in the glovebox. Finally, using a VeraSol Solar Simulator, *J-V* profiles were extracted while the devices were under AM 1.5

illumination. A range of biases from -0.2 to 1.0 V was used. After testing, the samples were transferred to a glovebox for storage before the active layers were imaged with AFM. *J-V* curve analysis was performed to extract power conversion efficiency (*PCE*), open-circuit voltage (V_{oc}), short-circuit current (J_{sc}), and fill factor (*FF*). The Python code associated with this GUI is available open-source and free of charge from www.github.com/wesleyktatum/OPV_analysis

4.2.5 *OFET Devices and Testing*

Freshly cast active layers were sealed under nitrogen and transferred to a different glovebox for thermal evaporation of the contact electrodes. Using an Ångstrom Engineering NextDep PVD system, 100 nm of Au as deposited at 0.5 Å/s, under no more than 10^{-6} torr of pressure. Through a photomask, 20 different devices were evaporated, each with a channel width of 1000 μm and a channel length of 50 μm. After contact deposition, in a corner of the substrate, a small area was thoroughly scored to expose the heavily p-doped Si substrate. On this exposed conductor, a small piece of indium was pressed on, to serve as a gate-electrode contact for all the devices. Then, the substrates were annealed for the various temperature ranges prescribed by Table 4.3, still in the glovebox. Finally, using a Signatone Probe Station, linear regime transfer curves were extracted with a gate voltage range of 5 to -95 V, with a drain bias of -20 V. After testing, the samples were transferred to a glovebox for storage before the active layers were imaged with AFM. Transfer curve analysis was performed to extract the linear regime charge-carrier mobility (μ*),* ideality coefficient (*r*), on-off ratio, and threshold voltage (V_{th}). The Python code associated with this GUI is available open-source and free of charge from www.github.com/wesleyktatum/OFET_analysis

4.2.6 *Force-Distance Mapping (FDM)*

AFM micrographs were obtained on a Bruker ICON AFM in Peak- force Quantitative Nanomechanical Mapping mode. ScanAsyst-Air tips were used for these measurements (SiN/Al, ~70kHz, and 0.4 N m^{-1}).

4.3 Results and Discussion

4.3.1 *Data and Sampling*

OPVs made from P3HT:$PC_{60}BM$ were fabricated and thermally annealed across various temperatures and durations, as shown in tables 4.1 and 4.2. Once fabricated, the devices were tested under N_2 atmosphere to determine four different metrics of their performance. For OPVs, these were power conversion efficiency (*PCE*), open-circuit voltage (V_{oc}), short-circuit current (J_{sc}), and fill factor (*FF*). After testing, the active layers were imaged using force-distance mapping (FDM) AFM. To sample the active layers' morphology, three representative 1 μm^2 scans were taken for each substrate, which held 8 devices. The architecture of the OPV devices preclude taking scans directly in the active layer area; however, scans were taken adjacent to devices that were included in the study. Only devices with PCE above 1% were included in the final dataset, except for the control samples that were not annealed, and which performed poorly. The resulting images where labeled with domain and phase labels using an m2py workflow that was optimized separately for the OPV and OFET datasets, following the guidelines outlined in the previous chapter. Scripted workflows are available for viewing online at www.github.com/wesleyktatum/m2py. These m2py workflows mapped and assigned each pixel with two sets of 2D labels that describe the pixels' phase and domain. Representative plots of the OPV datasets are shown as supporting information in section 4.5, Figures S4.1-5 while a

comprehensive listing of plots is hosted online for free at www.github.com/wesleyktatum/py-conjugated, which contains Jupyter notebooks for all data and modeling investigations, as well as plots and Python modules used throughout the Jupyter notebooks.

Table 4.1. Thermal annealing conditions that devices in the P3HT:$PC_{61}BM$ OPV dataset were subjected to during device fabrication. Color indicates the relative amount of thermal energy that the active layer was exposed to, ranging from dark blue (low) to dark red (high).

OPV	5 min	15 min	30 min
100 ºC			
125 ºC			
150 ºC			
175 ºC			

Table 4.2. Thermal annealing conditions that devices in the P3HT OFET dataset were subjected to during device fabrication. Color indicates the relative amount of thermal energy that the active layer was exposed to, ranging from dark blue (low) to dark red (high).

OFET	5 min	10 min	15 min	30 min
75 ºC				
100 ºC				
125 ºC				
150 ºC				

Using the m2py labels and scikit-image domain measuring functions,[149,150] the domain size and shape was determined and recorded for every domain in each image. To include this morphological information as a training feature in the standard regression models, these domain measurement values were averaged across all the domains, per phase, in each image and stored in a tabular format, along with their standard deviation. By simplifying the m2py labels into summary descriptions, the morphology data is able to be directly incorporated into predictive models that may not be adaptable to image-like data. Further, when this data is used to train standard regressors, such as ridge-regression, the importance of different morphological features in the final prediction can be probed to more fully understand how morphology influences prediction of device performance. These regressors will serve as a baseline for performance to the neural networks proposed in this work.

Due to the ease of device testing versus FDM imaging, there are more measured devices in each dataset than there are FDM images of the active layers. In order to ensure consistent comparisons between models– including image-like morphology data and those relying solely on tabular data– a common validation set of 10 devices was selected and withheld from training. The training datasets used for these models are small, meaning that each dataset is below 500 training samples. In fact, the device-only data only has 366 OPV samples. The SPM derived datasets only contain 36 OPV images that show a 1×1 μm FDM scan of the active layer in 256×256 pixels. Although the sample sizes for these two datasets are too small to expect high degrees of accuracy, they are enough to provide comparative insight on the effect of quantitative morphology data. This underscores the low data requirements for these workflows, which again points to the critical importance of quantitative morphology descriptions for successfully predicting device performance. Finally, all data is subjected to MinMax normalization before regression to account

for differences in orders of magnitude between the different device metrics and the scale-variance of some of the regressors (*e.g.* support vector machines). For instance, with OFET, on/off ratios range from $10 - 10^6$, while r is a ratio value between 0 and 1.[175,176] If these values were left unnormalized, then the models will tend to fit only to the device metrics that are larger, rather than attuning equally to them all as we would want.

4.3.2 *Regression on Tabular Data Only*

In order to establish a baseline utility for quantitative morphology information, we wanted to summarize our full quantitative morphology to tractable features. To do this, we took the average and standard deviation of several morphology descriptors for each image's labeled, which were measured using skimage.measure.regionprops_table().[150] In the OPV, three phases were labeled by m2py, a polymer-rich, fullerene-rich, and mixed phase. For each of these phases in an image, the average and standard deviation was calculated for: filled area, extent, major axis length, minor axis length, eccentricity, orientation, and perimeter.[150] In addition to these summarized domain measurements, each phase's relative area in the image(relative phase area), and its total area in pixels (total phase area) were included as training features. So, for an image with three different phases identified (as with OPV), there are 74 training features that summarize the image's morphology and can be used to predict 4 different device performance metrics.

In order to fully incorporate the m2py labeled morphology data into predictive models, Neural Networks (NN) are used because of the flexibility with which they can encode different types of information. However, they are inherently black-box and closed to interpretation. So, to begin to look at how incorporating quantitative morphological information influences the prediction of different device performance metrics, we use a set of standard regression models of summaries of

the labeled morphologies. In the neural networks constructed for this work, the training features are encoded using a common input layer, after which the network divides into 4 separate branches– one to predict each metric. This network structure is intended to accentuate the interconnected nature of the effect that morphology has on device metrics, while also allowing the individual branches to be specialized for each device metric. However, with the more interpretable models, separate regression models predict *PCE*, V_{oc}, J_{sc}, and *FF*. In order to separate model variations from underlying connections in the data, we implemented Least Absolute Shrinkage Selection Operator (LASSO) regression, Random Forest (RF) regression, and Support Vector Machine (SVM) regression. In order to identify optimal hyperparameters for each standard regressor, scikit-learn's GridSearchCV() was used to fit combinations of hyperparameters specified in a parameter dictionary. For NN optimization, custom training and optimization protocol were built. The best combination of parameters was set and used to predict the final device performance. The best hyperparameters for each regressor are listed in Table S4.1 and a complete reporting of these hyperparameters and model optimization is available online at the associated directories in the Github repository www.github.com/wesleyktatum/py-conjugated.

To control for model performance variations and provide a baseline regression performance to compare against, each regressor was separately fit to two different sets of tabular training features: one including only the thermal annealing parameters (time and temperature) and the other including the described tabular morphological features summary. By comparing the results of each regressor trained on the different datasets, we can glean the impact that even these relatively condensed summaries of quantitative morphology data have on prediction accuracy. The preliminary results of these models are shown below in Figures 4.1 – 4.4. Full results will be included in future publications.

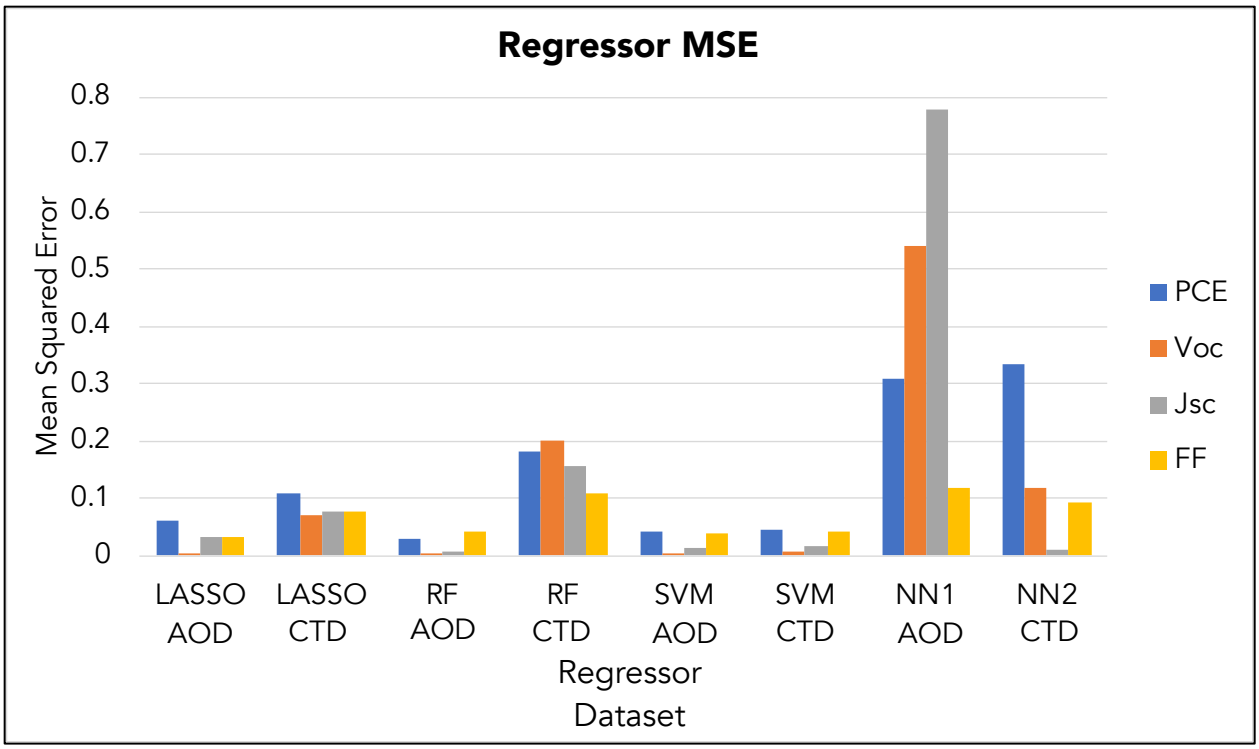

Figure 4.1. MSE for each model predicting 4 OPV device metrics (*PCE*, V_{oc}, J_{sc}, and *FF)*. Each model was trained on either the AOD or on the CTD.

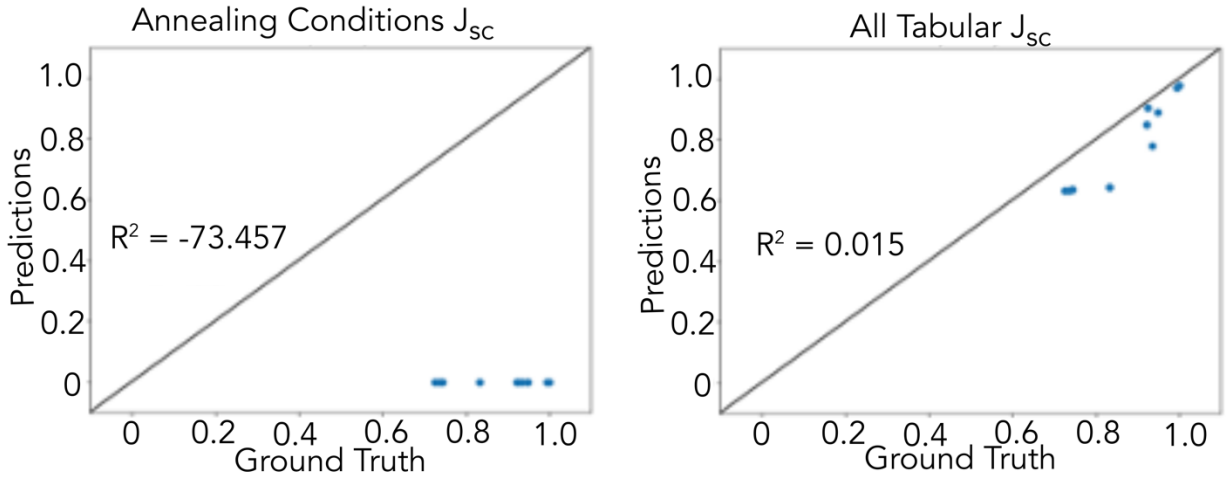

Figure 4.2. NN prediction of J_{sc} had the worst R^2 value when it only saw time and temperature data, but improved to the best R^2 after including tabular data summarizing the morphology of the device active layers.

In Figure 4.1, the mean-squared-error (MSE) loss is shown for each of the regressors as a means to track the difference between model predictions and ground truth values. In general, the loss for the annealing-conditions only dataset (AOD) was similar to or lower than that complete tabular dataset (CTD). This is remarkable because the sample size, N, for CTD is only 36, while N = 366 for the AOD. In light of this fact, it is clear that the addition of quantitative morphological information is highly beneficial to predicting final device performance. This improvement is largest for the NN prediction of J_{sc}, which went from the worst to the best performing model, as shown in Figure 4.3. RF and SVM models had the lowest losses overall, but RF did not show as significant of improvements upon introduction of the morphological information. Similarly, LASSO did not see better accuracy and predictions with the introduction of morphological information. It is interesting to note that the models that saw the most improvement from tabular morphological information, SVM and NN, are models that are most often used to evaluate information in images. These same identified patterns persist for the data presented in Figure 4.3, where the optimized mean-absolute-percent-error (MAPE) is shown. This is to be expected because MAPE similarly tracks the magnitude of the difference between model predictions and the ground truth.

In both of these model performance metrics, the variable that consistently appears to perform the best is V_{oc}. When we investigate the R^2 value for predictions made by these regressors, this assessment is shown to be incorrect, and that it's actually consistently the worst performing prediction. In their fits on AOD, the LASSO and RF models predict the only a single value of V_{oc} across all samples. This failing of performance was quite surprising. It was initially considered that the limited range of input V_{oc} values from the raw data might be hindering the ability of the models to learn; however, MinMax normalization should mitigate such discrepancies. Although

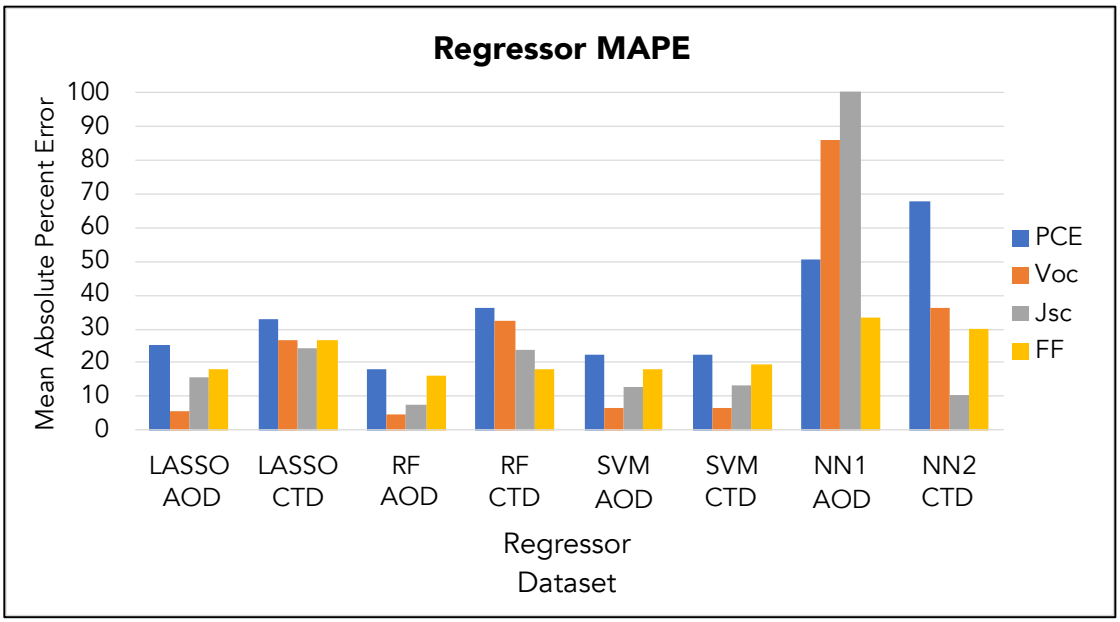

Figure 4.3. MAPE for each model predicting the 4 OPV device metrics, *PCE*, V_{oc}, J_{sc}, and *FF*. Each model was trained on either the AOD or on the CTD.

Figure 4.4. R^2 for each model predicting the 4 OPV device metrics, *PCE*, V_{oc}, J_{sc}, and *FF*. Each model was trained on either the AOD or on the CTD.

our subsequent models mitigate the extent of this discrepancy, V_{oc} was the one of the worst performing predictions. So, in general, models were able to predict J_{sc} and *FF* best of any of the

OPV parameters. This is attributed to the fact that these parameters have been shown to be most affected by morphology and crystallinity. The value of the other parameters relies more heavily on other aspects of the device. For instance, V_{oc} is more a product of molecular energy-level offsets in the HOMO and LUMO of the donor and acceptor materials. In light of these observations, it can be definitively stated that m2py labels and descriptors are extracting salient morphological information. Even when summaries of this morphology descriptors are shown to the models, their accuracy improves.

4.3.3 *Regression on Multidimensional Morphological Data*

Section 4.3.2 shows how including summarized morphology data into regressors can improve their predictive capabilities, even when sample-size is drastically decreased. However, the summarized data consolidates what could be thousands of domains into 2 numbers: the average and standard deviation. This represents a reduction in the information that is being conveyed to the model for training as compared to what is available. In order to fully incorporate morphological information into the predictions of device performance, it is necessary to include image-like data. This can include the m2py labels, the original SPM image, or both. When the models are able to see the domains images, it is expected that the increased density and specificity of information will improve their predictions. To that end, 2-dimensional convolutional neural networks were used to encode image information into the NN models so that predictions on device performance can be made. To inspect the extent to which improvements are seen when including image-like data, label data, and tabular data, model training was done on different combinations of the available datasets

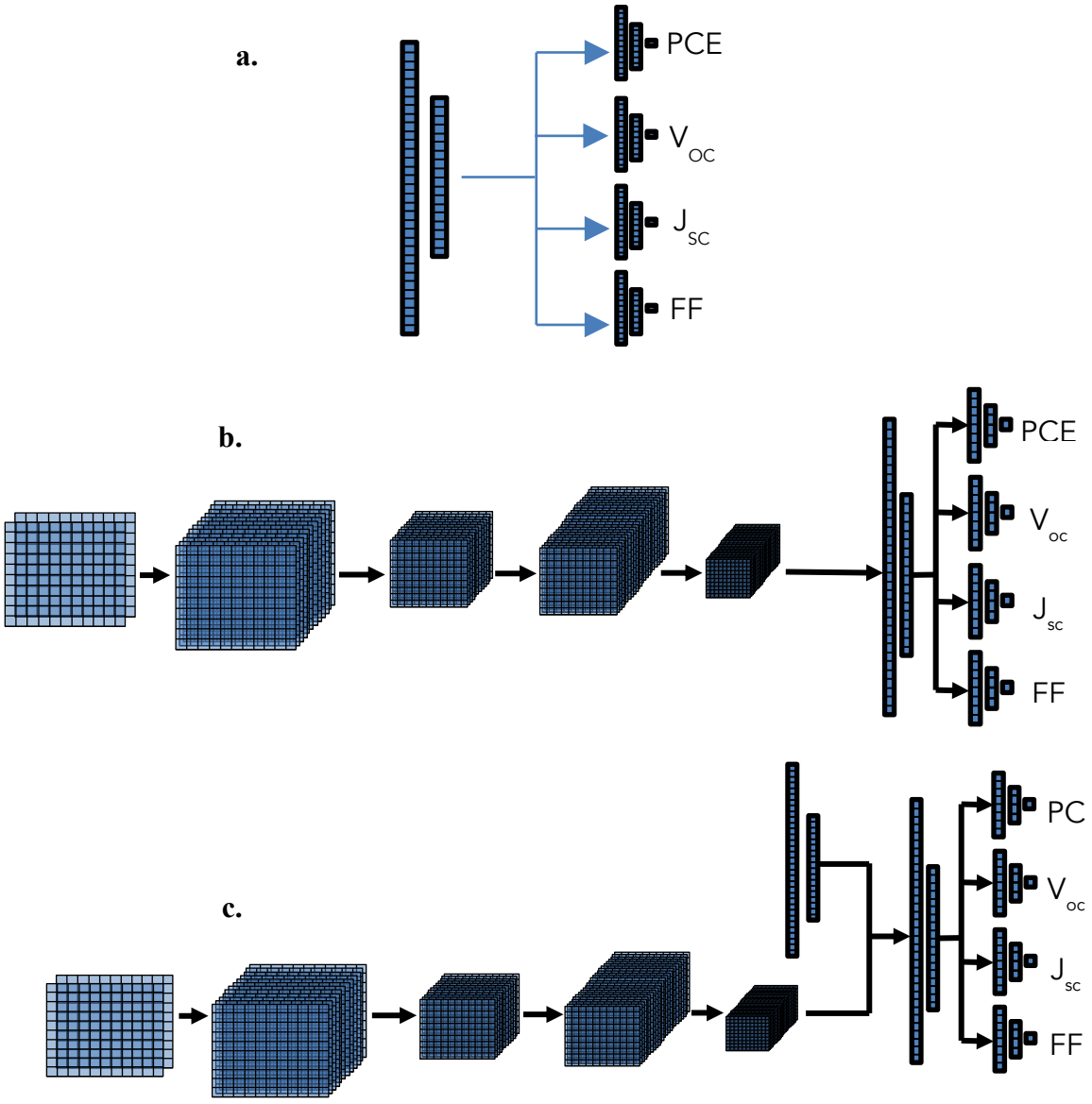

Figure 4.5. a. Network architecture for NN1 and NN2. Only tabular data is taken in and used to make device predictions. **b.** Network architecture for NN3 and NN4. Only image-like data is taken in, encoded, and used to make predictions. These models take in either m2py labels or SPM data and compress the 2-dimensional channels into 1-dimensional tensors before branching. **c.** Network architecture for NN5, NN6, and NN7 is shown. These models take in both tabular and image-like data. The encoded representations of these data are aggregated before the network branches to make its device predictions.

and compared, as described in Table 4.3. In general, it is expected that the models will improve as more image-like data is shown to the model. So, the model that is trained on all of the raw images, the m2py labels, and tabular data will perform the best. Given that m2py labels are distillations of SPM morphological information, including them in training is expected to improve model performance to a similar degree as including the raw images would. Generalized schemes that illustrate the 3 different network architectures explored in this work are shown in Figure 4.5. The NN architecture that is outlined in Figure 4.5a (NN1-2) is a shallow NN that is configured to only take in tabular data to make specialized predictions for the device parameters. Figure 4.5b (NN3-4) illustrates the compression and encoding of image-like data before it is flattened to fully connected linear layers that branch to make predictions on each of the device performance metrics. Finally, Figure 4.5c is an ensemble architecture that takes in both tabular and image-like data. Models using this architecture (NN5 – 7) will have the branches trained either simultaneously or asynchronously. In the simultaneous branch training, similar training protocol to that used for NN1 – 4 is used, where each training sample contains all data needed for the whole network. This is a straightforward method but requires every training sample to have both image and tabular components for the two branches. Strategies for asynchronous model training rely on the fact that the whole network is actually an ensemble of the two previously outlined models. The individual branches can be trained to encode their information and predictions. These model states are then saved and loaded into the ensemble network, which wraps around the two smaller classes and aggregates their encodings before making predictions. This means that the branches can be trained with different datasets, learning rates, epochs and other differences in hyperparameters. This will become useful in work that is outlined in Section 5.1.3-4

Table 4.3. Model name, training set, and progress for the NN predictors outlined in this work.

Architecture	Model	Dataset	Built	OPV Trained	OPV Evaluated
Figure 4.6.a	NN1	Annealing-Conditions Only	X	X	X
	NN2	All Tabular Data	X	X	X
Figure 4.6.b	NN3	m2py Labels Only	X	X	
	NN4	Image Data Only	X		
Figure 4.6.c	NN5	m2py Labels & Tabular Data			
	NN6	Image Data & Tabular Data			
	NN7	All Data			

In order to incorporate m2py labels or SPM images into NN models, the highly dimensional data needs to be encoded into 1D vectors for a final prediction to be made from them. Although there are various methods for encoding image information, only one is explored in the current chapter. Other encoding methods are described in section 5.1.4 for future work. In the current method, the image data is passed through a series of 3, 2-dimesional convolution and pooling layers that receive ReLU activation. The compressed image is vectorized and then passed into a linear layer, which then branches into the same 4 branches as the tabular network to predict device performance. Representative plots of MSE, MAPE, and R^2 extracted during learning rate optimization NN3 to predict annealing conditions are shown in Figure S4.10. As evidenced by the sinusoidal loss graph after epoch ~5 shows that the model is over-fitting to the data. This can be partially alleviated by altering the batch size and learning rate, but even with these modifications the dataset is small and

therefore prone to over-fitting. With a batch size of 26 (the full training set), 5 epochs where enough to reach the first minima in training, where percent error for J_{sc} and *FF* was as low as 15%, and the MAPE for *PCE* and V_{oc} are improved from the models reported in Figures 4.1-3. These are promising preliminary results, again despite the lack of extensive training data. Future work includes optimizing NN3. This includes optimization and improvements from advanced sampling and sub-sampling methods, as well as alternative methods for encoding image-like data, which are discussed in section 5.1.

4.4 CONCLUSIONS

This work shows that the quantitative morphological information that was extracted using m2py is highly correlated with device performance. Particularly for device parameters that are dependent upon crystallinity and long-range order, such as J_{sc} and *FF*, quantitative morphology descriptions can drastically improve the accuracy of predictions of final device performance for OPV devices. Distilling the features of SPM measurements into quantitative morphology labels by using the m2py library developed in chapter 3 enables us to fully integrate morphological data into supervised learning and regression workflows. The ability to extract and encode this information is already shown to drastically improve predictions of device performance as compared to just time and temperature annealing data, and will allow new insights into the morphology of OPV devices. We have shown that morphological data is informative enough to significantly reduce the needed size of training data to make accurate final predictions. Due to the efficacy and open-source nature of all the software used herein, the workflow outlined in these last chapters can be used by researchers to identify desirable morphological features and design streamlined optimization

protocol to emphasize those features. Finally, the tools and processes created and explored in chapters 3 and 4 have been shown to be able to be applied to materials and techniques far beyond the datasets shown here.

4.5 Supporting Information

4.5.1 *OPV Dataset Feature Surfaces*

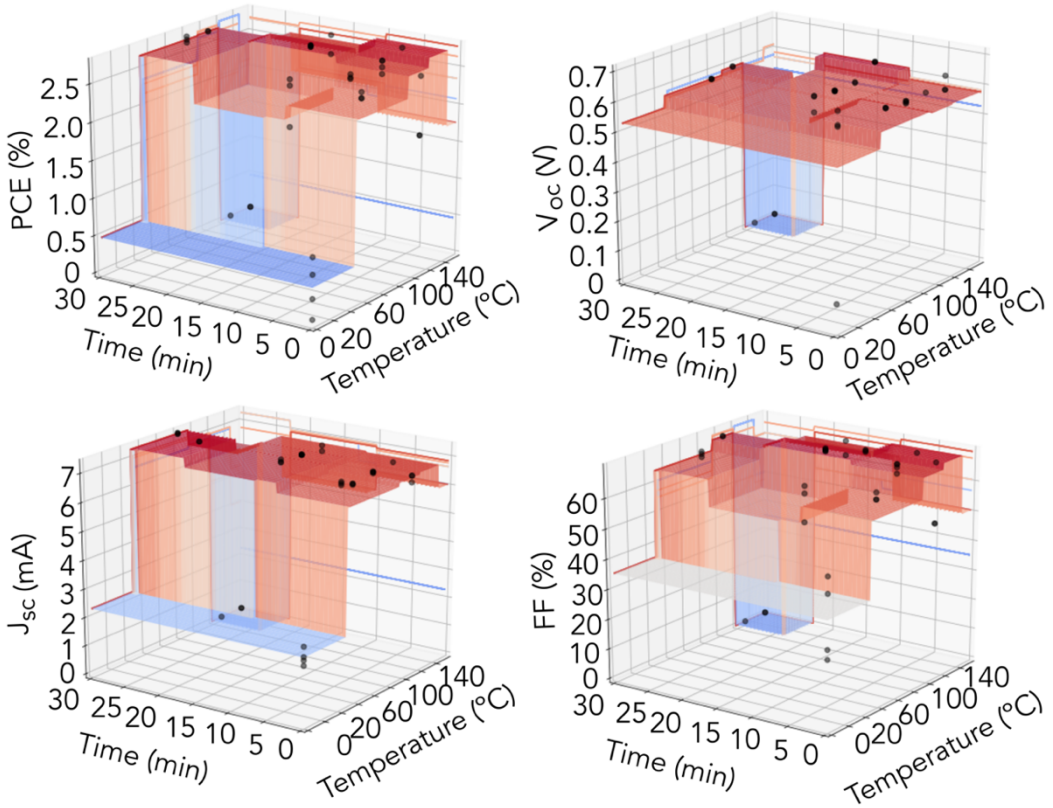

Figure S4.1. Device performance metrics for samples in the OPV dataset that includes morphological information (CTD). 3D surface represents the average value for a given (Time, Temperature) point on the graph. Individual devices are shown as black dots to show variation between samples.

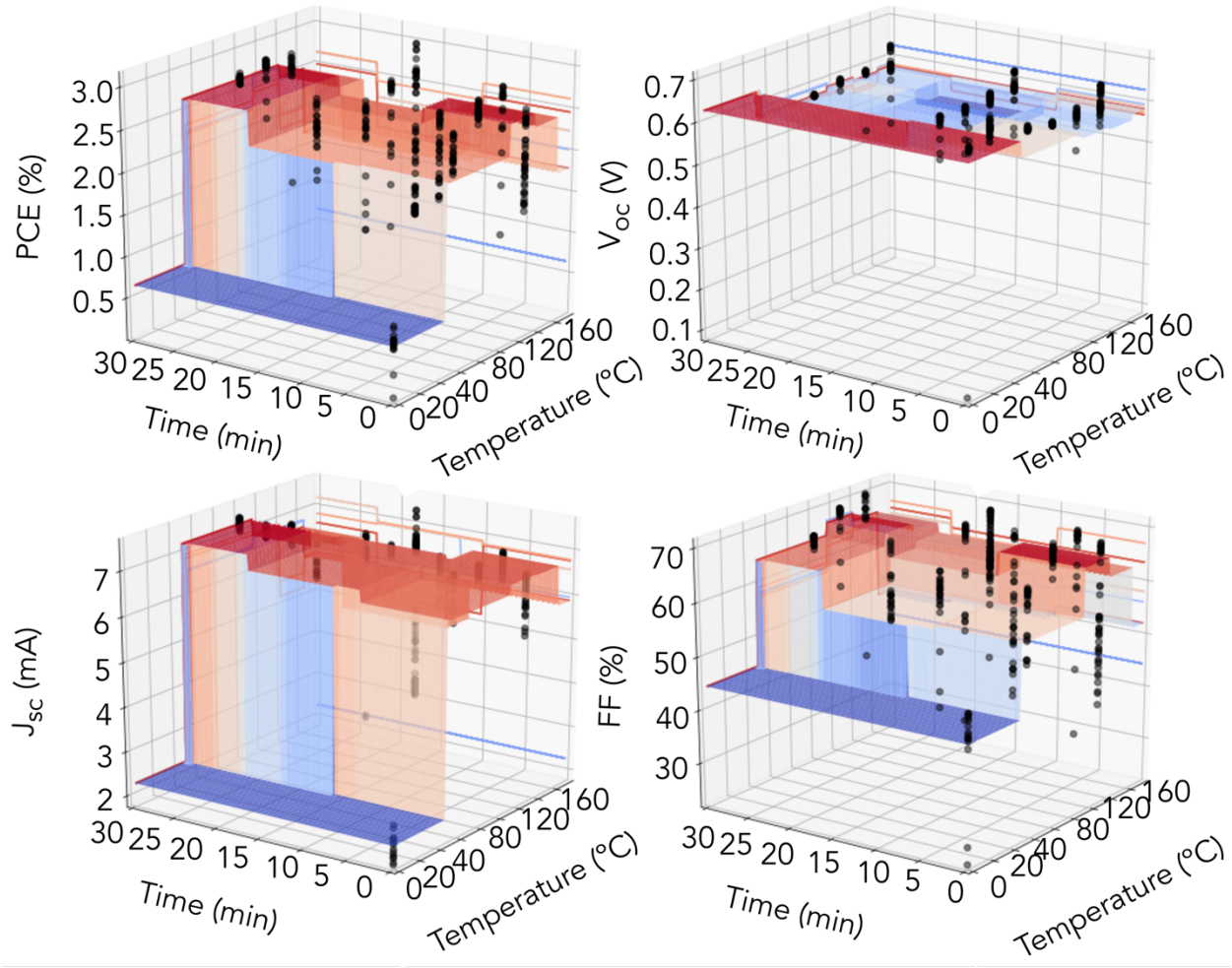

Figure S4.2. Device performance metrics for samples in the OPV dataset that only includes annealing conditions (AOD). 3D surface represents the average value for a given (Time, Temperature) point on the graph. Individual devices are shown as black circles to show variation between samples.

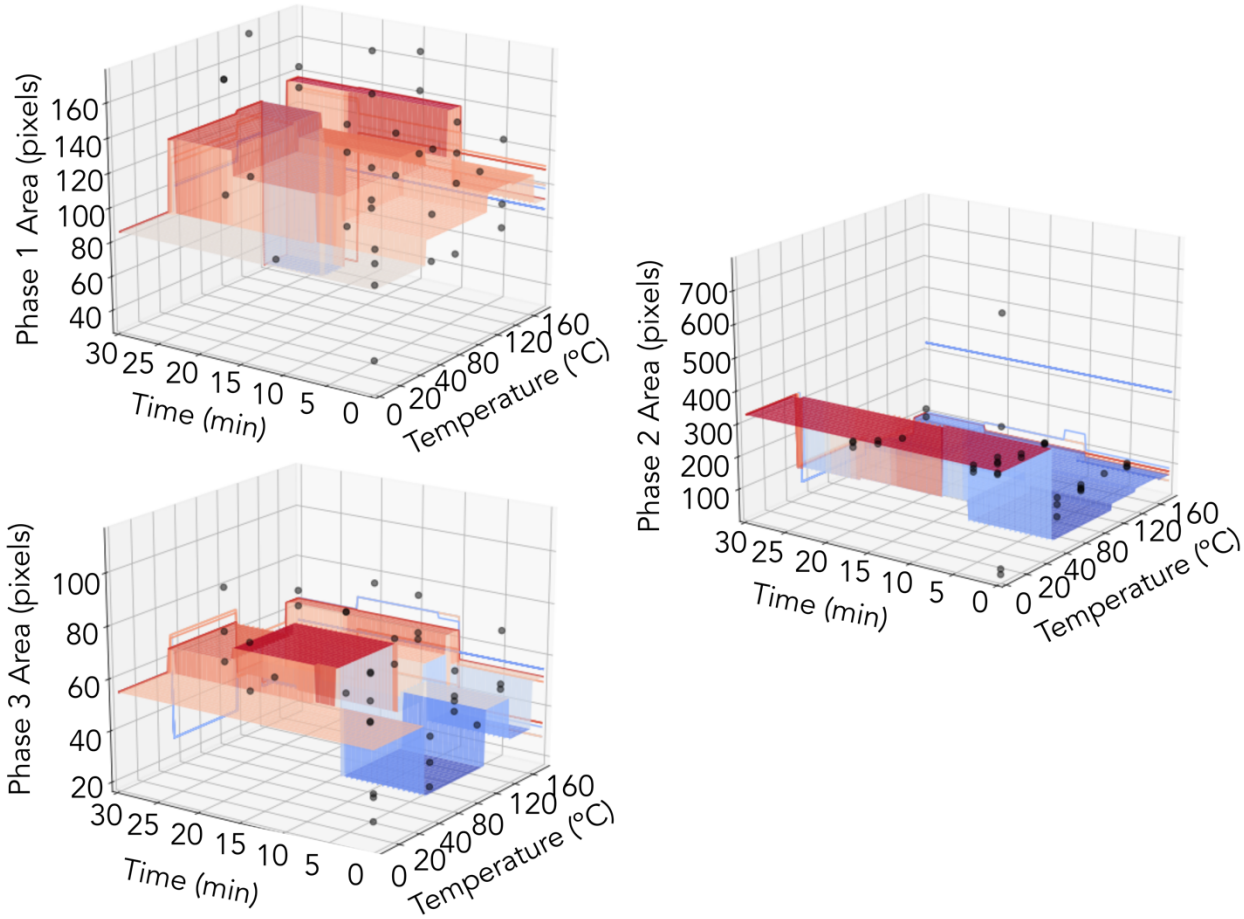

Figure S4.3. Representative morphology descriptors in the OPV dataset that includes morphological information. The active layers were all labeled with 3 phases (fullerene-rich, polymer-rich, and mixed phase, respectively). The 3D surface represents the average area value (in pixels) for a given (Time, Temperature) point on the graph. Individual devices are shown as black circles to show variation between samples.

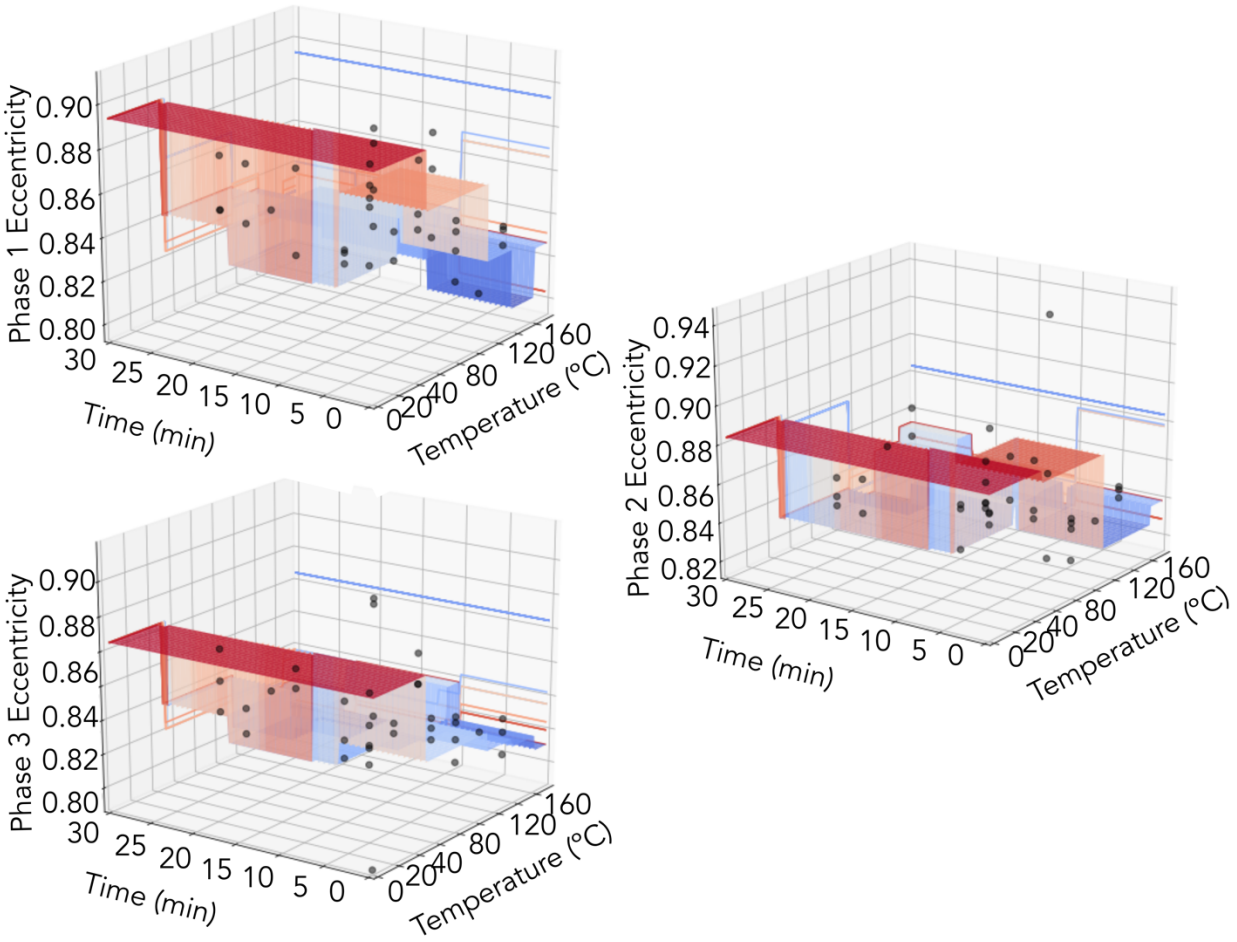

Figure S4.4. Representative morphology descriptors in the OPV dataset that includes morphological information. The active layers were all labeled with 3 phases (fullerene-rich, polymer-rich, and mixed phase, respectively). 3D surface represents the average eccentricity value (unitless) for a given (Time, Temperature) point on the graph. Individual devices are shown as black circles to show variation between samples.

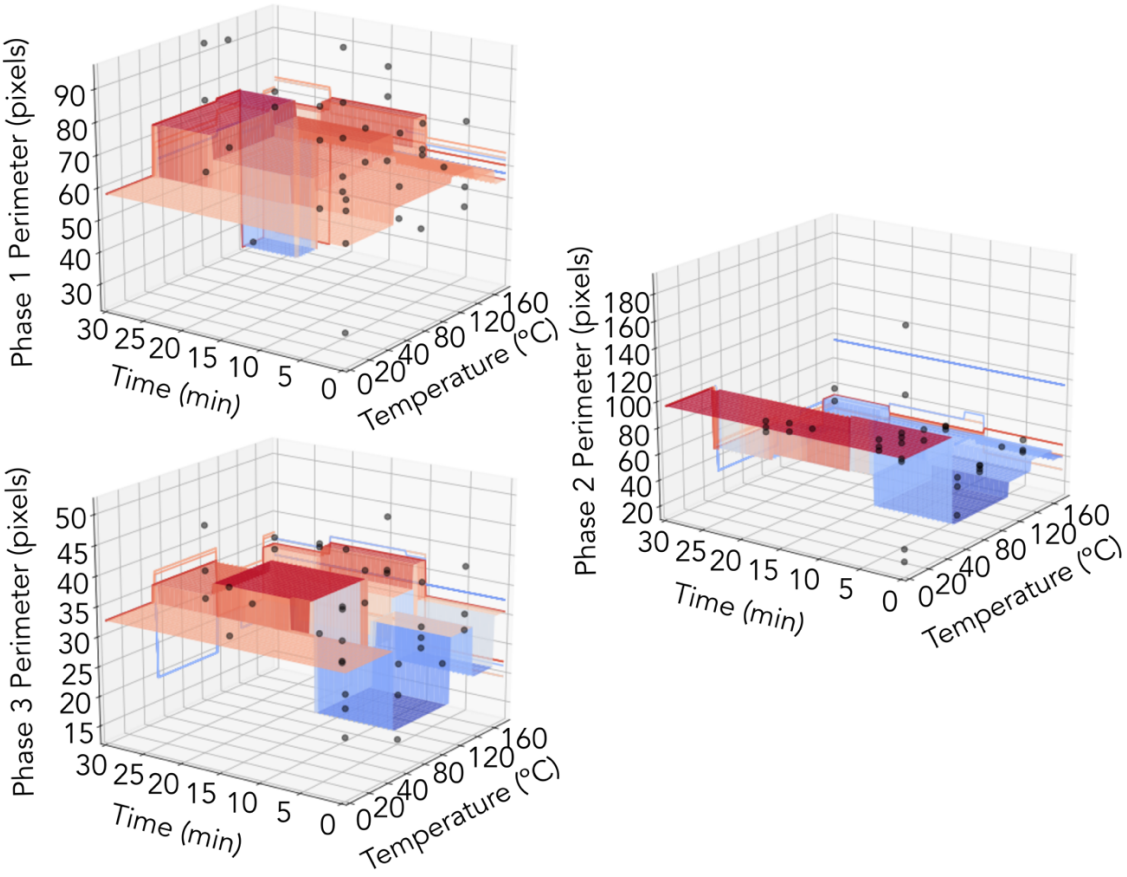

Figure S4.5. Representative morphology descriptors in the OPV dataset that includes morphological information. The active layers were all labeled with 3 phases (fullerene-rich, polymer-rich, and mixed phase, respectively). 3D surface represents the average perimeter length value (in pixels) for a given (Time, Temperature) point on the graph. Individual devices are shown as black circles to show variation between samples.

4.5.2 *Regressor Performance*

The parity plots for each device parameter predicted by each optimized model is shown below for comparison. The top set of four show device performance prediction results from the CTD, while the bottom 4 were produced by regressors trained on the AOD.

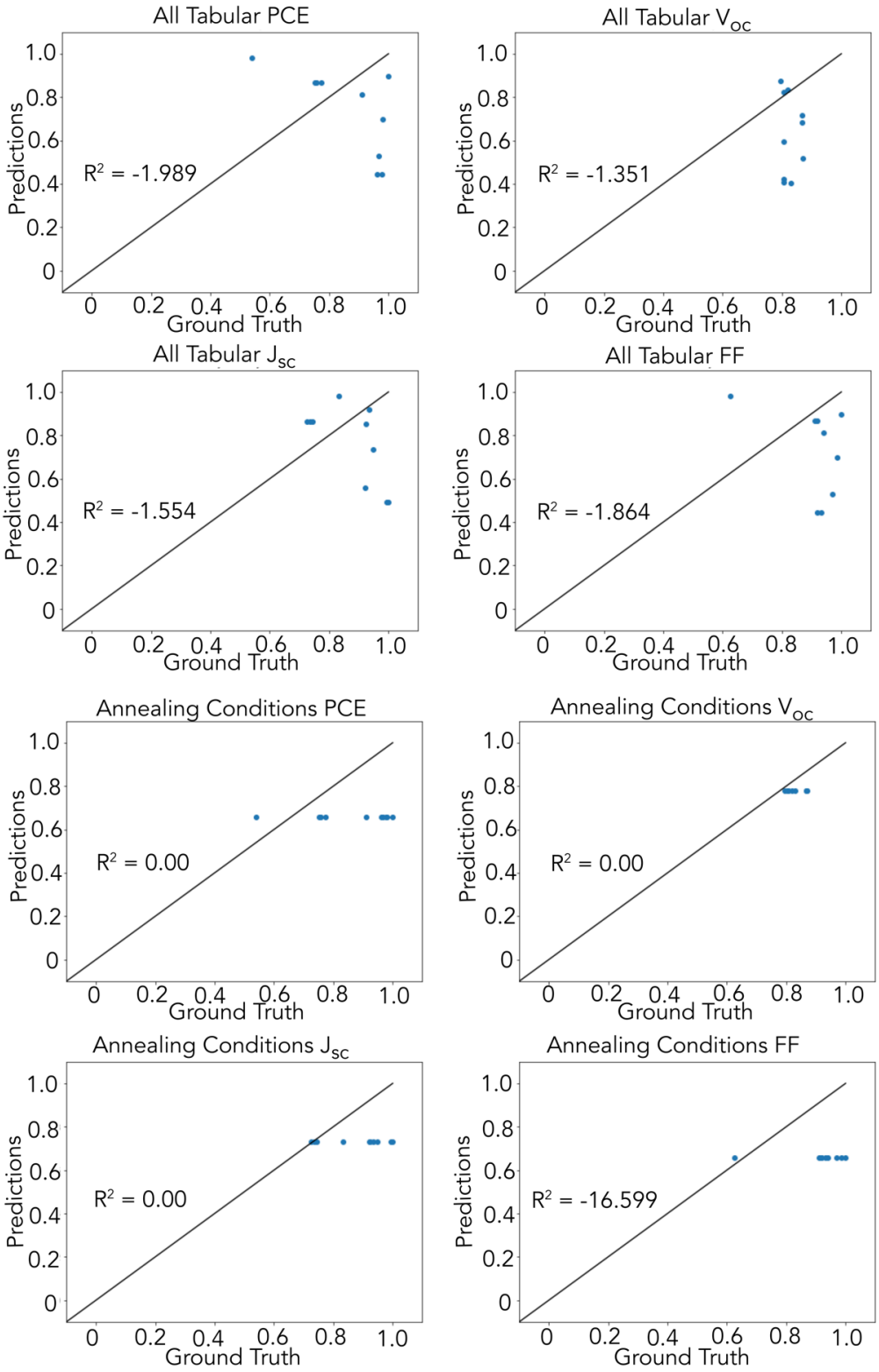

Figure S4.6. R^2 results for LASSO predictions after training on CTD (top 4) and AOD (bottom 4).

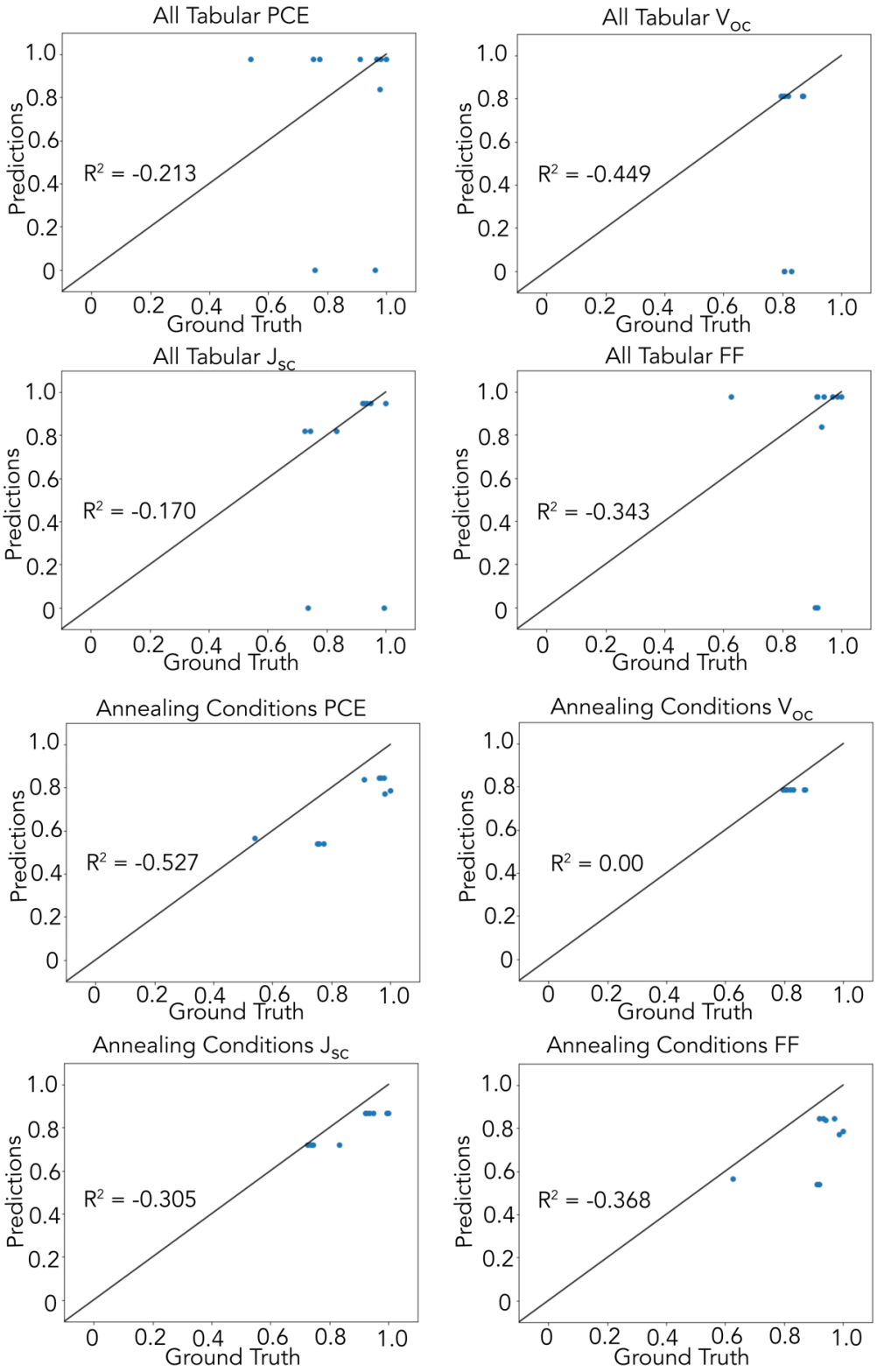

Figure S4.7. R^2 results for RF predictions after training on CTD (top 4) and AOD (bottom 4).

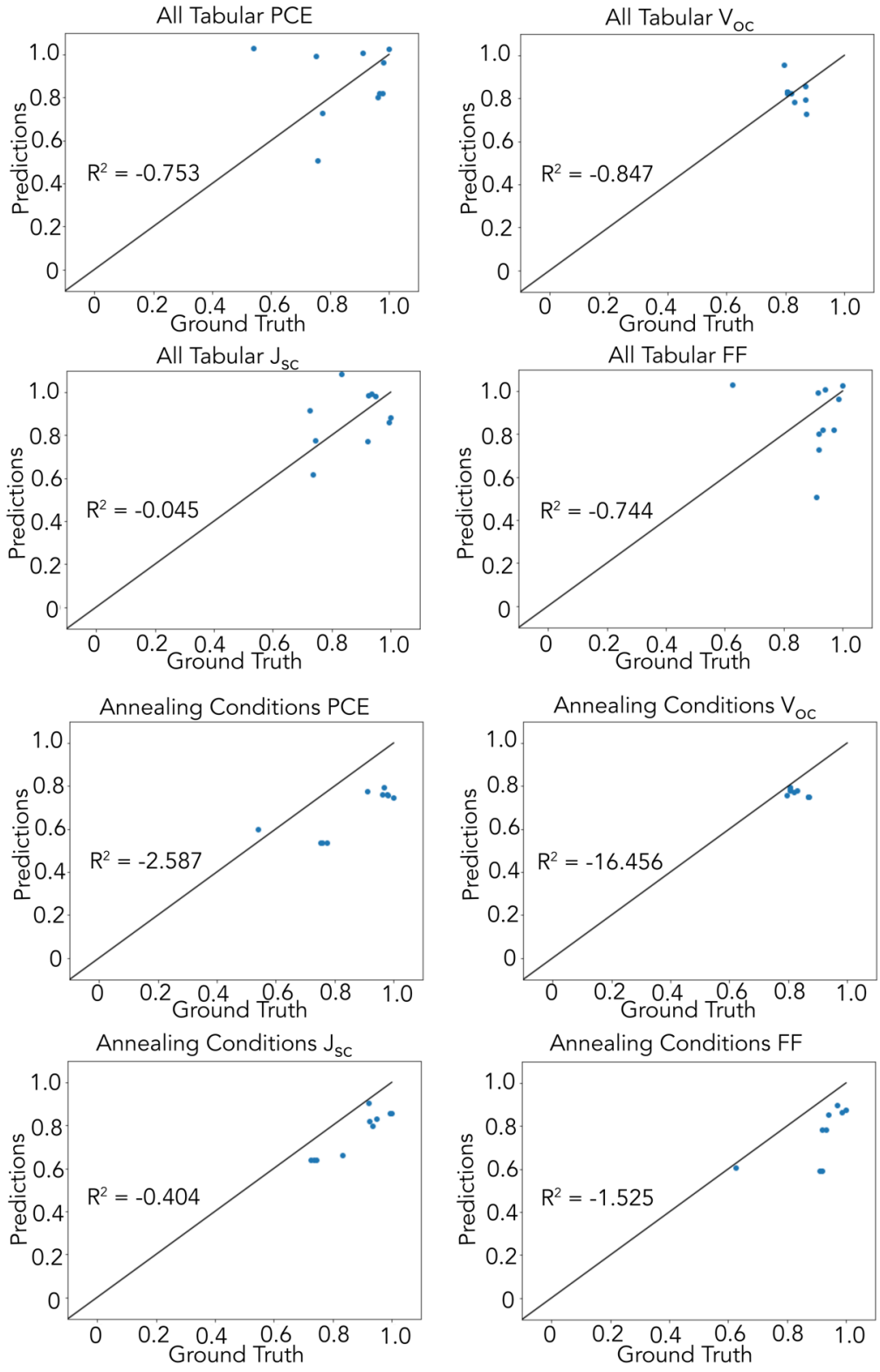

Figure S4.8. R^2 results for SVM predictions after training on CTD (top 4) and AOD (bottom 4).

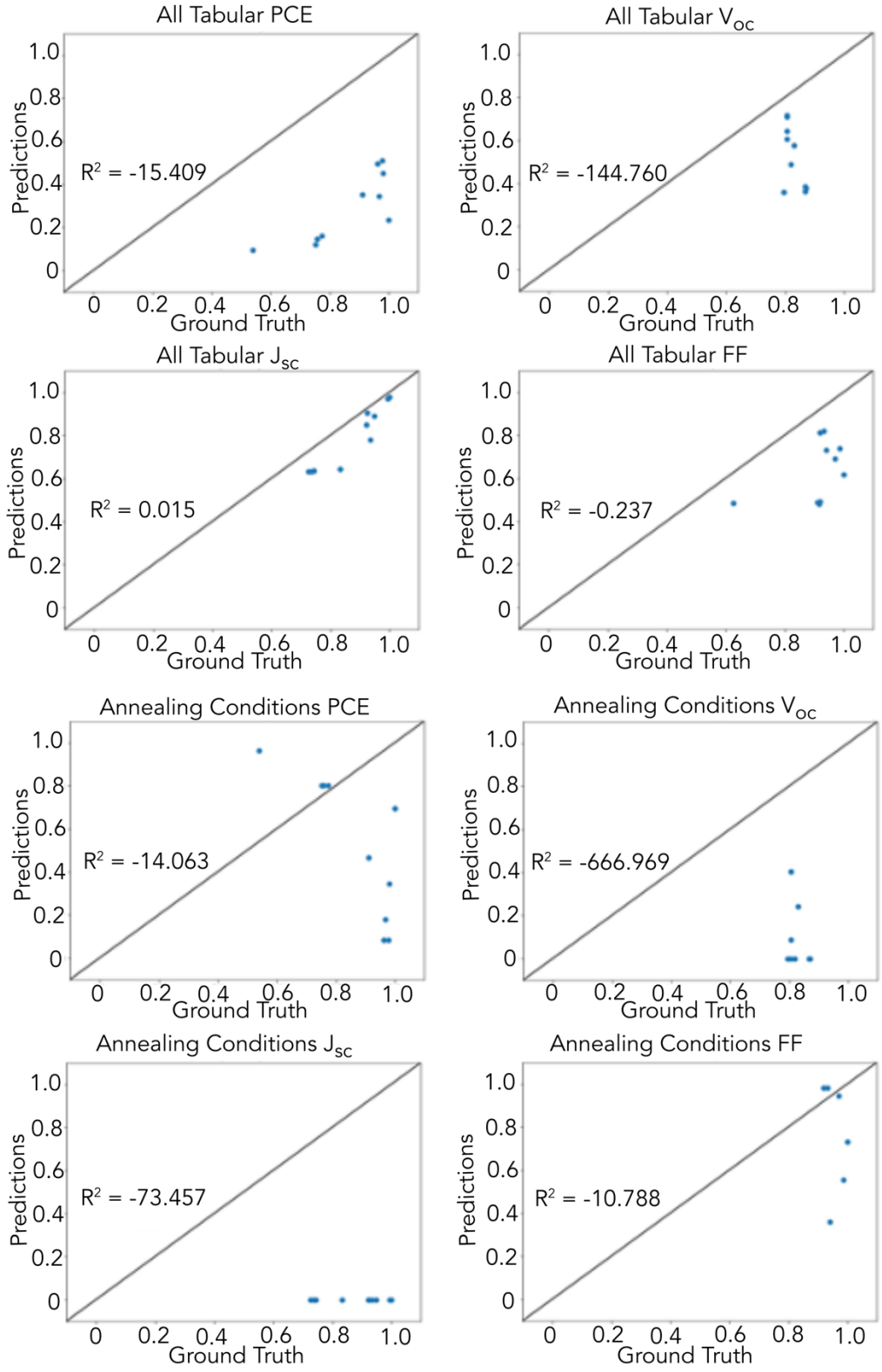

Figure S4.9. R^2 results for NN predictions after training on CTD (top 4, NN2) and AOD (bottom 4, NN1).

4.5.3 *Hyperparameters*

The scikit-learn regressors were optimized using the scikit-learn hyperparameter optimizer, GridSearchCV(), which investigates all permutations of parameters supplied by the user.[149] The parameter dictionary for each regressor is not reported in this dissertation, however they are available for free online at github.com/wesleyktatum/py-conjugated, which contains all code and notebooks used in this chapter. Regressor fitting and optimization notebooks are saved under the directory 'pyconjugated/ipynb/Regression/', where each regressor has its own Jupyter notebook. A table summarizing the hyperparameters of the best performing models is shown below:

Table S4.1. A table summarizing the optimized hyperparameter values for the presented regressors.

Model	Data	Hyperparameter	Best Value (PCE)	Best Value (Voc)	Best Value (Jsc)	Best Value (FF)
LASSO	Annealing Conditions Only	alpha	0.87474963	0.87474963	3.428231494	1.00E-06
		positive	FALSE	FALSE	FALSE	FALSE
		tol	1.00E-05	1.00E-05	1.00E-05	1.00E-05
		max_iter	1000	1000	1000	1000
		selection	random	random	random	random
		random_state	28	28	28	28
	All Tabular	alpha	0.04047757	0.00433785	0.1	0.1
		positive	FALSE	FALSE	FALSE	FALSE
		tol	1.00E-04	1.00E-05	1.00E-04	1.00E-04
		max_iter	1000	1000	1000	1000
		selection	random	random	random	random
		random_state	28	28	28	28
RF	Annealing Conditions Only	ccp_alpha	0	0	0	0
		criterion	mse	mae	mae	mae
		max_depth	27	1	2	5
		max_features	None	None	None	None
		max_leaf_nodes	10	2	4	6
		min_impurity_decrease	0	0	0	0
		min_impurity_split	None	None	None	None
		min_samples_leaf	1	1	1	1
		min_samples_split	3	2	2	2

		min_weight_fraction_leaf	0	0	0	0
		random_state	None	None	None	None
		splitter	best	best	best	best
	All Tabular	**ccp_alpha**	0	0	0	0
		criterion	mae	mse	mae	mse
		max_depth	29	3	30	28
		max_features	None	None	None	None
		max_leaf_nodes	10	17	5	30
		min_impurity_decrease	0	0	0	0
		min_impurity_split	None	None	None	None
		min_samples_leaf	1	1	1	1
		min_samples_split	2	3	3	3
		min_weight_fraction_leaf	0	0	0	0
		random_state	None	None	None	None
		splitter	best	best	best	best
SVM	**Annealing Conditions Only**	**C**	1	0.1	1	0.1
		cache_size	500	500	500	500
		coef0	0.01	0.01	0.146551724	0.590344828
		degree	3	3	3	7
		epsilon	0.1	0.1	0.1	0.1
		gamma	scale	scale	scale	scale
		kernel	poly	poly	poly	poly
		max_iter	-1	-1	-1	-1
		shrinking	TRUE	TRUE	TRUE	TRUE
		tol	0.001	0.001	0.001	0.001
	All Tabular	**C**	1000	0.1	100	1000
		cache_size	500	500	500	500
		coef0	0.698965517	0.1	0.354482759	0.354482759
		degree	8	12	6	8
		epsilon	0.1	0.1	0.1	0.1
		gamma	scale	scale	scale	scale
		kernel	poly	poly	poly	poly
		max_iter	-1	-1	-1	-1
		shrinking	TRUE	TRUE	TRUE	TRUE
		tol	0.001	0.001	0.001	0.001
NN	**Annealing Conditions Only**	**epochs**	11	11	11	11
		learning_rate	0.000095	0.000095	0.000095	0.000095
		optimizer	Adam	Adam	Adam	Adam

		loss_model	Thresholde dMSE	Thresholde dMSE	Thresholded MSE	Thresholded MSE
		batch_size	292	293	294	295
		initialization	Xavier	Xavier	Xavier	Xavier
	All Tabular	**epochs**	40	40	40	40
		learning_rate	0.005	0.005	0.005	0.005
		optimizer	Adam	Adam	Adam	Adam
		loss_model	Thresholde dMSE	Thresholde dMSE	Thresholded MSE	Thresholded MSE
		batch_size	26	26	26	26
		initialization	Xavier	Xavier	Xavier	Xavier
	m2py Labels	**epochs**				
		learning_rate				
		optimizer	Adam	Adam	Adam	Adam
		loss_model				
		batch_size	26	26	26	26
		initialization	Xavier	Xavier	Xavier	Xavier

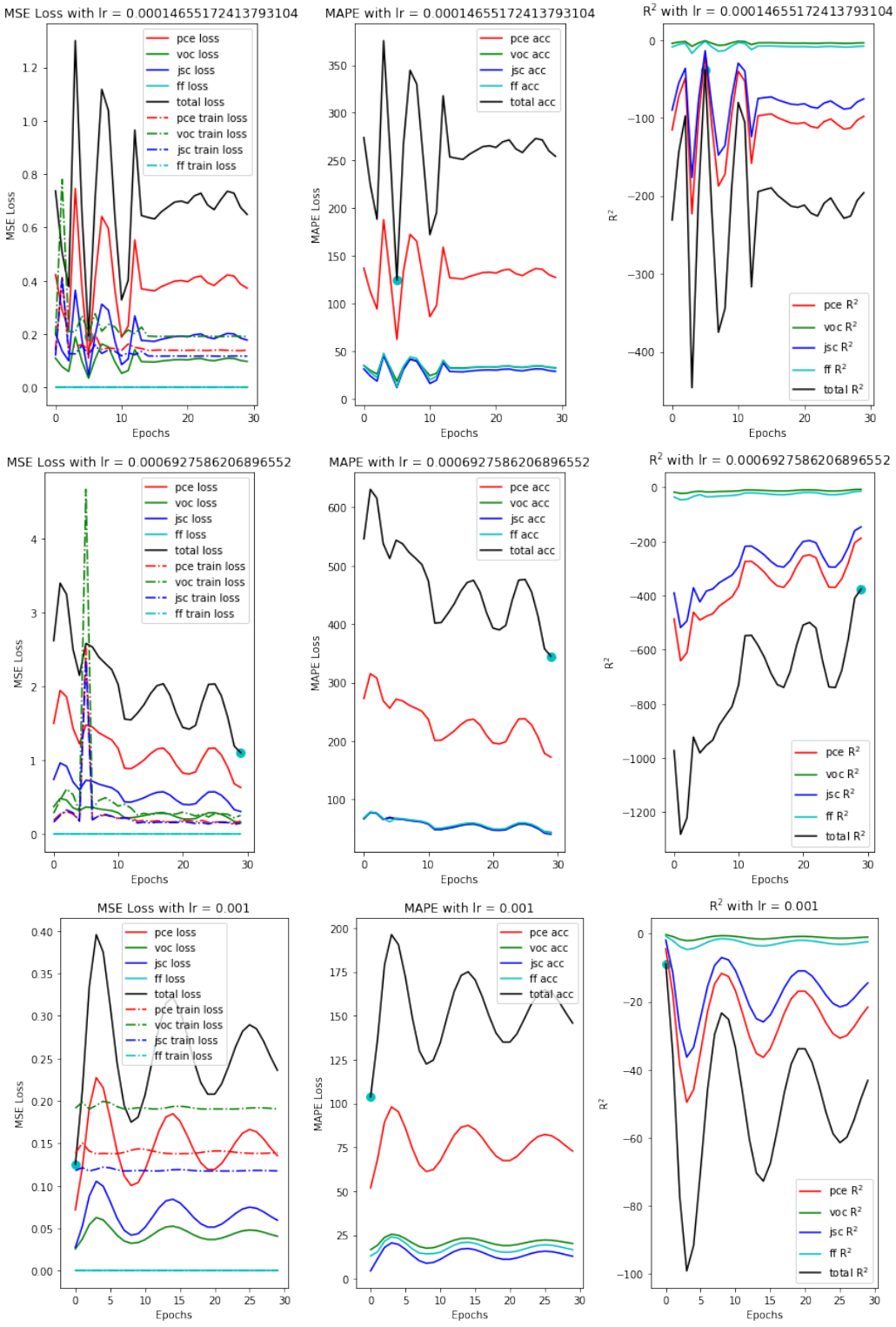

Figure S4.10. Representative results of learning rate optimization of NN3. For each learning rate, the MSE, MAPE, and R^2 are plotted for 30 epochs of training. For each graph, the blue dot corresponds to the epoch with the best value for that metric (*e.g.* lowest loss).

Chapter 5. FUTURE WORK AND CONSIDERATIONS

5.1 Improvements to Models Predicting OFET and OPV Performance

5.1.1 *Finishing the Comparison*

Table 4.3 outlined seven different neural networks, each optimized to a certain combination of OPV data. Future work will finish building and training these models., as well as applying them to the OFET dataset. There are 3 general types of NN explored by Table 4.3: 1) tabular only data (NN1 & NN2), 2) image only data (NN3, NN4), and 3) mixed data (NN5, NN6, NN7). The structures for type 1 and 2 networks have already been created and have structures shown in Figure 4.5a and b. In order to train and test type 3 networks, an ensemble network will be built that loads the pre-trained model states for the two different branches and predicts device parameters based on their output. This is shown graphically in Figure 4.5c.

5.1.2 *Data and Sampling*

As mentioned in the previous chapter, the datasets used in predicting thin film device performance are far smaller than is typically expected of machine learning techniques. One method that could be used to mitigate this is to sub-sample the FDM images and m2py label maps. By dividing the 256 × 256 pixel images into 4 sub-images, the dataset can be artificially increased. Similarly, sampling from the image using a rastering window can turn a single image into hundreds of morphology snapshots for training. Future work will use a 64 × 64 pixel window with a stride length of 1 to increase the 26-image dataset into one containing thousands of images. Sub-sampling

can also allow more images to be included in the training set, since only a small portion of the test-set images need to be reserved for validation.

5.1.3 *Model Optimization*

The sckikit-learn models were all optimized using scikit-learn optimization routines.[149] In addition to narrowing in on the explored hyperparameter-space, using adaptive optimization methods like Bayesian optimization could contribute the finding the optimal performance of these models. Utilizing frameworks like scorch (https://skorch.readthedocs.io/en/stable/) or ray.tune (https://docs.ray.io/en/latest/tune.html) could allow for similarly automated and improved hyperparameter optimization for the NN predictors, as opposed to the custom optimization routines.

5.1.4 *Image Encoding*

Chapter 4 outlines network architectures for encoding tabular and image data to make predictions about device performance. As mentioned, there are various methods specifically for extracting informative features from image-like data. One method was explored in section 4.3, which was convolution and compression to predict annealing conditions. The encodings produced by the layer before the predicting layer are used to describe the images in subsequent device prediction layers. However, there are more methods for extracting salient features from images, 2 of which will be examined. In the first method, the image data is used to train an autoencoder. Autoencoders are a type of neural network that compresses highly dimensional data into a lower-dimensional space. The compressed image-encoding is then expanded back out ("decoded") to the initial image. This

compression-expansion process has two benefits. The first is its efficacy in identifying descriptive features of the image. The second is that the encoding-decoding process does not require labeled features to predict since the goal is to re-create the initial image. For consistency with the image encoding method reported in Section 4.3.3, this autoencoder's compression will be to a 100-element tensor. After training the whole autoencoder, the first half of the model, the component that encodes, can then be used to encode new images into highly informative vectors. Similar to method 1, these informative morphology vectors are then used in the prediction of final device performance. The second type of image encoder to be explored is a variant of autoencoders called "self-learning". In this method, the goal is still to decode the compressed information to a clean version of the original data. However, in this method the input image is distorted in some way, prior to inputting the data into the model. This distortion can be blurring, transforming, rotating, or other ways of adding noise to the original image. By forcing the model to produce the original data by removing the applied distortions, it can more effectively identify descriptive features of the original image when it moves on to new data. As with the other image encoders, the first half that compresses the image will be used to extract predictive information in the image before using the encoded image to make predictions on final performance. It is expected that this final method will produce the most informative image encoding and will contribute to the most accurate predictions of device performance. Finally, the added advantage of using autoencoding of images is that morphology images with no final device performance can still be used train the image encoder. This will build off of the data sampling methods outlined in section 5.1.2.

5.2 Rectifying Kinetic Monte Carlo Simulations to Experimental Results

Simulation methods such as Density Functional Theory (DFT) and Molecular Dynamics (MD) have proved to be a valuable tool in the development of a molecular-scale understanding of CP.[177–184] By utilizing the governing equations of atomic interactions, researchers have reproduced experimental results to a high degree. Kinetic Monte Carlo (KMC) has been applied to CP:fullerene systems to investigate charge generation and transport as a result of the molecular distribution, or morphology. To do so, 10 tessellated 10 nm^3 cubes are generated, allowing *J-V* characteristics of the simulated active layer to be calculated.[177] In order to continue to improve these methods, it is important to continue to experimentally validate them as precisely as possible. However, experimental validation at this small of a size-scale is difficult at best with current instrumentation. Although lab-scale devices are smaller than commercial products, they are still on the order of 0.01 mm^3, far larger than the simulated devices. In order to precisely validate the veracity of the simulated morphologies, novel solutions are required.

The techniques outlined in section 3.3 and 3.4 enable just such an analysis and validation. We are currently working to fabricate consistent OPV cells from P3HT:$PCB_{60}M$ blends. Once consistency is achieved, OPV devices that are annealed for different times at different temperatures, similar to section 4.1, will be fabricated. This is expected to produce a variety of morphologies as the phases begin to separate and aggregate as a result of the thermal annealing. This array of devices will also allow the thorough investigation of domain size and distribution on the performance of P3HT:fullerene OPV devices. Once made, these OPV devices will be classified by their morphologies using the developed method and maps of domains and phases will be generated. Crucially, these morphology maps are spatially resolved on the order of 10 nm,

corresponding to the diameter of the probe tip, which is on the same order as KMC simulations generated by collaborators at Boise State University. This will allow for a quantitative comparison of experimental and simulated OPV morphologies and *J-V* characteristics that can be used to further improve KMC methods.

5.3 High Performance π-Conjugated Polymer Morphologies and Performance

Developing a detailed understanding of CP thin film morphology is of the upmost importance to continue the improvements the field has seen throughout the past years. As discussed above, CP can fall into one of three different morphological category types – semicrystalline, disordered aggregates, and completely amorphous, with some of the highest performing polymers, such as PIDTBTD, falling into the disordered aggregate category. It is reasonable to assume that these different morphological categories will behave differently throughout different film deposition procedures react differently to other processing parameters. Although investigations using traditional methods, like DSC and GIWAXS have elucidated much of these differences, it has so far been difficult to understand these materials on the length-scale of their crystalline domains, which is ~10 nm. The work in chapters 3 and 4 outline methods capable of examining materials on this length scale and quantitatively mapping their morphology with just such spatial resolution. As such, experiments to optimize and understand these thin film morphologies should seek to use m2py to label and identify these differences. To that end, the morphologies of P3HT (semicrystalline morphology) and another CP of interest, PIDTBTD (disordered aggregate morphology), that result from isotropic deposition (e.g. spin coating) and anisotropic, sheer aligning deposition (e.g. blade coating) will be investigated. The morphological progression as a

result of post-processing thermal annealing will serve to underscore the differences in the two polymers. The optoelectronic and charge transport properties for each reaction condition will be investigated by UV-vis and OFET fabrication, respectively.

Chapter 6. REFERENCES

(1) Roth, B.; Savagatrup, S.; V. de los Santos, N.; Hagemann, O.; Carlé, J. E.; Helgesen, M.; Livi, F.; Bundgaard, E.; Søndergaard, R. R.; Krebs, F. C.; et al. Mechanical Properties of a Library of Low-Band-Gap Polymers. *Chem. Mater.* **2016**, *28* (7), 2363–2373.

(2) Chortos, A.; Liu, J.; Bao, Z. Pursuing Prosthetic Electronic Skin. *Nat. Mater.* **2016**, *15* (9), 937–950.

(3) Kim, H.-J.; Thukral, A.; Sharma, S.; Yu, C. Biaxially Stretchable Fully Elastic Transistors Based on Rubbery Semiconductor Nanocomposites. *Adv. Mater. Technol.* **2018**, *3* (6), 1800043.

(4) Choi, D.; Kim, H.; Persson, N.; Chu, P.-H.; Chang, M.; Kang, J.-H.; Graham, S.; Reichmanis, E. Elastomer–Polymer Semiconductor Blends for High-Performance Stretchable Charge Transport Networks. *Chem. Mater.* **2016**, *28* (4), 1196–1204.

(5) Zhang, Y.; Fu, H.; Su, Y.; Xu, S.; Cheng, H.; Fan, J. A.; Hwang, K.-C.; Rogers, J. A.; Huang, Y. Mechanics of Ultra-Stretchable Self-Similar Serpentine Interconnects. *Acta Mater.* **2013**, *61* (20), 7816–7827.

(6) Kim, D.-H.; Xiao, J.; Song, J.; Huang, Y.; Rogers, J. A. Stretchable, Curvilinear Electronics Based on Inorganic Materials. *Adv. Mater.* **2010**, *22* (19), 2108–2124.

(7) Song, Z.; Wang, X.; Lv, C.; An, Y.; Liang, M.; Ma, T.; He, D.; Zheng, Y.-J.; Huang, S.-Q.; Yu, H.; et al. Kirigami-Based Stretchable Lithium-Ion Batteries. *Sci. Rep.* **2015**, *5* (1), 10988.

(8) Rogers, J. A.; Someya, T.; Huang, Y. Materials and Mechanics for Stretchable Electronics. *Science* **2010**, *327* (5973), 1603–1607.

(9) Won Mook Choi, †; Jizhou Song, ‡; Dahl-Young Khang, †; Hanqing Jiang, §; Yonggang Y. Huang, ‡ and; John A. Rogers*, †. Biaxially Stretchable "Wavy" Silicon Nanomembranes. **2007**, *7* (6), 1655–1663.

(10) Song, J.; Huang, Y.; Xiao, J.; Wang, S.; Hwang, K. C.; Ko, H. C.; Kim, D.-H.; Stoykovich, M. P.; Rogers, J. A. Mechanics of Noncoplanar Mesh Design for Stretchable Electronic Circuits. *J. Appl. Phys.* **2009**, *105* (12), 123516.

(11) Wang, Y.; Gong, S.; Wang, S. J.; Yang, X.; Ling, Y.; Yap, L. W.; Dong, D.; Simon, G. P.; Cheng, W. Standing Enokitake-like Nanowire Films for Highly Stretchable Elastronics. *ACS Nano* **2018**, acsnano.8b05019.

(12) Guo, Y.; Guo, Z.; Zhong, M.; Wan, P.; Zhang, W.; Zhang, L. A Flexible Wearable Pressure Sensor with Bioinspired Microcrack and Interlocking for Full-Range Human-Machine Interfacing. *Small* **2018**, 1803018.

(13) Chiang, C. K.; Fincher, C. R.; Park, Y. W.; Heeger, A. J.; Shirakawa, H.; Louis, E. J.; Gau, S. C.; MacDiarmid, A. G. Electrical Conductivity in Doped Polyacetylene. *Phys. Rev. Lett.* **1977**, *39* (17), 1098–1101.

(14) Lin, Y.; Firdaus, Y.; Nugraha, M. I.; Liu, F.; Karuthedath, S.; Emwas, A.; Zhang, W.; Seitkhan, A.; Neophytou, M.; Faber, H.; et al. 17.1% Efficient Single-Junction Organic Solar Cells Enabled by N-Type Doping of the Bulk-Heterojunction. *Adv. Sci.* **2020**, *7* (7), 1903419.

(15) Luo, C.; Kyaw, A. K. K.; Perez, L. A.; Patel, S.; Wang, M.; Grimm, B.; Bazan, G. C.; Kramer, E. J.; Heeger, A. J. General Strategy for Self-Assembly of Highly Oriented Nanocrystalline Semiconducting Polymers with High Mobility. *Nano Lett.* **2014**, *14* (5),

2764–2771.
(16) Mun, S.; Park, Y.; Lee, Y.-E. K.; Sung, M. M. Highly Sensitive Ammonia Gas Sensor Based on Single-Crystal Poly(3-Hexylthiophene) (P3HT) Organic Field Effect Transistor. *Langmuir* **2017**, *33* (47), 13554–13560.
(17) Han, J.; Yang, D.; Wang, Y.; Ma, D.; Qiao, W.; Wang, Z. Y. Low-LUMO Acceptor Polymers for High-Gain All-Polymer Photodiodes. *J. Mater. Chem. C* **2018**.
(18) Hiura, S.; Okada, N.; Wakui, J.; Narita, H.; Kanehashi, S.; Shimomura, T. Thermoelectric Properties of Poly(3-Hexylthiophene) Nanofiber Mat with a Large Void Fraction. *Materials (Basel).* **2017**, *10* (5), 468.
(19) Untilova, V.; Biskup, T.; Biniek, L.; Vijayakumar, V.; Brinkmann, M. Control of Chain Alignment and Crystallization Helps Enhance Charge Conductivities and Thermoelectric Power Factors in Sequentially Doped P3HT:F4TCNQ Films. *Macromolecules* **2020**, *53* (7), 2441–2453.
(20) Ding, X.; Liu, J.; Harris, T. A. L. A Review of the Operating Limits in Slot Die Coating Processes. *AIChE J.* **2016**, *62* (7), 2508–2524.
(21) Gu, X.; Zhou, Y.; Gu, K.; Kurosawa, T.; Guo, Y.; Li, Y.; Lin, H.; Schroeder, B. C.; Yan, H. H.; Molina-Lopez, F.; et al. Roll-to-Roll Printed Large-Area All-Polymer Solar Cells with 5% Efficiency Based on a Low Crystallinity Conjugated Polymer Blend. *Adv. Energy Mater.* **2017**, *7* (14), 1602742.
(22) Renewable Energy Agency, I. *RENEWABLE ENERGY TECHNOLOGIES: COST ANALYSIS SERIES*; 2012.
(23) Gburek, B.; Wagner, V. Influence of the Semiconductor Thickness on the Charge Carrier Mobility in P3HT Organic Field-Effect Transistors in Top-Gate Architecture on Flexible Substrates. *Org. Electron.* **2010**, *11* (5), 814–819.
(24) Min Nam, Y.; Huh, J.; Ho Jo, W. Optimization of Thickness and Morphology of Active Layer for High Performance of Bulk-Heterojunction Organic Solar Cells. *Sol. Energy Mater. Sol. Cells* **2010**, *94* (6), 1118–1124.
(25) Kaltenbrunner, M.; White, M. S.; Głowacki, E. D.; Sekitani, T.; Someya, T.; Sariciftci, N. S.; Bauer, S. Ultrathin and Lightweight Organic Solar Cells with High Flexibility. *Nat. Commun.* **2012**, *3* (1), 770.
(26) Song, E.; Kang, B.; Choi, H. H.; Sin, D. H.; Lee, H.; Lee, W. H.; Cho, K. Stretchable and Transparent Organic Semiconducting Thin Film with Conjugated Polymer Nanowires Embedded in an Elastomeric Matrix. *Adv. Electron. Mater.* **2016**, *2* (1), 1500250.
(27) Xu, J.; Wang, S.; Wang, G.-J. N.; Zhu, C.; Luo, S.; Jin, L.; Gu, X.; Chen, S.; Feig, V. R.; To, J. W. F.; et al. Highly Stretchable Polymer Semiconductor Films through the Nanoconfinement Effect. *Science* **2017**, *355* (6320), 59–64.
(28) Nunzi, J.-M. Organic Photovoltaic Materials and Devices. *Comptes Rendus Phys.* **2002**, *3* (4), 523–542.
(29) Sariciftci, N. S.; Milowitz, L.; Heeger, A. J.; Wudl, F. Photoinduced Electron Transfer from a Conducting Polymer to Buckminsterfullerene. *Science (80-.).* **1992**, *258* (5–87), 1474–1476.
(30) Pron, A.; Rannou, P. Processible Conjugated Polymers: From Organic Semiconductors to Organic Metals and Superconductors. *Prog. Polym. Sci.* **2002**, *27* (1), 135–190.
(31) Ajayaghosh, A. Donor–Acceptor Type Low Band Gap Polymers: Polysquaraines and Related Systems. *Chem. Soc. Rev.* **2003**, *32* (4), 181–191.
(32) Spano, F. C.; Silva, C. H- and J-Aggregate Behavior in Polymeric Semiconductors. *Annu.*

Rev. Phys. Chem. **2014**, *65* (1), 477–500.
(33) Yamagata, H.; Spano, F. C. Interplay between Intrachain and Interchain Interactions in Semiconducting Polymer Assemblies: The HJ-Aggregate Model. *J. Chem. Phys.* **2012**, *136* (18), 184901.
(34) Hestand, N. J.; Spano, F. C. Expanded Theory of H- and J-Molecular Aggregates: The Effects of Vibronic Coupling and Intermolecular Charge Transfer. *Chem. Rev.* **2018**, *118* (15), 7069–7163.
(35) Baghgar, M.; Labastide, J. A.; Bokel, F.; Hayward, R. C.; Barnes, M. D. Effect of Polymer Chain Folding on the Transition from H- to J-Aggregate Behavior in P3HT Nanofibers. *J. Phys. Chem. C* **2014**, *118* (4), 2229–2235.
(36) Hosemann, R. Crystalline and Paracrystalline Order in High Polymers. *J. Appl. Phys.* **1963**, *34* (1), 25–41.
(37) Koch, F. P. V.; Rivnay, J.; Foster, S.; Müller, C.; Downing, J. M.; Buchaca-Domingo, E.; Westacott, P.; Yu, L.; Yuan, M.; Baklar, M.; et al. The Impact of Molecular Weight on Microstructure and Charge Transport in Semicrystalline Polymer Semiconductors–Poly(3-Hexylthiophene), a Model Study. *Prog. Polym. Sci.* **2013**, *38* (12), 1978–1989.
(38) Snyder, C. R.; Nieuwendaal, R. C.; DeLongchamp, D. M.; Luscombe, C. K.; Sista, P.; Boyd, S. D. Quantifying Crystallinity in High Molar Mass Poly(3-Hexylthiophene). *Macromolecules* **2014**, *47* (12), 3942–3950.
(39) Koch, F. P. V.; Heeney, M.; Smith, P. Thermal and Structural Characteristics of Oligo(3-Hexylthiophene)s (3HT) $_n$, n = 4–36. *J. Am. Chem. Soc.* **2013**, *135* (37), 13699–13709.
(40) Mazzio, K. A.; Rice, A. H.; Durban, M. M.; Luscombe, C. K. Effect of Regioregularity on Charge Transport and Structural and Excitonic Coherence in Poly(3-Hexylthiophene) Nanowires. *J. Phys. Chem. C* **2015**, *119* (27), 14911–14918.
(41) Baghgar, M.; Labastide, J.; Bokel, F.; Dujovne, I.; Mckenna, A.; Barnes, A. M.; Pentzer, E.; Emrick, T.; Hayward, R.; Barnes, M. D. Probing Inter-and Intrachain Exciton Coupling in Isolated Poly(3- Hexylthiophene) Nanofibers: Effect of Solvation and Regioregularity. *J. Phys. Chem. Lett* **2012**, *3*, 1674–1679.
(42) Shimomura, T.; Takahashi, T.; Ichimura, Y.; Nakagawa, S.; Noguchi, K.; Heike, S.; Hashizume, T. Relationship between Structural Coherence and Intrinsic Carrier Transport in an Isolated Poly(3-Hexylthiophene) Nanofiber. *Phys. Rev. B* **2011**, *83* (11), 115314.
(43) Li, Y.; Tatum, W. K.; Onorato, J. W.; Barajas, S. D.; Yang, Y. Y.; Luscombe, C. K. An Indacenodithiophene-Based Semiconducting Polymer with High Ductility for Stretchable Organic Electronics. *Polym. Chem.* **2017**, *8* (34), 5185–5193.
(44) Li, Y.; Tatum, W. K.; Onorato, J. W.; Zhang, Y.; Luscombe, C. K. Low Elastic Modulus and High Charge Mobility of Low-Crystallinity Indacenodithiophene-Based Semiconducting Polymers for Potential Applications in Stretchable Electronics. *Macromolecules* **2018**, *51* (16), 6352–6358.
(45) Persson, N.; McBride, M.; Grover, M.; Reichmanis, E. Silicon Valley Meets the Ivory Tower: Searchable Data Repositories for Experimental Nanomaterials Research. *Curr. Opin. Solid State Mater. Sci.* **2016**, *20* (6), 338–343.
(46) Holliday, S.; Donaghey, J. E.; McCulloch, I. Advances in Charge Carrier Mobilities of Semiconducting Polymers Used in Organic Transistors. *Chem. Mater.* **2014**, *26* (1), 647–663.
(47) Wang, G.; Swensen, J.; Moses, D.; Heeger, A. J. Increased Mobility from Regioregular Poly(3-Hexylthiophene) Field-Effect Transistors. *Cit. J. Appl. Phys.* **2003**, *93*

(hexylthiophene), 195.
(48) DeLongchamp, D. M.; Kline, R. J.; Jung, Y.; Germack, D. S.; Lin, E. K.; Moad, A. J.; Richter, L. J.; Toney, M. F.; Heeney, M.; McCulloch, I. Controlling the Orientation of Terraced Nanoscale "Ribbons" of a Poly(Thiophene) Semiconductor. *ACS Nano* **2009**, *3* (4), 780–787.
(49) Chen, L.; Chi, S.; Zhao, K.; Liu, J.; Yu, X.; Han, Y. Aligned Films of the DPP-Based Conjugated Polymer by Solvent Vapor Enhanced Drop Casting. *Polymer (Guildf).* **2016**, *104*, 123–129.
(50) Choi, D.; Chang, M.; Reichmanis, E. Controlled Assembly of Poly(3-Hexylthiophene): Managing the Disorder to Order Transition on the Nano- through Meso-Scales. *Adv. Funct. Mater.* **2015**, *25* (6), 920–927.
(51) Aiyar, A. R.; Hong, J.-I.; Izumi, J.; Choi, D.; Kleinhenz, N.; Reichmanis, E. Ultrasound-Induced Ordering in Poly(3-Hexylthiophene): Role of Molecular and Process Parameters on Morphology and Charge Transport. *ACS Appl. Mater. Interfaces* **2013**, *5* (7), 2368–2377.
(52) Wang, G.; Persson, N.; Chu, P.-H.; Kleinhenz, N.; Fu, B.; Chang, M.; Deb, N.; Mao, Y.; Wang, H.; Grover, M. A.; et al. Microfluidic Crystal Engineering of π-Conjugated Polymers. *ACS Nano* **2015**, *9* (8), 8220–8230.
(53) Chen, C.; Liu, D.; Wu, Y.; Bi, W.; Sun, X.; Chen, X.; Liu, W.; Xu, L.; Song, H.; Dai, Q. Dual Interfacial Modifications by Conjugated Small-Molecules and Lanthanides Doping for Full Functional Perovskite Solar Cells. *Nano Energy* **2018**, *53*, 849–862.
(54) Marjani, S.; Khosroabadi, S.; Sabaghi, M. A High Efficiency Ultrathin CdTe Solar Cell for Nano-Area Applications. *Opt. Photonics J.* **2016**, *06* (02), 15–23.
(55) Onorato, J.; Pakhnyuk, V.; Luscombe, C. K. Structure and Design of Polymers for Durable, Stretchable Organic Electronics. *Polym. J.* **2017**, *49* (1), 41–60.
(56) Lipomi, D. J.; Tee, B. C.-K.; Vosgueritchian, M.; Bao, Z. Stretchable Organic Solar Cells. *Adv. Mater.* **2011**, *23* (15), 1771–1775.
(57) Noriega, R.; Rivnay, J.; Vandewal, K.; V Koch, F. P.; Stingelin, N.; Smith, P.; Toney, M. F.; Salleo, A. A General Relationship between Disorder, Aggregation and Charge Transport in Conjugated Polymers. *Nat. Mater.* **2013**, *12*, 1038–1044.
(58) Kang, S. D.; Snyder, G. J. Charge-Transport Model for Conducting Polymers. *Nat. Mater.* **2017**, *16* (2), 252–257.
(59) Chang, J.-F.; Sirringhaus, H.; Giles, M.; Heeney, M.; McCulloch, I. Relative Importance of Polaron Activation and Disorder on Charge Transport in High-Mobility Conjugated Polymer Field-Effect Transistors. *Phys. Rev. B* **2007**, *76* (20), 205204.
(60) DeLongchamp, D. M.; Kline, R. J.; Lin, E. K.; Fischer, D. A.; Richter, L. J.; Lucas, L. A.; Heeney, M.; McCulloch, I.; Northrup, J. E. High Carrier Mobility Polythiophene Thin Films: Structure Determination by Experiment and Theory. *Adv. Mater.* **2007**, *19* (6), 833–837.
(61) Zhang, W.; Smith, J.; Watkins, S. E.; Gysel, R.; McGehee, M.; Salleo, A.; Kirkpatrick, J.; Ashraf, S.; Anthopoulos, T.; Heeney, M.; et al. Indacenodithiophene Semiconducting Polymers for High-Performance, Air-Stable Transistors. *J. Am. Chem. Soc.* **2010**, *132* (33), 11437–11439.
(62) Mollinger, S. A.; Krajina, B. A.; Noriega, R.; Salleo, A.; Spakowitz, A. J. Percolation, Tie-Molecules, and the Microstructural Determinants of Charge Transport in Semicrystalline Conjugated Polymers. *ACS Macro Lett.* **2015**, *4* (7), 708–712.

(63) Martín, J.; Stingelin, N.; Cangialosi, D. Direct Calorimetric Observation of the Rigid Amorphous Fraction in a Semiconducting Polymer. *J. Phys. Chem. Lett.* **2018**, *9* (5), 990–995.
(64) Flory, P. J. Theory of Crystallization in Copolymers. *Trans. Faraday Soc.* **1955**, *51* (0), 848.
(65) Sanchez, I. C.; Eby, R. K. Thermodynamics and Crystallization of Random Copolymers. *Macromolecules* **1975**, *8* (5), 638–641.
(66) Yasuniwa, M.; Haraguchi, K.; Nakafuku, C.; Hirakawa, S. Effect of Molecular Weight on the Phase Diagram of Polyethylene under High Pressure. *Polym. J.* **1985**, *17* (11), 1209–1219.
(67) Wang, Z.; Ju, J.; Yang, J.; Ma, Z.; Liu, D.; Cui, K.; Yang, H.; Chang, J.; Huang, N.; Li, L. The Non-Equilibrium Phase Diagrams of Flow-Induced Crystallization and Melting of Polyethylene. *Sci. Rep.* **2016**, *6* (1), 32968.
(68) Verho, T.; Paajanen, A.; Vaari, J.; Laukkanen, A. Crystal Growth in Polyethylene by Molecular Dynamics: The Crystal Edge and Lamellar Thickness. *Macromolecules* **2018**, *51* (13), 4865–4873.
(69) Zhang, W.; Larson, R. G. Direct All-Atom Molecular Dynamics Simulations of the Effects of Short Chain Branching on Polyethylene Oligomer Crystal Nucleation. *Macromolecules* **2018**, *51* (13), 4762–4769.
(70) S. Gautam; S. Balijepalli, † and; Rutledge*, G. C. Molecular Simulations of the Interlamellar Phase in Polymers: Effect of Chain Tilt. **2000**.
(71) Rojas, G.; Inci, B.; Wei, Y.; Wagener, K. B. Precision Polyethylene: Changes in Morphology as a Function of Alkyl Branch Size. *J. Am. Chem. Soc.* **2009**, *131* (47), 17376–17386.
(72) Hosoda, S.; Nozue, Y.; Kawashima, Y.; Suita, K.; Seno, S.; Nagamatsu, T.; Wagener, K. B.; Inci, B.; Zuluaga, F.; Rojas, G.; et al. Effect of the Sequence Length Distribution on the Lamellar Crystal Thickness and Thickness Distribution of Polyethylene: Perfectly Equisequential ADMET Polyethylene vs Ethylene/α-Olefin Copolymer. *Macromolecules* **2011**, *44* (2), 313–319.
(73) Pulst, M.; Schneemann, C.; Ruda, P.; Golitsyn, Y.; Grefe, A.-K.; Stühn, B.; Busse, K.; Reichert, D.; Kressler, J. Chain Tilt and Crystallization of Ethylene Oxide Oligomers with Midchain Defects. *ACS Macro Lett.* **2017**, *6* (11), 1207–1211.
(74) Samiullah, M. H.; Pulst, M.; Golitsyn, Y.; Busse, K.; Poppe, S.; Hussain, H.; Reichert, D.; Kressler, J. Solid State Phase Transitions in Poly(Ethylene Oxide) Crystals Induced by Designed Chain Defects. *Macromolecules* **2018**, *51* (11), 4407–4414.
(75) Bronstein, H. A.; Luscombe, C. K. Externally Initiated Regioregular P3HT with Controlled Molecular Weight and Narrow Polydispersity. *J. Am. Chem. Soc.* **2009**, *131* (36), 12894–12895.
(76) Huang, Y.; Luscombe, C. K. Towards Green Synthesis and Processing of Organic Solar Cells. *Chem. Rec.* **2019**, *19*, 1–12.
(77) Mauer, R.; Kastler, M.; Laquai, F. The Impact of Polymer Regioregularity on Charge Transport and Efficiency of P3HT:PCBM Photovoltaic Devices. *Adv. Funct. Mater.* **2010**, *20* (13), 2085–2092.
(78) Poelking, C.; Andrienko, D. Effect of Polymorphism, Regioregularity and Paracrystallinity on Charge Transport in Poly(3-Hexylthiophene) [P3HT] Nanofibers. *Macromolecules* **2013**, *46* (22), 8941–8956.

(79) Kim, J.-S.; Kim, J.-H.; Lee, W.; Yu, H.; Kim, H. J.; Song, I.; Shin, M.; Oh, J. H.; Jeong, U.; Kim, T.-S.; et al. Tuning Mechanical and Optoelectrical Properties of Poly(3-Hexylthiophene) through Systematic Regioregularity Control. *Macromolecules* **2015**, *48* (13), 4339–4346.
(80) Snyder, C. R.; Henry, J. S.; Delongchamp, D. M. Effect of Regioregularity on the Semicrystalline Structure of Poly(3-Hexylthiophene). *Macromolecules* **2011**, *44*, 7088–7091.
(81) Kohn, P.; Huettner, S.; Komber, H.; Senkovskyy, V.; Tkachov, R.; Kiriy, A.; Friend, R. H.; Steiner, U.; Huck, W. T. S.; Sommer, J.-U.; et al. On the Role of Single Regiodefects and Polydispersity in Regioregular Poly(3-Hexylthiophene): Defect Distribution, Synthesis of Defect-Free Chains, and a Simple Model for the Determination of Crystallinity. *J. Am. Chem. Soc.* **2012**, *134* (4790–4805), 4790–4805.
(82) Balar, N.; O'Connor, B. T. Correlating Crack Onset Strain and Cohesive Fracture Energy in Polymer Semiconductor Films. *Macromolecules* **2017**, *50* (21), 8611–8618.
(83) Zhugayevych, A.; Mazaleva, O.; Naumov, A.; Tretiak, S. Lowest-Energy Crystalline Polymorphs of P3HT. *J. Phys. Chem. C* **2018**, *122* (16), 9141–9151.
(84) Kim, S.; Park, J. K.; Park, Y. D. Charge Transport Behaviors of End-Capped Narrow Band Gap Polymers in Bottom-Contact Organic Field-Effect Transistors. *RSC Adv.* **2014**, *4* (74), 39268–39272.
(85) Onorato, J. W.; Luscombe, C. K. Morphological Effects on Polymeric Mixed Ionic/Electronic Conductors. *Mol. Syst. Des. Eng.* **2019**, *4* (2), 310–324.
(86) Dong, B. X.; Nowak, C.; Onorato, J. W.; Strzalka, J.; Escobedo, F. A.; Luscombe, C. K.; Nealey, P. F.; Patel, S. N. Influence of Side-Chain Chemistry on Structure and Ionic Conduction Characteristics of Polythiophene Derivatives: A Computational and Experimental Study. *Chem. Mater.* **2019**, *31* (4), 1418–1429.
(87) Flagg, L. Q.; Bischak, C. G.; Onorato, J. W.; Rashid, R. B.; Luscombe, C. K.; Ginger, D. S. Polymer Crystallinity Controls Water Uptake in Glycol Side-Chain Polymer Organic Electrochemical Transistors. *J. Am. Chem. Soc.* **2019**, *141* (10), 4345–4354.
(88) Koldemir, U.; Puniredd, S. R.; Wagner, M.; Tongay, S.; McCarley, T. D.; Kamenov, G. D.; Müllen, K.; Pisula, W.; Reynolds, J. R. End Capping Does Matter: Enhanced Order and Charge Transport in Conjugated Donor–Acceptor Polymers. *Macromolecules* **2015**, *48* (18), 6369–6377.
(89) Tatum, W. K.; Resing, A. B.; Flagg, L. Q.; Ginger, D. S.; Luscombe, C. K. Defect Tolerance of π-Conjugated Polymer Crystal Lattices and Their Relevance to Optoelectronic Applications. *ACS Appl. Polym. Mater.* **2019**, *1* (6), 1466–1475.
(90) He, P. The Distribution of Degree of Crystallinity—New Concept in Polymer Science. *Chinese Chem. Lett.* **2018**, *29* (12), 1711–1712.
(91) Yang, Y.; Chen, M.; Li, H.; Li, H. The Degree of Crystallinity Exhibiting a Spatial Distribution in Polymer Films. *Eur. Polym. J.* **2018**, *107*, 303–307.
(92) Morin, P.-O.; Bura, T.; Leclerc, M. Realizing the Full Potential of Conjugated Polymers: Innovation in Polymer Synthesis. *Mater. Horizons* **2016**, *3* (1), 11–20.
(93) Chiu, M.; Jeng, U.; Su, C.; Liang, K. S.; Wei, K. Simultaneous Use of Small- and Wide-Angle X-ray Techniques to Analyze Nanometerscale Phase Separation in Polymer Heterojunction Solar Cells. *Adv. Mater.* **2008**, *20* (13), 2573–2578.
(94) Tatum, W. K.; Luscombe, C. K. π-Conjugated Polymer Nanowires: Advances and Perspectives toward Effective Commercial Implementation. *Polym. J.* **2018**, *50* (8), 659–

669.
(95) Roehling, J. D.; Arslan, I.; Moulé, A. J. Controlling Microstructure in Poly(3-Hexylthiophene) Nanofibers. *J. Mater. Chem.* **2012**, *22* (6), 2498.
(96) McMahon, D. P.; Cheung, D. L.; Goris, L.; Dacuña, J.; Salleo, A.; Troisi, A. Relation between Microstructure and Charge Transport in Polymers of Different Regioregularity. *J. Phys. Chem. C* **2011**, *115* (39), 19386–19393.
(97) Mena-Osteritz, E.; Meyer, A.; Langeveld-Voss, B. M. W.; Janssen, R. A. J.; Meijer, E. W.; Bäuerle, P. Two-Dimensional Crystals of Poly(3-Alkyl- Thiophene)s: Direct Visualization of Polymer Folds in Submolecular Resolution. *Angew. Chemie Int. Ed.* **2000**, *39* (15), 2679–2684.
(98) Han, Y.; Guo, Y.; Chang, Y.; Geng, Y.; Su, Z. Chain Folding in Poly(3-Hexylthiophene) Crystals. *Macromolecules* **2014**, *47* (11), 3708–3712.
(99) Welch, P.; Muthukumar, M. Molecular Mechanisms of Polymer Crystallization from Solution. *Phys. Rev. Lett.* **2001**, *87* (21), 218302.
(100) Garcia, R.; Proksch, R. Nanomechanical Mapping of Soft Matter by Bimodal Force Microscopy. *Eur. Polym. J.* **2013**, *49* (8), 1897–1906.
(101) Herruzo, E. T.; Garcia, R. Theoretical Study of the Frequency Shift in Bimodal FM-AFM by Fractional Calculus. *Beilstein J. Nanotechnol.* **2012**, *3* (1), 198–206.
(102) Giridharagopal, R.; Flagg, L. Q.; Harrison, J. S.; Ziffer, M. E.; Onorato, J.; Luscombe, C. K.; Ginger, D. S. Electrochemical Strain Microscopy Probes Morphology-Induced Variations in Ion Uptake and Performance in Organic Electrochemical Transistors. *Nat. Mater.* **2017**, *16* (7), 737–742.
(103) Nguyen, H. K.; Ito, M.; Nakajima, K. Elastic and Viscoelastic Characterization of Inhomogeneous Polymers by Bimodal Atomic Force Microscopy. *Jpn. J. Appl. Phys.* **2016**, *55* (8S1), 08NB06.
(104) Kocun, M.; Labuda, A.; Meinhold, W.; Revenko, I.; Proksch, R. Fast, High Resolution, and Wide Modulus Range Nanomechanical Mapping with Bimodal Tapping Mode. *ACS Nano* **2017**, *11* (10), 10097–10105.
(105) Christopher M. Stafford, *,†; Bryan D. Vogt, †; Christopher Harrison, †,§; Duangrut Julthongpiput, †,⊥ and; Huang‡, R. Elastic Moduli of Ultrathin Amorphous Polymer Films. **2006**.
(106) Saha, R.; Nix, W. D. Effects of the Substrate on the Determination of Thin Film Mechanical Properties by Nanoindentation. *Acta Mater.* **2002**, *50* (1), 23–38.
(107) Chen, Y.; Zhao, Y.; Liang, Z. Solution Processed Organic Thermoelectrics: Towards Flexible Thermoelectric Modules. *Energy Environ. Sci.* **2015**, *8* (2), 401–422.
(108) Patel, S. N.; Glaudell, A. M.; Peterson, K. A.; Thomas, E. M.; O'Hara, K. A.; Lim, E.; Chabinyc, M. L. Morphology Controls the Thermoelectric Power Factor of a Doped Semiconducting Polymer. *Sci. Adv.* **2017**, *3* (6), e1700434.
(109) van Franeker, J. J.; Westhoff, D.; Turbiez, M.; Wienk, M. M.; Schmidt, V.; Janssen, R. A. J. Controlling the Dominant Length Scale of Liquid-Liquid Phase Separation in Spin-Coated Organic Semiconductor Films. *Adv. Funct. Mater.* **2015**, *25* (6), 855–863.
(110) An, Q.; Ma, X.; Gao, J.; Zhang, F. Solvent Additive-Free Ternary Polymer Solar Cells with 16.27% Efficiency. *Sci. Bull.* **2019**, *64* (8), 504–506.
(111) Chortos, A.; Liu, J.; Bao, Z. Pursuing Prosthetic Electronic Skin. *Nat. Mater.* **2016**, *15* (9), 937–950.
(112) Mazzio, K. A.; Luscombe, C. K. The Future of Organic Photovoltaics. *Chem. Soc. Rev.*

2015, *44*, 78–90.
(113) Holliday, S.; Li, Y.; Luscombe, C. K. Recent Advances in High Performance Donor-Acceptor Polymers for Organic Photovoltaics. *Prog. Polym. Sci.* **2017**, *70*, 34–51.
(114) Dang, M. T.; Hirsch, L.; Wantz, G. P3HT:PCBM, Best Seller in Polymer Photovoltaic Research. *Adv. Mater.* **2011**, *23* (31), 3597–3602.
(115) Ji, Y.; Xiao, C.; Heintges, G. H. L.; Wu, Y.; Janssen, R. A. J.; Zhang, D.; Hu, W.; Wang, Z.; Li, W. Conjugated Polymer with Ternary Electron-Deficient Units for Ambipolar Nanowire Field-Effect Transistors. *J. Polym. Sci. Part A Polym. Chem.* **2016**, *54* (1), 34–38.
(116) Persson, N. E.; Rafshoon, J.; Naghshpour, K.; Fast, T.; Chu, P.-H.; McBride, M.; Risteen, B.; Grover, M.; Reichmanis, E. High-Throughput Image Analysis of Fibrillar Materials: A Case Study on Polymer Nanofiber Packing, Alignment, and Defects in Organic Field Effect Transistors. *ACS Appl. Mater. Interfaces* **2017**, *9* (41), 36090–36102.
(117) Bharti, M.; Singh, A.; Samanta, S.; Aswal, D. K. Conductive Polymers for Thermoelectric Power Generation. *Prog. Mater. Sci.* **2018**, *93*, 270–310.
(118) Yao, H.; Fan, Z.; Cheng, H.; Guan, X.; Wang, C.; Sun, K.; Ouyang, J. Recent Development of Thermoelectric Polymers and Composites. *Macromol. Rapid Commun.* **2018**, *39* (6), 1700727.
(119) Liu, Y.; Zhao, J.; Li, Z.; Mu, C.; Ma, W.; Hu, H.; Jiang, K.; Lin, H.; Ade, H.; Yan, H. Aggregation and Morphology Control Enables Multiple Cases of High-Efficiency Polymer Solar Cells. *Nat. Commun.* **2014**, *5*, 5293.
(120) Ye, L.; Xiong, Y.; Li, S.; Ghasemi, M.; Balar, N.; Turner, J.; Gadisa, A.; Hou, J.; O'Connor, B. T.; Ade, H. Precise Manipulation of Multilength Scale Morphology and Its Influence on Eco-Friendly Printed All-Polymer Solar Cells. *Adv. Funct. Mater.* **2017**, *27* (33), 1702016.
(121) Diao, Y.; Shaw, L.; Bao, Z.; Mannsfeld, S. C. B. Morphology Control Strategies for Solution-Processed Organic Semiconductor Thin Films. *Energy Environ. Sci.* **2014**, *7* (7), 2145–2159.
(122) Cha, H.; Wheeler, S.; Holliday, S.; Dimitrov, S. D.; Wadsworth, A.; Lee, H. H.; Baran, D.; McCulloch, I.; Durrant, J. R. Influence of Blend Morphology and Energetics on Charge Separation and Recombination Dynamics in Organic Solar Cells Incorporating a Nonfullerene Acceptor. *Adv. Funct. Mater.* **2018**, *28* (3), 1704389.
(123) Greco, C.; Melnyk, A.; Kremer, K.; Andrienko, D.; Daoulas, K. C. Generic Model for Lamellar Self-Assembly in Conjugated Polymers: Linking Mesoscopic Morphology and Charge Transport in P3HT. *Macromolecules* **2019**, *52* (3), 968–981.
(124) Collins, B. A.; Tumbleston, J. R.; Ade, H. Miscibility, Crystallinity, and Phase Development in P3HT/PCBM Solar Cells: Toward an Enlightened Understanding of Device Morphology and Stability. *J. Phys. Chem. Lett.* **2011**, *2* (24), 3135–3145.
(125) Flagg, L. Q.; Bischak, C. G.; Onorato, J. W.; Rashid, R. B.; Luscombe, C. K.; Ginger, D. S. Polymer Crystallinity Controls Water Uptake in Glycol Side-Chain Polymer Organic Electrochemical Transistors. *J. Am. Chem. Soc.* **2019**, *141* (10), 4345–4354.
(126) Giridharagopal, R.; Cox, P. A.; Ginger, D. S. Functional Scanning Probe Imaging of Nanostructured Solar Energy Materials. *Acc. Chem. Res.* **2016**, *49* (9), 1769–1776.
(127) Giridharagopal, R.; Rayermann, G. E.; Shao, G.; Moore, D. T.; Reid, O. G.; Tillack, A. F.; Masiello, D. J.; Ginger, D. S. Submicrosecond Time Resolution Atomic Force Microscopy for Probing Nanoscale Dynamics. *Nano Lett.* **2012**, *12* (2), 893–898.

(128) Giridharagopal, R.; Ginger, D. S. Characterizing Morphology in Bulk Heterojunction Organic Photovoltaic Systems. *J. Phys. Chem. Lett.* **2010**, *1* (7), 1160–1169.
(129) Pingree, L. S. C.; Reid, O. G.; Ginger, D. S. Electrical Scanning Probe Microscopy on Active Organic Electronic Devices. *Adv. Mater.* **2009**, *21* (1), 19–28.
(130) Baghgar, M.; Barnes, M. D. Work Function Modification in P3HT H/J Aggregate Nanostructures Revealed by Kelvin Probe Force Microscopy and Photoluminescence Imaging. *ACS Nano* **2015**, *9* (7), 7105–7112.
(131) Killgore, J. P.; DelRio, F. W. Contact Resonance Force Microscopy for Viscoelastic Property Measurements: From Fundamentals to State-of-the-Art Applications. *Macromolecules* **2018**, *51* (18), 6977–6996.
(132) Wood, D.; Hancox, I.; Jones, T. S.; Wilson, N. R. Quantitative Nanoscale Mapping with Temperature Dependence of the Mechanical and Electrical Properties of Poly(3-Hexylthiophene) by Conductive Atomic Force Microscopy. *J. Phys. Chem. C* **2015**, *119* (2), 11459–11467.
(133) Passeri, D.; Rossi, M.; Tamburri, E.; Terranova, M. L. Mechanical Characterization of Polymeric Thin Films by Atomic Force Microscopy Based Techniques. *Anal. Bioanal. Chem.* **2013**, *405* (5), 1463–1478.
(134) Kong, J.; Giridharagopal, R.; Harrison, J. S.; Ginger, D. S. Identifying Nanoscale Structure–Function Relationships Using Multimodal Atomic Force Microscopy, Dimensionality Reduction, and Regression Techniques. *J. Phys. Chem. Lett.* **2018**, *9* (12), 3307–3314.
(135) Stirling, J.; Woolley, R. A. J.; Moriarty, P. Scanning Probe Image Wizard: A Toolbox for Automated Scanning Probe Microscopy Data Analysis. *Rev. Sci. Instrum.* **2013**, *84* (11), 113701.
(136) Groeber, M. A.; Jackson, M. A. DREAM.3D: A Digital Representation Environment for the Analysis of Microstructure in 3D. *Integr. Mater. Manuf. Innov.* **2014**, *3* (1), 56–72.
(137) Neumayer, S. M.; Collins, L.; Vasudevan, R.; Smith, C.; Somnath, S.; Shur, V. Y.; Jesse, S.; Kholkin, A. L.; Kalinin, S. V.; Rodriguez, B. J. Decoupling Mesoscale Functional Response in PLZT across the Ferroelectric–Relaxor Phase Transition with Contact Kelvin Probe Force Microscopy and Machine Learning. *ACS Appl. Mater. Interfaces* **2018**, *10* (49), 42674–42680.
(138) Kalinin, S. V.; Strelcov, E.; Belianinov, A.; Somnath, S.; Vasudevan, R. K.; Lingerfelt, E. J.; Archibald, R. K.; Chen, C.; Proksch, R.; Laanait, N.; et al. Big, Deep, and Smart Data in Scanning Probe Microscopy. *ACS Nano* **2016**, *10* (10), 9068–9086.
(139) Somnath, S.; Smith, C. R.; Kalinin, S. V.; Chi, M.; Borisevich, A.; Cross, N.; Duscher, G.; Jesse, S. Feature Extraction via Similarity Search: Application to Atom Finding and Denoising in Electron and Scanning Probe Microscopy Imaging. *Adv. Struct. Chem. Imaging* **2018**, *4* (1), 3.
(140) Borodinov, N.; Neumayer, S.; Kalinin, S. V.; Ovchinnikova, O. S.; Vasudevan, R. K.; Jesse, S. Deep Neural Networks for Understanding Noisy Data Applied to Physical Property Extraction in Scanning Probe Microscopy. *npj Comput. Mater.* **2019**, *5* (1), 25.
(141) Li, X.; Dyck, O. E.; Oxley, M. P.; Lupini, A. R.; McInnes, L.; Healy, J.; Jesse, S.; Kalinin, S. V. Manifold Learning of Four-Dimensional Scanning Transmission Electron Microscopy. *npj Comput. Mater.* **2019**, *5* (1), 5.
(142) Rickman, J. M.; Lookman, T.; Kalinin, S. V. Materials Informatics: From the Atomic-Level to the Continuum. *Acta Mater.* **2019**, *168*, 473–510.

(143) Mukaddem, K. T.; Beard, E. J.; Yildirim, B.; Cole, J. M. ImageDataExtractor: A Tool To Extract and Quantify Data from Microscopy Images. *J. Chem. Inf. Model.* **2019**, acs.jcim.9b00734.
(144) Woolley, R. A. J.; Stirling, J.; Radocea, A.; Krasnogor, N.; Moriarty, P. Automated Probe Microscopy via Evolutionary Optimization at the Atomic Scale. *Appl. Phys. Lett.* **2011**, *98* (25), 253104.
(145) Beck, D. A. C.; Carothers, J. M.; Subramanian, V. R.; Pfaendtner, J. Data Science: Accelerating Innovation and Discovery in Chemical Engineering. *AIChE J.* **2016**, *62* (5), 1402–1416.
(146) van der Walt, S. C. C.; Varoquaux, G. The Numpy Array: A Structure for Efficient Numerical Computation. *Comput. Sci. Eng.* **2011**, *13*, 22–30.
(147) Eric Jones Travis Oliphant, P. P. et al. Scipy: Open Source Scientific Tools for Python.
(148) Hunter, J. D. Matplotlib: A 2D Graphics Environment. *Comput. Sci. Eng.* **2007**, *9*, 90–95.
(149) Fabian Pedregosa Gael Varoquaux, A. G. et al. Scikit-Learn: Machine Learning in Python. *J. Mach. Learn. Res.* **2011**, *12*, 2825–2830.
(150) van der Walt Johannes L. Schonberger, J. N.-I. et al. Scikit-Image: Image Processing in Python. *PeerJ*. 2014, p e453.
(151) Somnath, S.; Smith, C. R.; Jesse, S.; Laanait, N. Pycroscopy - An Open Source Approach to Microscopy and Microanalysis in the Age of Big Data and Open Science. *Microsc. Microanal.* **2017**, *23* (S1), 224–225.
(152) Somnath, S.; Smith, C. R.; Laanait, N.; Vasudevan, R. K.; Ievlev, A.; Belianinov, A.; Lupini, A. R.; Shankar, M.; Kalinin, S. V.; Jesse, S. USID and Pycroscopy -- Open Frameworks for Storing and Analyzing Spectroscopic and Imaging Data. *arXiv* **2019**.
(153) Tatum, W.; Torrejon, D.; O'Neil, P.; Onorato, J. W.; Resing, A.; Holliday, S.; Flagg, L. Q.; Ginger, D. S.; Luscombe, C. K. A Generalizable Framework for Algorithmic Interpretation of Thin Film Morphologies in Scanning Probe Images. *J. Chem. Inf. Model.* **2020**, *16* (03), 17.
(154) Nečas, D.; Klapetek, P. Gwyddion: An Open-Source Software for SPM Data Analysis. *Open Phys.* **2012**, *10* (1), 181–188.
(155) Takahashi, K.; Yamagishi, T.; Aoyagi, S.; Aoki, D.; Fukushima, K.; Kimura, Y. Principal Component Analysis Image Fusion of TOF-SIMS and Microscopic Images and Low Intensity Secondary Ion Enhancement by Pixel Reduction. *J. Vac. Sci. Technol. B* **2018**, *36* (3), 03F113.
(156) Seifrid, M. T.; Oosterhout, S. D.; Toney, M. F.; Bazan, G. C. Kinetic Versus Thermodynamic Orientational Preferences for a Series of Isomorphic Molecular Semiconductors. *ACS Omega* **2018**, *3* (8), 10198–10204.
(157) Rinehart, S. J.; Yuan, G.; Dadmun, M. D. Elucidating the Kinetic and Thermodynamic Driving Forces in Polymer Blend Film Self-Stratification. *Macromolecules* **2018**, *51* (19), 7836–7844.
(158) Na, J. Y.; Kang, B.; Lee, S. G.; Cho, K.; Park, Y. D. Surface-Mediated Solidification of a Semiconducting Polymer during Time-Controlled Spin-Coating. *ACS Appl. Mater. Interfaces* **2017**, *9* (11), 9871–9879.
(159) Ruan, C. "Skin-Core-Skin" Structure of Polymer Crystallization Investigated by Multiscale Simulation. *Mater. (Basel, Switzerland)* **2018**, *11* (4), 610.
(160) Young, T. J.; Monclus, M. A.; Burnett, T. L.; Broughton, W. R.; Ogin, S. L.; Smith, P. A. The Use of the PeakForce ™ Quantitative Nanomechanical Mapping AFM-Based Method

for High-Resolution Young's Modulus Measurement of Polymers. *Meas. Sci. Technol.* **2011**, *22* (12), 125703.
(161) B.T.M., R. J.; Arnold, M. The Watershed Transform: Definitions, Algorithms and Parallelization Strategies. *Fundam. Informaticae* **2000**, *41* (1, 2), 187–228.
(162) Edelsbrunner, H.; Harer, J. *Computational Topology - an Introduction.*; American Mathematical Society, 2010.
(163) Noriega, R. Efficient Charge Transport in Disordered Conjugated Polymer Microstructures. *Macromol. Rapid Commun.* **2018**, *39* (14), 1800096.
(164) Chou, K. W.; Yan, B.; Li, R.; Li, E. Q.; Zhao, K.; Anjum, D. H.; Alvarez, S.; Gassaway, R.; Biocca, A.; Thoroddsen, S. T.; et al. Spin-Cast Bulk Heterojunction Solar Cells: A Dynamical Investigation. *Adv. Mater.* **2013**, *25* (13), 1923–1929.
(165) Yan, Y.; Liu, X.; Wang, T. Conjugated-Polymer Blends for Organic Photovoltaics: Rational Control of Vertical Stratification for High Performance. *Adv. Mater.* **2017**, *29* (20), 1601674.
(166) Chang, M.; Lee, J.; Chu, P.-H.; Choi, D.; Park, B.; Reichmanis, E. Anisotropic Assembly of Conjugated Polymer Nanocrystallites for Enhanced Charge Transport. *ACS Appl. Mater. Interfaces* **2014**, *6* (23), 21541–21549.
(167) Kohn, P.; Rong, Z.; Scherer, K. H.; Sepe, A.; Sommer, M.; Müller-Buschbaum, P.; Friend, R. H.; Steiner, U.; Hüttner, S. Crystallization-Induced 10-Nm Structure Formation in P3HT/PCBM Blends. *Macromolecules* **2013**, *46* (10), 4002–4013.
(168) Vaynzof, Y.; Kabra, D.; Zhao, L.; Chua, L. L.; Steiner, U.; Friend, R. H. Surface-Directed Spinodal Decomposition in Poly[3-Hexylthiophene] and C $_{61}$ -Butyric Acid Methyl Ester Blends. *ACS Nano* **2011**, *5* (1), 329–336.
(169) Goh, T.; Huang, J.-S.; Yager, K. G.; Sfeir, M. Y.; Nam, C.-Y.; Tong, X.; Guard, L. M.; Melvin, P. R.; Antonio, F.; Bartolome, B. G.; et al. Quaternary Organic Solar Cells Enhanced by Cocrystalline Squaraines with Power Conversion Efficiencies >10%. *Adv. Energy Mater.* **2016**, *6* (21), 1600660.
(170) Botiz, I.; Stingelin, N. Influence of Molecular Conformations and Microstructure on the Optoelectronic Properties of Conjugated Polymers. *Materials (Basel).* **2014**, *7* (12), 2273–2300.
(171) Yan, Y.; Liu, X.; Wang, T. Conjugated-Polymer Blends for Organic Photovoltaics: Rational Control of Vertical Stratification for High Performance. *Adv. Mater.* **2017**, *29* (20), 1601674.
(172) Chang, M.; Lim, G.; Park, B.; Reichmanis, E. Control of Molecular Ordering, Alignment, and Charge Transport in Solution-Processed Conjugated Polymer Thin Films. *Polymers (Basel).* **2017**, *9* (12), 212.
(173) Tatum, W. K.; Torrejon, D.; O'Neil, P.; Onorato, J. W.; Resing, A. B.; Holliday, S.; Flagg, L. Q.; Ginger, D. S.; Luscombe, C. K. Generalizable Framework for Algorithmic Interpretation of Thin Film Morphologies in Scanning Probe Images. *J. Chem. Inf. Model.* **2020**, acs.jcim.0c00308.
(174) Paszke, A.; Gross, S.; Massa, F.; Lerer, A.; Bradbury, J.; Chanan, G.; Chintala, S. PyTorch: An Imperative Style, High-Performance Deep Learning Library. *Adv. Neural Inf. Process. Syst.* **2019**, *32*, 8024–8035.
(175) Choi, H. H.; Cho, K.; Frisbie, C. D.; Sirringhaus, H.; Podzorov, V. Critical Assessment of Charge Mobility Extraction in FETs. *Nature Materials*. Nature Publishing Group December 19, 2017, pp 2–7.

(176) Choi, D.; Chu, P. H.; McBride, M.; Reichmanis, E. Best Practices for Reporting Organic Field Effect Transistor Device Performance. *Chemistry of Materials*. American Chemical Society June 23, 2015, pp 4167–4168.
(177) Jones, M. L.; Dyer, R.; Clarke, N.; Groves, C. Are Hot Charge Transfer States the Primary Cause of Efficient Free-Charge Generation in Polymer:Fullerene Organic Photovoltaic Devices? A Kinetic Monte Carlo Study. *Phys. Chem. Chem. Phys.* **2014**, *16* (38), 20310–20320.
(178) Zhan, P.; Zhang, W.; Jacobs, I. E.; Nisson, D. M.; Xie, R.; Weissen, A. R.; Colby, R. H.; Moulé, A. J.; Milner, S. T.; Maranas, J. K.; et al. Side Chain Length Affects Backbone Dynamics in Poly(3-Alkylthiophene)S. *J. Polym. Sci. Part B Polym. Phys.* **2018**, *56* (17), 1193–1202.
(179) Yong, X.; Shi, W.; Wu, G.; Goh, S. S.; Bai, S.; Xu, J.-W.; Wang, J.-S.; Yang, S.-W. Tuning the Thermoelectric Performance of π–d Conjugated Nickel Coordination Polymers through Metal–Ligand Frontier Molecular Orbital Alignment. *J. Mater. Chem. A* **2018**.
(180) Xu, B.; Yi, X.; Huang, T.-Y.; Zheng, Z.; Zhang, J.; Salehi, A.; Coropceanu, V.; Ho, C. H. Y.; Marder, S. R.; Toney, M. F.; et al. Donor Conjugated Polymers with Polar Side Chain Groups: The Role of Dielectric Constant and Energetic Disorder on Photovoltaic Performance. *Adv. Funct. Mater.* **2018**, 1803418.
(181) Kobayashi, H.; Shirasawa, R.; Nakamoto, M.; Hattori, S.; Tomiya, S. Carrier Mobility in Mesoscale Heterogeneous Organic Materials: Effects of Crystallinity and Anisotropy on Efficient Charge Transport. *Appl. Phys. Lett.* **2017**, *111* (3), 033301.
(182) Guilbert, A. A. Y.; Zbiri, M.; Dunbar, A. D. F.; Nelson, J. Quantitative Analysis of the Molecular Dynamics of P3HT:PCBM Bulk Heterojunction. *J. Phys. Chem. B* **2017**, *121* (38), 9073–9080.
(183) Li, J.; Koshnick, C.; Diallo, S. O.; Ackling, S.; Huang, D. M.; Jacobs, I. E.; Harrelson, T. F.; Hong, K.; Zhang, G.; Beckett, J.; et al. Quantitative Measurements of the Temperature-Dependent Microscopic and Macroscopic Dynamics of a Molecular Dopant in a Conjugated Polymer. *Macromolecules* **2017**, *50* (14), 5476–5489.
(184) Tummala, N. R.; Risko, C.; Bruner, C.; Dauskardt, R. H.; Brédas, J.-L. Entanglements in P3HT and Their Influence on Thin-Film Mechanical Properties: Insights from Molecular Dynamics Simulations. *J. Polym. Sci. Part B Polym. Phys.* **2015**, *53* (13), 934–942.

VITA

Wesley Tatum was born in New Mexico, but also lived in Virginia and Michigan before finishing high school while living in Washington State. He has always held an interest in science and a reverence for nature, as a result of his family, education, and life experience. Throughout elementary, middle, and high school, teachers like Greenbrier Elementary School's Mr. Parks and Jesuit High School's Mr. Feebeck sparked and nurtured these interests. Wesley went to Whitworth University, where he received a B.S. in Physical Chemistry and a B.A. in Physics. While at Whitworth, Wesley was an All-American swimmer and met his wife, Bethany. After such impactful classes at Whitworth, taught by Prof. Ong, Prof. Stevens, and Prof. Larkin, as well as a summer research internship through the National Nanotechnology Infrastructure Network, Wesley joined Prof. Christine Luscombe's research group at the University of Washington. At the UW, Wesley received the Wagstaff, DIRECT, GO-MAP Presidential and ARCS Fellowships. During this time, Wesley's passions for science, nature, and community flourished as he worked as an officer in Diversity In Clean Energy (DICE) for 3 years and established the student group GRID (Global Renewables Infrastructure Network). The latter of which stemmed from work with Prof. Lilo Pozzo to explore solar energy for off-grid applications in disaster relief and developing communities. He was awarded Husky 100 in 2019, as well the Clean Energy Institute's Outreach award, and a nomination by the Materials Science and Engineering department for the Graduate School Medal. He was the departmental nomination for the Graduate School Medal in both 2019 and 2020, being a finalist in 2020. His research included a wide range of topics, including self-assembly, device fabrication, microscopy, computer vision, natural language processing, resilient energy, and equitable research practices in co-creative research.

PUBLICATIONS

1. **Tatum, Wesley K.**; Torrejon, Diego; O'Neil, Patrick; Onorato, Jonathan W.; Resing, Anton; Holliday, Sara; Flagg, Lucas Q.; Ginger, David S.; Luscomb, Christine K. A Generalizable Framework for Algorithmic Interpretation of Thin Film Morphologies in Scanning Probe Images. *ACS. J. Chem. Inf. Model.*, **2020**.

2. **Tatum, Wesley K.**; Resing, Anton B.; Flagg, Lucas Q.; Ginger, David S.; Luscombe, Christine K. Defect Tolerance of π-Conjugated polymers and their relevance to optoelectronic applications. *ACS. Appl. Polym. Mat.*, **2019**, 1 (6), 1466-1475.

3. Keerthisinghe, Chanaka; Ahumada-Paras, Mareldi; Pozzo, Lilo D.; Kirschen, Daniel S.; Pontes, Hugo; **Tatum, Wesley K.**; Matos, Marvi A. PV-Battery Systems for Critical Loads During Emergencies. *IEEE Power and Energy*, **2019**, 17, 1, 82-92.

4. Shi, Qinqin; **Tatum, Wesley K.**; Zhang, Junxiang; Scott, Colleen; Luscombe, Christine K; Marder, Seth R.; Blakely, Simon B. The Direct Arylation Polymerization (DArP) of Well-Defined Alternating Copolymers Based On 5,6-Dicyano[2,1,3]benzothiadiazole (DCBT). *Asian J. of Org. Chem.*, **2018**, 7 (7), 1419-1425.

5. **Tatum, Wesley K.**; Luscombe, Christine K. π-Conjugated polymer nanowires: advances and perspectives towards effective commercial implementation. *Polym. J.*, **2018**, 50 (8), 659-669.

6. Haydon, Ian; Herpoldt, Karla-Louise; Hosseinzadeh, Parisa; Kang, Christine; Kang, Lauren J.; Montoni, Nicholas P.; **Tatum, Wesley K.** Workforce diversity: Strategies for cultivating inclusion in research. *Inside eLife*, **2018**, https://elifesciences.org/inside-elife/8a24d01a/workforce-diversity-strategies-for-cultivating-inclusion-in-research.

7. Li, Yilin; **Tatum, Wesley K.**; Onorato, Jonathan W.; Zhang, Yongcao; Luscombe, Christine K. Low elastic modulus and high charge mobility of low-crystallinity indacenodithiophene-based semiconducting polymers for potential applications in stretchable electronics. *Macromolecules*, **2018**, 51 (16), 6352-6358.

8. Xi, Yuyin; Li, David S.; Newbloom, Greg M.; **Tatum, Wesley K.**; O'Donnell, Matthew; Luscombe, Christine K.; Pozzo, Lilo D. Sonocrystallization of conjugated polymers with ultrasound fields. *Soft Matter*, **2018**, 14 (24), 4963-4976.

9. Li, Yilin; **Tatum, Wesley K.**; Onorato, Jonathan W.; Barajas, Sierra D.; Yang, Yun Y.; Luscombe, Christine K. An indacenodithiophene-based semiconducting polymer with high ductility for stretchable organic electronics. *Polym. Chem.* **2017**, 8 (34), 5185-5193.